

ALMA MATER STUDIORUM-UNIVERSITY OF BOLOGNA

---

SCHOOL OF ENGINEERING AND ARCHITECTURE

Second Cycle Degree in

Telecommunications Engineering

Master Thesis in

Communication Systems: Theory and Measurement

# **SIGNAL PROCESSING AT EM LEVEL USING METASURFACES**

Author:

**KRISHNA PRASAD BACHU**

Supervisor:

Prof. Ing. **DAVIDE DARDARI**

---

Academic Year 2020/2021

Graduation Session 3rd

# Acronyms

**IRS** Intelligent Reflecting Surface

**LIS** Large Intelligent Surface

**SIS** Small Intelligent Surface

**DAM** Direct Antenna Modulation

**QPSK** Quadrature Phase Shift Keying

**FSS** Frequency selective surface

**LoS** Line of Sight

**DoF** Degree of Freedom

**SWIPT** Simultaneous Wireless Information and Power Transfer

**RIS** Reconfigurable Intelligent Surfaces

**SRE** Smart Radio Environment

**DL** Deep Learning

**HIS** High Impedance Surface

**IFFT** Inverse Fast Fourier Transform

**LTI** Linear Time Invariant

**BER** Bit Error Rate

**GSM** Global System Mobile Communications

**DL** Deep Learning

**AM** Amplitude Modulation

**PM** Phase Modulation

**TML** Multi-Focus Lens

**IMT** Insulator to Metal Transition

**IPCA** Interdigitated Photo-Conductive Antenna

**SSR** Split Ring Resonators

**SPP** Surface Plasmon Polariton

**EIRP** Effective Isotropic Radiated Power

# Introduction

In recent decades, the field of telecommunications, driven by a high demand for digital communications characterized by low latencies, has undergone considerable development. The exponential growth of data traffic, which is estimated to reach hundreds of connected devices per cubic meter in the future, and future applications to be supported, including virtual reality, autonomous driving and 4K / 8K UHD video streaming, will impose requirements for bit-rate and latency that cannot be satisfied by today's fifth generation standard but will require a large band, presumably identifiable in the TeraHertz band, located between the microwave and the visible spectrum [1]. It is also expected that in the near future, with the advent of the sixth generation (6G) standard, the Digital Signal Processing (DSP) techniques currently used may not be sufficient to satisfy the required requirements. The causes of the limitations of the DSP are to be found in the high frequencies of the signals, which, according to Shannon's theorem, require analog-to-digital converters (ADCs) and digital-to-analog converters (DACs) operating at very high frequencies. Furthermore, the high amount of binary data produced by the ADCs could not be processed by today's digital circuits, guaranteeing low latencies and low power consumption. In light of this, at the academic level, alternative methods are being investigated to perform Signal Processing directly on the electromagnetic wave carrying the information, in order to simplify the processing performed digitally, with advantages in terms of small latencies.

The development of the 6G standard, in addition to the exploitation of portions of the radio spectrum at ever higher frequencies, will also require the introduction of new design paradigms for wireless networks enabled by new technologies. One of them is the technology of metasurfaces, devices capable of interacting with electromagnetic waves by performing functions that are not present or difficult to obtain in nature. In particular, by exploiting the properties of metasurfaces, the postulate according to which the propagation space of the wireless signal:

- is controlled only by nature
- cannot be altered

effectively transforming the propagation space into something programmable

(Smart Radio Environments [8]). Also, using the ability of the metasurfaces to manipulate amplitude and phase of an electromagnetic wave, it is expected that, to decrease latencies, a part of the signal processing can take place directly at the electromagnetic level, thus introducing the new field of electromagnetic signal processing. This thesis illustrates the metasurfaces developed in recent years, analyzing their electromagnetic characteristics and peculiarities in order to derive an input-output model of the implemented function. Subsequently, exploiting some of the proposed metasurfaces. The treatment of this thesis is structured as follows: In Chapter 1: Metamaterials and Metasurfaces, this chapter covers the description of metamaterials. The metasurface generations show how the metasurface has improved over time. Using Reconfigurable Intelligent Surface and its technologies, transforming the environment into a smart radio environment.

In Chapter 2: Development of Metasurfaces, which is concerned with the advancement of metasurface programming in space and time to change the amplitude and phase in order to achieve the desired beamforming and particular attention to the Metasurface that changes over time.

In Chapter 3: Metasurfaces working beyond millimeter waves, which is concerned with, how can a time-varying metasurface be utilized to control the amplitude and phase in the Terahertz band and how can it be controlled thermally, electrically, and optically.

In Chapter 4: Conclusions

# Contents

<b>Introduction</b>	<b>iv</b>
<b>1 Metamaterials and MetaSurfaces</b>	<b>1</b>
1.1 Metamaterials . . . . .	1
1.2 Generations of Metasurface . . . . .	3
1.2.1 Metasurface 2.0 . . . . .	4
1.2.2 Metasurface 3.0 . . . . .	5
1.3 Smart Radio Environments and Reconfigurable Intelligent Surfaces	6
1.3.1 Smart Radio Environment . . . . .	6
1.3.2 Reconfigurable Intelligent Surfaces (RIS) . . . . .	7
1.3.3 Solutions for RISs . . . . .	10
<b>2 Development of Metasurfaces</b>	<b>15</b>
2.1 Materials and Methods . . . . .	15
2.1.1 Coding Metamaterials . . . . .	15
2.1.2 Digital Metamaterials . . . . .	17
2.1.3 Programmable Metamaterials . . . . .	20
2.2 Dynamic Metasurface Antennas . . . . .	22
2.2.1 DMA for Near Field Communication . . . . .	26
2.3 Time-controlled metasurfaces for Frequency conversion . . . . .	29
2.4 Time-modulated metasurfaces for Frequency Translation . . . . .	33
2.5 Space-time-coding digital metasurfaces . . . . .	37
2.6 Metaprism for Passive and non-reconfigurable metasurface . . . . .	43
2.7 Non-reciprocal and programmable meta-prism . . . . .	45
2.8 Selective camouflage using time-controlled metasurfaces . . . . .	48
2.9 Secure Electromagnetic Buildings using Slow Phase-Switching FSS	51
<b>3 Metasurfaces working beyond millimeter waves</b>	<b>54</b>
3.1 Time-Varying Metasurfaces Based on Graphene Microribbon Arrays	54
3.2 Linear Frequency Conversion via Sudden Merging of Resonances	58
3.3 Electrical control of terahertz frequency conversion . . . . .	60

3.4	Thermally switchable terahertz wavefront metasurface . . . . .	62
3.5	Graphene-Based Plasmonic Nano-Antenna Array . . . . .	67
<b>4</b>	<b>Conclusion</b>	<b>74</b>
	<b>List of Figures</b>	<b>81</b>
	<b>Bibliography</b>	<b>82</b>



# Chapter 1

## Metamaterials and MetaSurfaces

### 1.1 Metamaterials

Metamaterials (where meta mean ‘beyond’) are essentially man-made devices, designed to obtain a behaviour which is not typically present in Nature and to control the wavefront of light (or generally any type of wave-like phenomenon) through the use of user-defined constituent ‘atoms’ - where an atom, or meta-atom, denotes that the element is smaller than the wavelength of interest, meaning that the effect is averaged. Negative refractive index materials, zero-index materials, invisibility cloaking, and sub-diffraction imaging have all been developed as a result of these studies, which would be impossible to produce using the optical properties of naturally occurring materials. However, despite the exciting and unusual physical phenomena presented by such metamaterials, their bulky volumetric organization poses numerous production challenges, preventing their direct usage in the creation of practical electronics.

Due to the fact that they can provide similar phenomena as metamaterials, but are only a fraction of a wavelength thin 2D planar metamaterials are potentially simpler to realize and much easier to build and the associated losses are negligible. The 2D planar metamaterials namely metasurfaces, have attracted a lot of attention in recent years. Metasurfaces have been used to create a variety of optical devices, the majority of which use abrupt phase changes to manipulate the wavefront of light. They have been used not only in the optical regime but also in radio-based applications as well.

Hasman used the idea of Geometric phase (or Pancharatnam-Berry phase), which is the wavelength-insensitive phase modification of a transmitted wave based only on the polarisation states crossed on the Poincaré sphere [2]. These works used a basic method of rotating planar optical elements, which in this case were sub-wavelength gratings, to produce a spatially variable phase alteration of

incident light. Previous uses of geometric phase had been time-variant (and spatially invariant i.e. laterally isotropic media), such that the phase of the light was changed after completing a cyclic path around the Poincaré sphere by propagating through optical devices (polarisers). This work was a crucial step in the formation of metasurfaces, as we now know them.

## Poincaré Sphere

Henri Poincaré devised the Poincaré Sphere concept in the late nineteenth century, which allows any polarization of light to be represented geometrically on the surface of a sphere. In Figure 2.6, you can see a schematic illustration of this. The north and south poles correspond to circularly polarised light, the equator to linearly polarised light (with x and y polarisations in opposing directions), and any position between the poles and the equator to elliptically polarised light. When dealing with optical devices, this visualization is very useful because a wave propagates through a number of them, each changing the polarization state, and therefore tracing out a route on the Poincaré sphere. The spots on the sphere will remain near even if the polarization changes slightly. Because each point corresponds to a state, if a beam of light changes polarization state, an arc or path between two points suggests a continuous polarization state evolution and is deemed slowly-varying and thus adiabatic. Because the Poincaré sphere is a 3D object and Jones vectors are 2D, the correspondence is because the surface of the Poincaré sphere is the only place where a polarisation state can be defined a state cannot exist within the sphere and thus Jones vectors describe the 2D surface of the Poincaré sphere well.

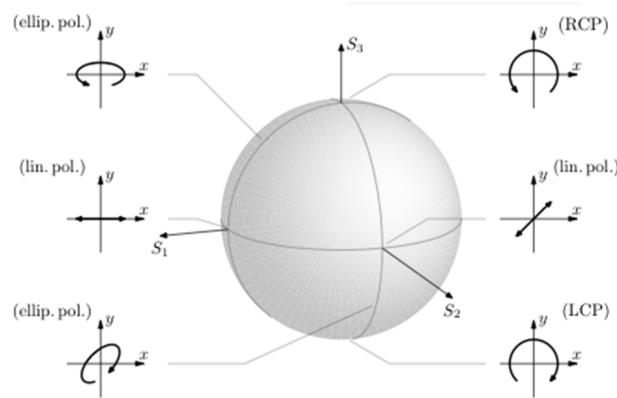


Figure 1.1: Visual illustration of the Poincaré Sphere for representing polarisation states of light [2].

Some years later, the concept of laterally abrupt phase-changes utilizing meta-

surfaces allowed a generalization of Snell's law by incorporating a phase gradient term, which was carried out by Capasso [4]. This work used geometrically varying V-shaped antennas arranged such that the individual phase of each one was periodically increasing by a small amount. This resulted in the negative refraction of light at an interface, work which had only been previously realized using metamaterials. Following this work and combining the geometric functionality Chen created a plasmonic flat lens that operated in the visible spectrum using phase rather than antenna geometry and phase-gradient metasurfaces. Circular polarization conversion was used, which traces out pole-to-pole arcs on the Poincaré sphere and results in a phase modification of the wavefront, allowing for both concave and convex lens functionality. Crozier [6] proposed a silicon nanofin phase-gradient as a means of distinguishing the handedness of incident circularly polarised light by diffracting the opposite handedness into different angles, building on previous work on geometric-phase controlled lenses using metal nano structures. As a result, it was discovered that high-efficiency metasurfaces can be created and behave similarly to those proven utilizing resonant metal structures [2].

Combining the functionality of geometric-phase with metallic antenna and dielectric structures is a profound means of achieving many desirable optical phenomena, and has resulted in the potential real-world applications of lensing, beam-steering, beam-shaping, and holography, as demonstrated in these works. This is the foundation of this thesis.

## **1.2 Generations of Metasurface**

The concept of metasurfaces has evolved over the last two decades, from early works on periodic structures to more recent advances in gradient metasurfaces, and most recently, time modulated metasurfaces for the development of reconfigurable and programmable structures with real-time electromagnetic response control which are described in this section. The historical route of the metasurface concept is depicted in Fig. 1.2 by highlighting the three generations.

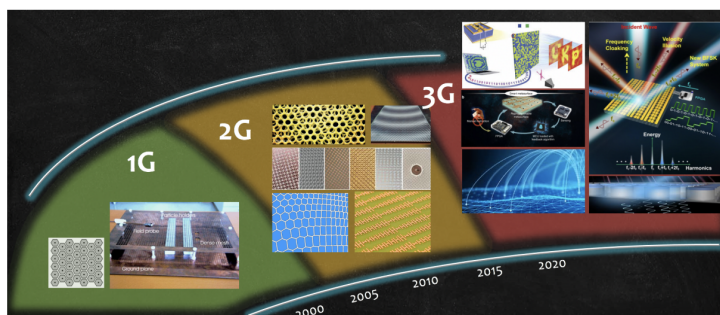


Figure 1.2: The evolution of the metasurface notion across time. Homogeneous periodic structures characterize the first generation of metasurfaces. Inhomogeneous metasurfaces with varied qualities in space make up the second generation of metasurfaces. Metasurfaces of the third generation are either homogeneous or in-homogeneous structures with properties that change over time [7].

### 1.2.1 Metasurface 2.0

In-homogeneous structures (e.g. quasi-periodic, gradient structures, etc.) with homogenized electromagnetic properties that vary point by point describe the second generation of metasurfaces. The reflected and transmitted electromagnetic fields, as well as the radiation from a propagating surface wave, can all be manipulated using these structures. Such structures have been frequently used in the antenna industry as a result of their unusual behavior (e.g. metasurface antennas).

#### Advantages and Disadvantages

Because of the peculiar characteristics of the second generation Metasurfaces, those structures have been widely used in the antenna business. Spatial modulation of the metasurface properties allowed enhancing the capabilities but the Metasurface properties cannot be controlled in both space and time which lead the way to the Third Generation Metasurfaces. The Third generation metasurfaces can be controlled in space and time. This capability is enabled by many control mechanisms (e.g electronic, optical, thermal, chemical, liquid crystal based, etc.) and boosted by recent advancements in integration and micro/nano fabrication technologies.

The ability to control the metasurface's response in real time, in particular, enables the incorporation of awareness and cognitive features into structural elements or objects in the environment, resulting in a significant reduction in signal processing and paving the way for zero latency and ultra-high capacity systems.

## 1.2.2 Metasurface 3.0

Homogeneous and inhomogeneous structures with time-controlled attributes characterize the third generation of metasurfaces. The capacity to control qualities in both space and time enables for the creation of tunable, time-modulated, reconfigurable, and programmable metasurfaces, allowing for the creation of new and unique electromagnetic devices [7].

The environment (e.g., walls, objects, windows, etc.) is regarded as an obstruction in most communication systems, lowering the quality of the received signal. This is especially true as the number of operations becomes more frequent.



Figure 1.3: A vision of a structured intelligent environment made up of metasurfaces whose attributes may be adjusted in real-time [7].

In this case, one feasible approach would be to take advantage of the inevitable interaction between the electromagnetic field and the environment in order to improve the communication system's performance. In other words, if the environment is appropriately structured through the integration of intelligent metasurfaces, whose attributes can be modified in real-time, the environment itself may represent a level of freedom that can be used to improve the performance of future communication systems. In fact, metasurfaces embedded in structural elements or objects that make up the environment can be used to increase awareness of the electromagnetic environment (e.g. by connecting two points that are not in line-of-sight) and to extend the coverage of a communication system (e.g. by connecting two points that are not in line-of-sight) monitoring conflicting signals, their frequency channels, arrival directions, and so on) to fine-tune the features of a source of radiation (e.g. by changing in real-time the radiation pattern, its maxima and nulls, etc. To increase security (for example, by encrypting data through correct

modulation along the propagation path as a result of interaction with a structured intelligent environment), etc. As a result, the majority of the additional signaling required in future communication systems will be performed at the physical layer and at the speed of light, resulting in ultra-high capacity and reduced latency when compared to traditional paradigms. Fig.1.3 depicts a sketch of the authors vision of the organized world.

## **1.3 Smart Radio Environments and Reconfigurable Intelligent Surfaces**

### **1.3.1 Smart Radio Environment**

Nature is in charge of the environment. Current wireless network design methodologies typically focus on optimizing the so-called end-points of communication lines, such as transmitters and receivers.

Though Nature creates the environment, it may be manipulated by design. To compensate for the effect of the wireless channel and/or to capitalize on specific features and characteristics of the wireless channel, the overarching paradigm that characterizes the design of current wireless networks consists of pre-processing the signals at the transmitters and/or post-processing the signals at the receivers. RIS's give wireless researchers more options for creating and optimizing wireless networks, which are based on the wireless environment's diverse role. In reality, after the radio waves are released by the transmitters and before they are viewed by the receivers, RIS's are capable of shaping the radio waves that impinge on them in such a way that the wireless environment can be customized, in principle, to meet specific system requirements. As a result, the wireless environment is not viewed as an uncontrollable random phenomenon, but rather as one of the network design elements that may be optimized to satisfy a variety of performance metrics and quality of service needs.

Models of communication theory are being revisited. As a result, the concept of SRE's brings a novel communication-theoretic understanding of wireless systems and opens up new optimization possibilities. The conceptual block diagram of a traditional point-to-point communication system, as well as the matching block diagram under an SRE-based framework, are shown in Fig.1.4. Under the classical paradigm the system is described using transition probabilities, which are not considered optimization variables in the traditional communication theoretic paradigm. Instead, the system is described using transition probabilities that can be adjusted under the SRE-based communication-theoretic framework, due to the deployment of RIS's across the environment and the ability to control and

program the functions that RIS's apply to the impinging radio waves. As a result, the system model becomes an optimization variable that may be optimized in conjunction with the transmitter and receiver. Rather than optimizing the input signal for a certain system model, the input signal and the system can now be optimized together.

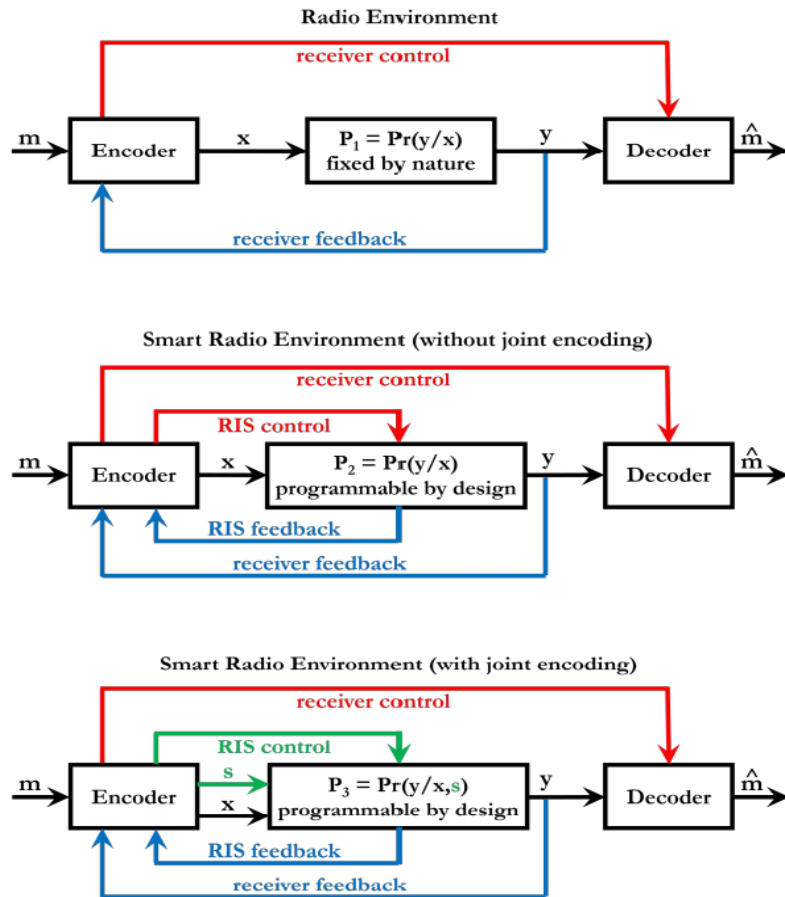


Figure 1.4: Radio environments and smart radio environments have communication-theoretic models (with and without joint encoding) [8].

### 1.3.2 Reconfigurable Intelligent Surfaces (RIS)

RIS is also termed as IRS. RIS/IRS is a revolutionary new technology that improves the performance of wireless communication networks by intelligently changing the electromagnetic propagation environment using enormous low-cost passive reflecting devices placed on a planar surface. Different elements of an IRS, in

particular, can independently reflect the incident signal by changing its amplitude and/or phase, resulting in fine-grained 3D passive beamforming for directional signal augmentation or nulling [11].

The intelligent reflecting surface (IRS) has been described as a promising new technology for software-controlled reflection to reconfigure the wireless propagation environment. IRS, in contrast to existing wireless link adaptation techniques at the transmitter/receiver, adjusts the wireless channel between them proactively by highly adjustable and intelligent signal reflection.

As a result, a new degree of freedom (DoF) is added to wireless communication performance, paving the way for a smart and programmable wireless environment to be realized. Fig.1.5 shows a few examples of IRS-assisted wireless network applications.

The first application concerns a user who is in a dead zone, where the direct connectivity between them and their serving BS is substantially obstructed. In this situation, deploying an IRS with clear links to the BS and user helps avoid the obstacle by generating a virtual line-of-sight (LoS) link between them via intelligent signal reflection. This is especially important for extending coverage in mmWave communications, which are very susceptible to interior blocking.

The second example shows how IRS can be used to improve physical layer security. When the link distance between the BS and the eavesdropper is shorter than the link distance between the BS and the legitimate user (e.g. user 1) or when the eavesdropper is in the same direction as the legitimate user (e.g. user 2), the achievable secrecy communication rates are severely limited (even when transmit beamforming is used at the BS).

In the third application, an IRS can be deployed at the cell edge for a cell-edge user who suffers from both high signal attenuation from its serving BS and severe co-channel interference from a neighboring BS. By properly designing its reflect beamforming, an IRS can help not only improve the desired signal power but also suppress the interference, creating a “signal hotspot” as well as a “interference-free zone” in its vicinity. The fourth application shows how IRS can be used to enable huge device-to-device (D2D) communications by acting as a signal reception hub and allowing for simultaneous low-power D2D broadcasts through interference mitigation. The final application uses IRS to realize simultaneous wireless information and power transfer (SWIPT) to various devices in an Internet-of-Things (IoT) network, where the IRS’s large aperture is used to compensate for significant power loss over long distances via passive beamforming to nearby IoT devices to improve the efficiency of wireless power transfer to them.

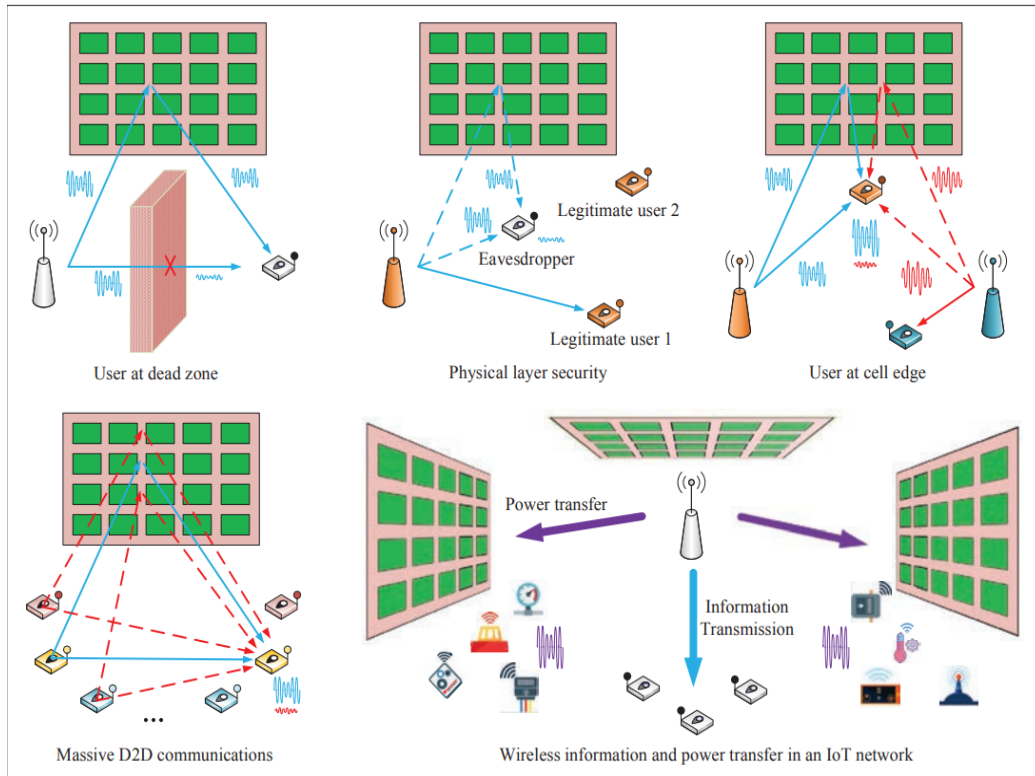


Figure 1.5: IRS applications that are commonly used in wireless networks [11].

Despite its many advantages, the IRS-assisted wireless network has both active (BS, AP, and user terminal) and passive (IRS) components, which distinguishes it from a standard network that solely includes active components.

The so called RIS is a major enabler for realizing the idea of SREs by making the wireless environment programmable and controllable. An RIS is a low-cost adaptive (smart) thin composite material sheet that, like wallpaper, covers sections of walls, buildings, ceilings, and other surfaces and is capable of changing radio waves impinging on it in ways that can be programmed and controlled using external stimuli. As a result, a major feature of RIS's is their ability to be (re)configurable after deployment in a wireless environment [8].

Dependent on this broad definition, the operation of a RIS can be divided into two stages, each of which is carried out at regular intervals based on the environment's coherence time.

- Control and programming phase. The essential environmental information for configuring the RIS's operation is estimated during this phase, and the RIS is configured for subsequent operation.
- Normal operation phase. The RIS is already configured at this point and facilitates in the transmission of other devices across the network.

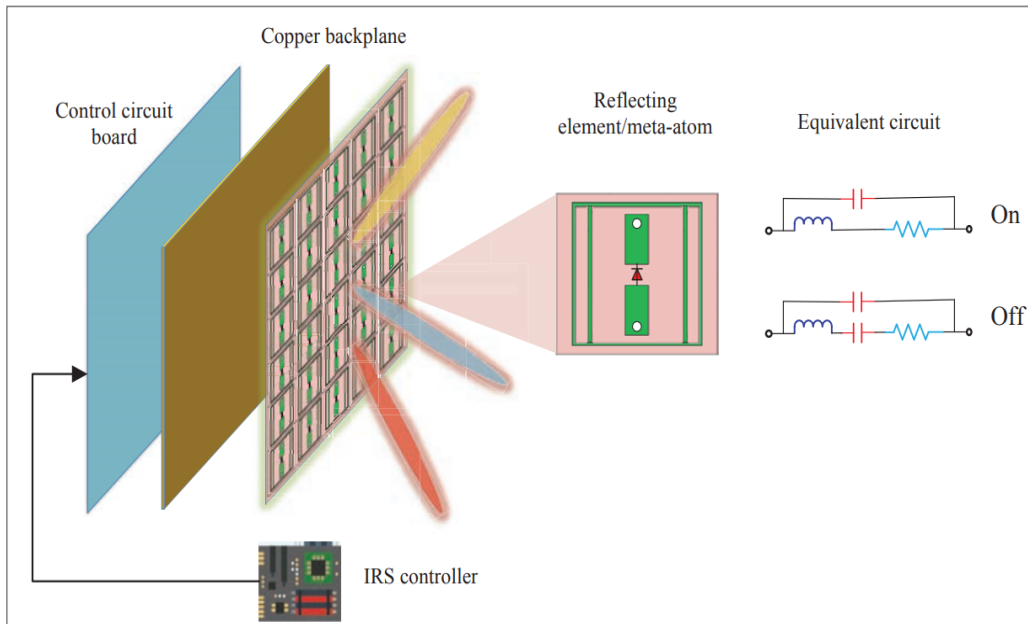


Figure 1.6: IRS Architecture [11].

### 1.3.3 Solutions for RISs

There are two types of RIS's. Although the current state of research may be far from realizing RIS's in the sense of the definition just given, several researchers are working on smart surfaces that function conceptually like programmable thin wallpaper and programmable thin glass and are capable of manipulating radio waves as desired. Figs.1.7 and 1.8 show two current examples of these research initiatives [8].

The *R-Focus* prototype from MIT. The *R-Focus* prototype is represented in Fig.1.7. The *R-Focus* prototype is built up of 3,720 low-cost antennas spread out over a six-square-meter area. Each antenna element is estimated to cost on the order of a few cents or less when scaled up. Because the surface does not create additional radio waves, the structure operates in a nearly-passive mode, but it can be adaptively adjusted using low-power electronic circuits to beam form and focus the impinging radio waves towards specified directions and places, respectively.



Figure 1.7: The RFocus prototype from MIT (photo: Jason Dorfman, CSAIL) [8].

The prototype of NTT DOCOMO. A smart glass prototype, recently designed by researchers at NTT DOCOMO in Japan, is illustrated in Fig.1.8. The manufactured smart glass is a thin layer (metasurface) that is intentionally engineered and consists of a large number of sub-wavelength unit elements arranged in a periodic pattern over a two-dimensional surface covered with a glass substrate. It is feasible to dynamically alter the response of the impinging radio waves in three modes by shifting the glass substrate slightly: (i) complete penetration of incident radio waves; (ii) partial reflection of incident radio waves; and (iii) complete reflection of all radio waves. Because the smart glass is incredibly transparent, it may be used in an unobtrusive manner. It can, for example, alter radio waves in accordance with the installation environment, especially in regions that are not suitable for building base stations, such as densely populated areas or inside spaces where signal reception must be selectively restricted (e.g., high-security areas). Furthermore, the transparent substrate does not obstruct the line-of-sight of the user in any way, either aesthetically or physically [8].

Other major issues in developing and implementing IRS-aided wireless networks from a signal processing and communication standpoint, such as passive beamforming design, IRS channel acquisition, and IRS deployment [11].

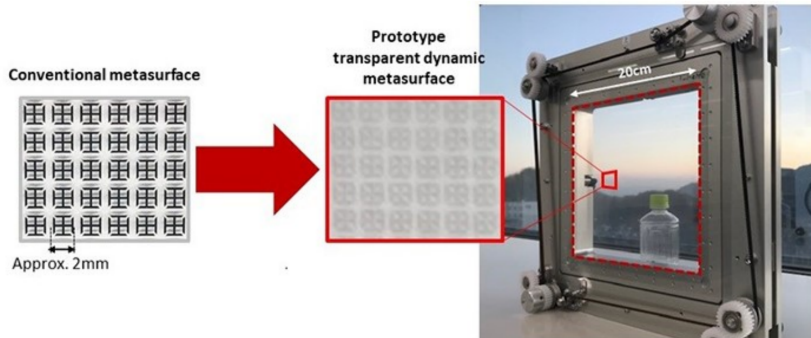


Figure 1.8: The prototype of NTT DOCOMO (photo: NTT DOCOMO) [8].

The discrete amplitude and phase shift levels of each element present a barrier when implementing passive beamforming for IRS in practice. Rather than utilizing exhaustive search, a practical technique is to first loosen such constraints and solve the issue with continuous amplitude/phase shift values, then quantize the resulting answers to their nearest discrete values. To enhance speed even more, the heuristic alternating optimization technique can be used to iteratively optimize each element's discrete amplitude/phase-shift values while fixing the values of all the others at each iteration.

Using machine learning techniques such as Deep Learning (DL) to solve the channel acquisition problem is one possible option. For example, in the training phase, we can deploy IRS's at some carefully chosen reference locations and collect critical performance characteristics like as received signal strength measured at various user locations. The output and input of a DL-based neural network are then trained using IRS locations and relevant performance indicators. The trained DL network is then used to forecast a list of locations for placing IRS's in the deployment phase, using the required performance indicators as input. Following the deployment of IRS's at these locations, a new set of performance metrics can be collected and used to further train the DL network in the future to increase prediction accuracy.

As shown in Fig.1.9 the author of [11] investigate the minimal transmit power necessary at the BS to achieve a target user signal-to-noise ratio (SNR) of 20 dB by altering the value of  $d$ . For starters, moving the user further away from the BS results in higher transmit power due to increasing signal attenuation in the scheme without IRS. However, implementing the IRS, which dramatically improves the SNR when the user is close to it, solves this problem. As a result, a user who is close to either the BS ( $d = 25$  m) or the IRS ( $d = 50$  m) requires less transmit power than a user who is far away from both ( $d = 40$  m).

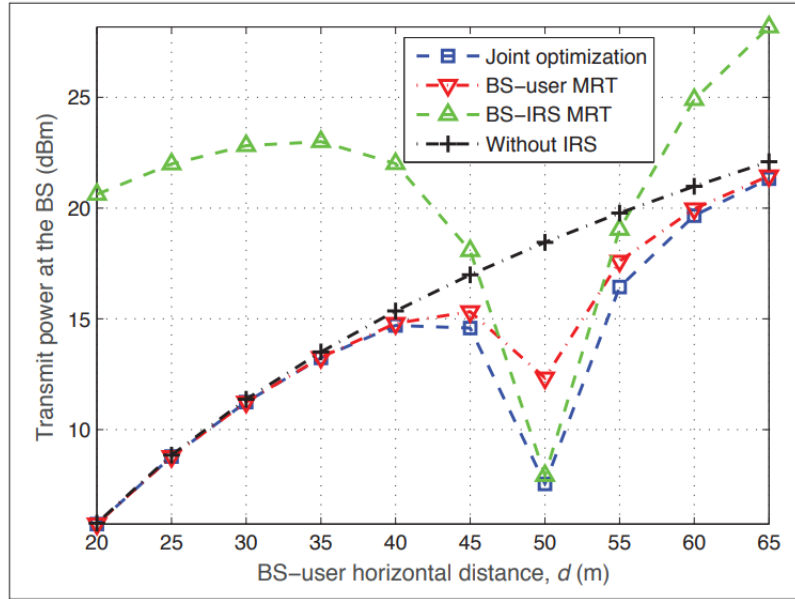


Figure 1.9: BS transmit power vs Horizontal distance between User and BS [11].

Holographic communication is a comprehensive method of manipulating the electromagnetic field with greatest flexibility. New metamaterials developed for the realization of LISs and IRSs as shown in Fig. 1.10 can provide this versatility. In this context, the author have examined the theoretical consequences of employing LISs as active antennas in this article [9], stressing the limitations of current models as well as the potential available when operating in the near-field regime. In reality, whereas only one communication mode may be formed in LoS in the far field, an increasing number of communication modes can be acquired in the near-field region, allowing for enhanced capacity.

Even if some theoretical and technological issues remain to be resolved, new wireless networks operating at millimeter-wave and terahertz are predicted to reap major benefits in terms of enhanced capacity, dependability, and node densification, as explained in this article. By utilizing breakthroughs in EM theory of information, this approach may demand tighter synergy between designs at the digital and EM levels than in the past.

The optimal communication between LIS/SIS is treated as an eigen functions problem in this study [10], starting from an e.m. formulation. Unfortunately, if huge surfaces are considered, finding the solution to the eigen functions problem necessitates extensive and possibly prohibitive em level simulations, which rarely give broad insights. As a result, the author concentrate their efforts on obtaining approximate but correct analytical equations for the link gain and available orthogonal communication channels (i.e., the DoF) between the transmitter and

receiver.

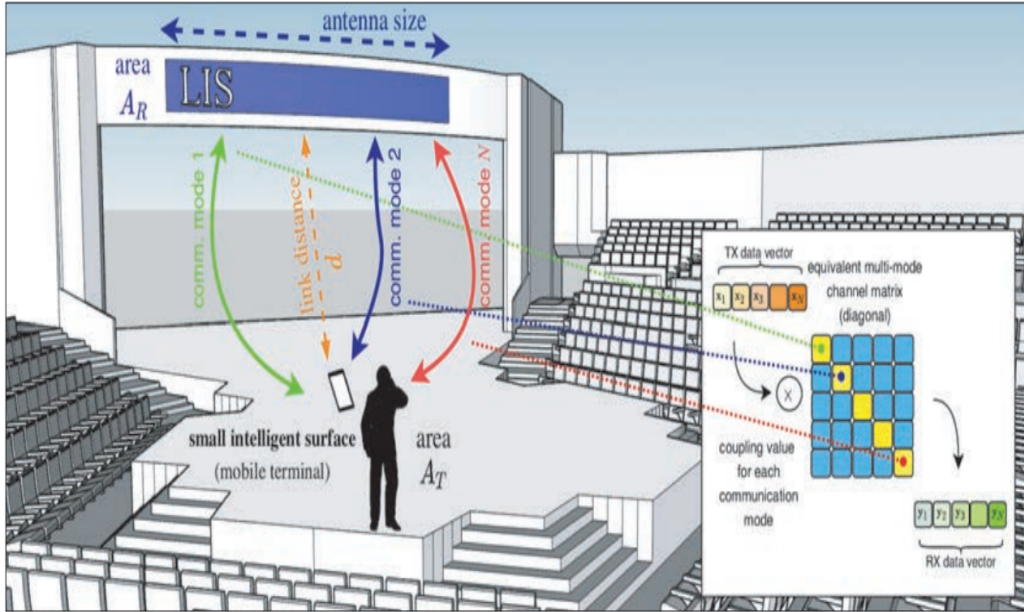


Figure 1.10: Multiple communication modes in LoS conditions, corresponding to parallel channels at the EM level, are used by a LIS to communicate with a mobile terminal equipped with a small intelligent surface [9].

Multiple intelligent reflecting surfaces (IRSs) [12] are deployed to expand the coverage and, perhaps, the rank of the channel in a multi-user multiple-input multiple-output (MIMO) system. The author propose an IRS configuration optimization technique that aims to maximize the network sum-rate by relying solely on statistical characterisation of mobile user's locations. As a result, the proposed approach for IRS optimization does not require the estimation of either instantaneous channel state information (CSI) or second-order channel statistics, easing (or even eliminating) the need for frequent IRS reconfiguration, which is one of the most critical issues in IRS-assisted systems. The proposed method's validity is supported by numerical findings. It is demonstrated, in particular, that IRS-assisted wireless systems that are optimized based on statistical location information nevertheless give significant performance benefits when compared to baseline situations that do not use IRS's.

# Chapter 2

## Development of Metasurfaces

### 2.1 Materials and Methods

#### 2.1.1 Coding Metamaterials

The concept of coding metamaterials underpins all of the findings in this article. To begin, we will use 1-bit coding metamaterials. We investigate a specific metasurface made of binary digital elements of ‘0’ or ‘1’, as shown in Fig.2.1a. The physical realization of digital elements is not unique, but it does necessitate specific responses in order to achieve big phase changes and have a lot of control over EM waves. The highest phase difference in the binary case is  $\pi$  (or  $180^\circ$ ) [3]. As a result, we create a metamaterials particle with a 0 phase response for the ‘0’ element and a meta material particle with a  $\pi$  phase response for the ‘1’ element. The phase responses of the ‘0’ and ‘1’ elements are easily defined as  $\varphi_n = n\pi$  in this fashion ( $n=0, 1$ ). The most basic elements ‘0’, ‘1’ can be used as magnetic and electric conductors. However, to provide a broad frequency band, the binary elements are realized using a sub wavelength square metallic patch printed on a dielectric substrate [3].

The substrate proposed in [3] is  $h = 1.964$  mm thick, with a dielectric constant of 2.65 and a loss tangent of 0.001; the metallic patch is  $t = 0.018$  mm thick, with a width of  $w$ ; and the unit cell’s periodicity is  $a = 5$  mm. In a broad band, the phase difference is about  $180^\circ$  when the patch widths are 4.8 and 3.75 mm. The phase difference varies from  $135^\circ$  to  $200^\circ$  between 8.1 Ghz and 12.7 GHz (it is exactly  $180^\circ$  at 8.7 and 11.5 GHz).

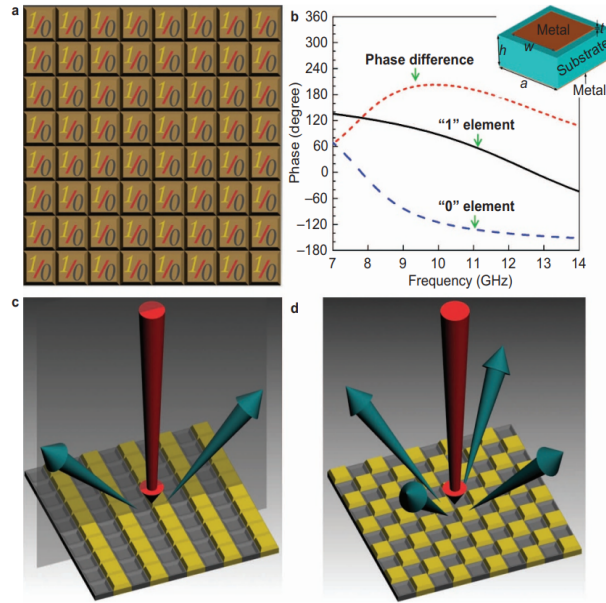


Figure 2.1: The coding metasurface and the 1-bit digital metasurface. (a) 1-bit digital metasurface: ‘0’ and ‘1’. (b) A square metallic patch unit structure for realizing the ‘0’ and ‘1’ elements. (c, d) Two 1-bit periodic coding metasurfaces for controlling beam scattering by designing ‘0’ and ‘1’ element coding sequences: (c) 010101.../010101... and (d) 010101.../ 101010... codes [3].

As a result, the author of [3] constructed the metasurface using patch particles with  $w = 54.8$  mm as the ‘0’ element and  $w = 3.75$  mm as the ‘1’ element, both of which are easily produced in a single-layered dielectric board. It is worth noting that the ‘0’ element’s absolute phase response may not be 0 at a given frequency, but this has no bearing on physics because the phase may be normalized to 0.

Unlike analog metamaterials that regulate EM fields using effective medium characteristics or unique dispersion relations, coding metamaterials will simply modify EM waves using alternative coding sequences of ‘0’ and ‘1’ elements. The normally incident beam will mainly be reflected to two symmetrically oriented directions by the metasurface under the periodic sequence 010101.../010101... whereas the normally incident beam will mainly be reflected to four symmetrically oriented directions under the periodic sequence 010101.../101010.../010101.../101010... as illustrated in Fig.2.1 c and d.

To illustrate the foregoing physical phenomena mathematically, consider a general square metasurface with  $N \times N$  equal-sized lattices of dimension  $D$ , each of which is inhabited by a sub-array of ‘0’ or ‘1’ components. The distribution of ‘0’ and ‘1’ lattices is flexible. Each lattice’s scattering phase is considered to be

$\varphi(m, n)$ , which is either  $0^\circ$  or  $180^\circ$ .

The far-field function scattered by the metasurface under normal incidence of plane waves is written as:

$$f(\theta, \varphi) = f_e(\theta, \varphi) \cdot \sum_{m=1}^N \sum_{n=1}^N \exp\{-i\{\varphi(m, n) + kD \sin \theta [(m - \frac{1}{2}) \cos \varphi + (n - \frac{1}{2}) \sin \varphi]\}\} \quad (2.1)$$

The metasurface's directivity function  $Dir(h, Q)$  can be written as

$$Dir(\theta, \varphi) = 4\pi |f(\theta, \varphi)|^2 / \int_0^{2\pi} \int_0^{\pi/2} |f(\theta, \varphi)|^2 \sin \theta d\theta d\varphi \quad (2.2)$$

Equations (2.1) and (2.2) are used to create complex coding sequences that enable coding metasurfaces to perform sophisticated functions. The coding metamaterial concept can be expanded from 1-bit coding to 2-bit coding and beyond. To simulate the '00', '01', '10', and '11' elements in 2-bit coding, four types of unit cells with unique responses are required. 2-bit coding allows for more latitude in manipulating EM waves than 1-bit coding, but it necessitates more complex digital control technologies.

## 2.1.2 Digital Metamaterials

We can control EM waves by changing the coding sequences of '0' and '1' (or '00', '01', '10', and '11') elements, as well as develop true digital metamaterials and programmable metamaterials, using the notion of coding metamaterials. The particle's entire volume is  $6 \times 6 \times 2 \text{ mm}^3$ , which corresponds to  $0.172 \times 0.172 \times 0.057 \lambda^3$  at the center frequency. DC voltage can be used to control the biased diode. The diode is 'ON' when the biased voltage is 3.3 V, and the corresponding effective circuit is shown in Fig.2.3a; when the biased voltage is not present, the diode is 'OFF' and the corresponding circuit model is shown in Fig.2.3 b. When the diode is on, the metamaterial particle behaves as a '1' element and when the diode is off, it behaves as a '0' element, according to the numerical results obtained by inserting the circuit models into CST Microwave Studio. The phase difference in the frequency region from 8.3 to 8.9 GHz is roughly  $180^\circ$  as shown in Fig.2.4b. The phase difference at 8.6 GHz is exactly  $180^\circ$ .

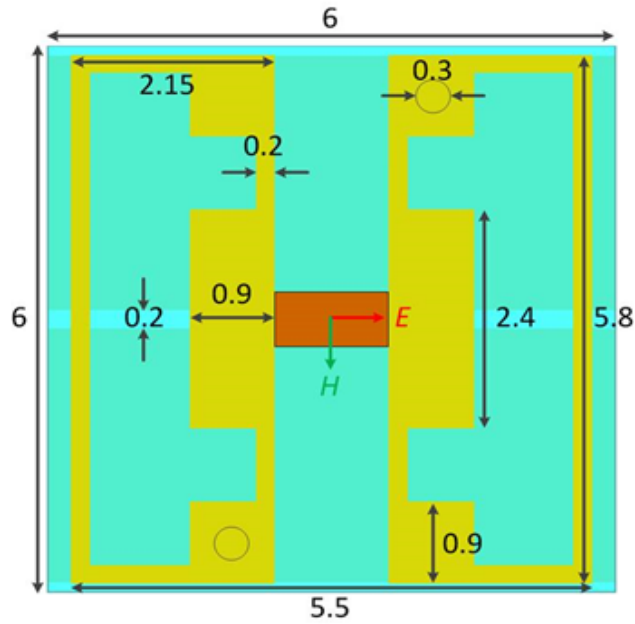


Figure 2.2: Top view of the one-of-a-kind metamaterial particle used to create a digital metasurface, with specific geometrical characteristics [3].

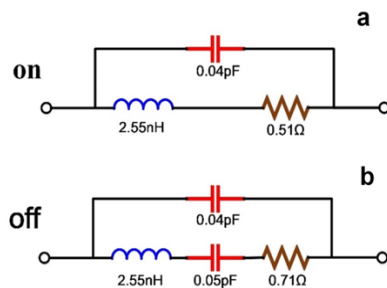


Figure 2.3: The biased diode's effective circuit models in the "on" and "off" states. (a) The 'on' condition. (b) The 'off' condition [3].

The design and construction of a sample of a 1-bit digital metasurface based on the metamaterial particle, as shown in Fig.2.5 a,c and d. The digital metasurface is made up of 30x30 equal unit cells, each with a biased diode (Fig. 2.5d). A control voltage is shared by five adjacent columns of unit cells, each of which corresponds to a single bit of the control words. As a result, this is a one-dimensional (1D) digital metasurface with six control words in the coding sequence. To demonstrate the ideas, the following four coding sequences are used: 000000, 111111,

010101, and 001011. Fig.2.6a-d show the simulation results of 3D scattering patterns from 1D digital metasurfaces, respectively. The regularly incident beams are directly reflected back with the coding sequences 000000 and 111111, as shown in Fig.2.6a and b, since they exactly resemble electric and magnetic conductors. The regularly incident beam is largely reflected in two directions by the metasurface under the periodic coding sequence 010101, as shown in Fig.2.6c.

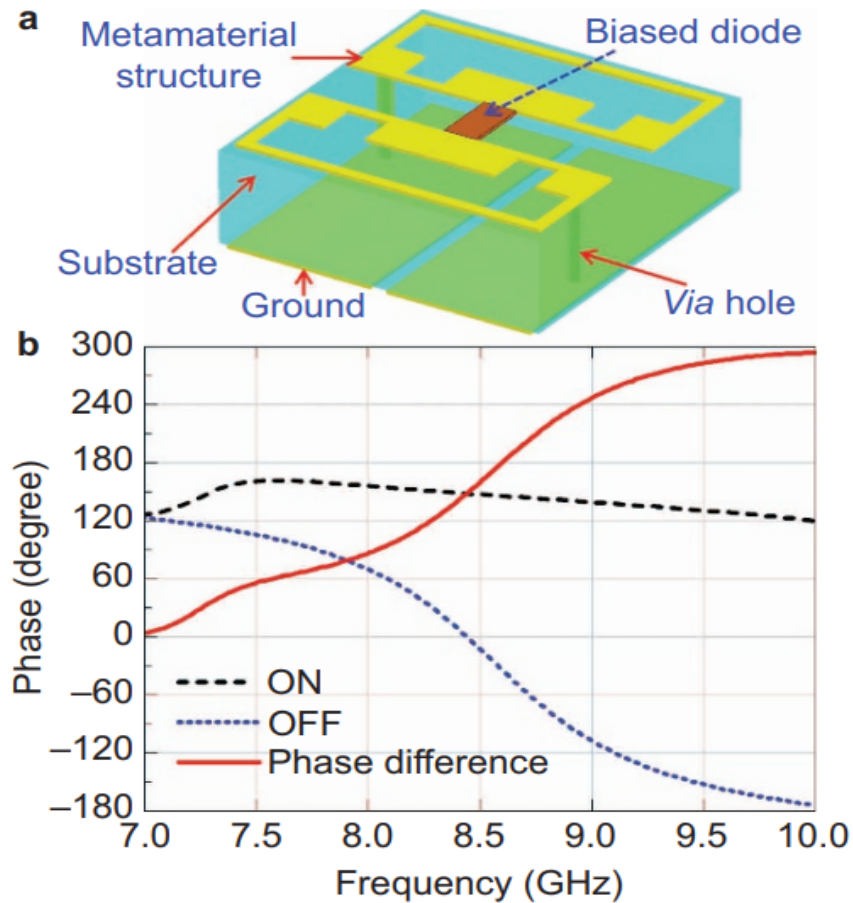


Figure 2.4: The metamaterial particle for realizing the digital metasurface and the corresponding phase responses. (a) The structure of the metamaterial particle, which behaves as '0' and '1' elements when the biased diode is 'OFF' and 'ON', respectively. (b) The corresponding phase responses of the metamaterial particle as the biased diode is 'OFF' and 'ON' over a range of frequencies [3].

### 2.1.3 Programmable Metamaterials

The author in [3] designed and implemented FPGA technology to digitally regulate the coding sequences as shown in Fig.2.5. Four switches serve as triggers for various coding sequence controls. When one of the switches is turned on, the FPGA generates the corresponding coding sequence. As a result, we may change the voltage distributions on the metasurface digitally by toggling different triggers, which control the biased diode's 'ON' and 'OFF' states, resulting in the appropriate '0' and '1' states of the digital metasurface. As a result, the FPGA program controls different functions on the unique metasurface, resulting in a programmable metasurface.

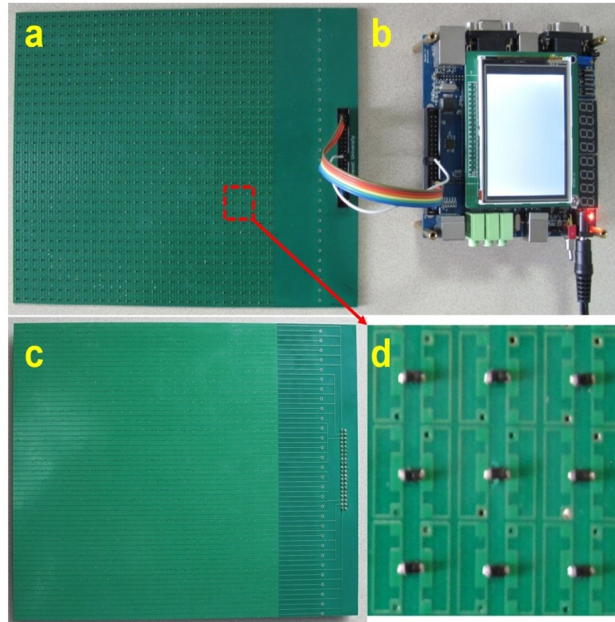


Figure 2.5: FPGA-controlled fabrication of a 1D digital metasurface. (a) The 1D digital metasurface from above. (b) FPGA (Field Programmable Gate Array). (c) The 1D digital metasurface from the bottom. (d) A zoomed image of the one-dimensional digital metasurface [3].

Fig.2.6i depicts the flow chart of the FPGA-triggered programmable metasurface. Experiments were carried out to verify that a single metasurface can influence EM waves in different ways. Fig.2.6e - 2.6h shows the measured scattering patterns of the 1D digital metasurface generated by activating coding sequences 000000, 111111, 010101, and 001011 with FPGA. Multiple functionalities are readily visible in these pictures, which are in good agreement with the numerical simulations presented in Fig's. 2.6a - 2.6d.

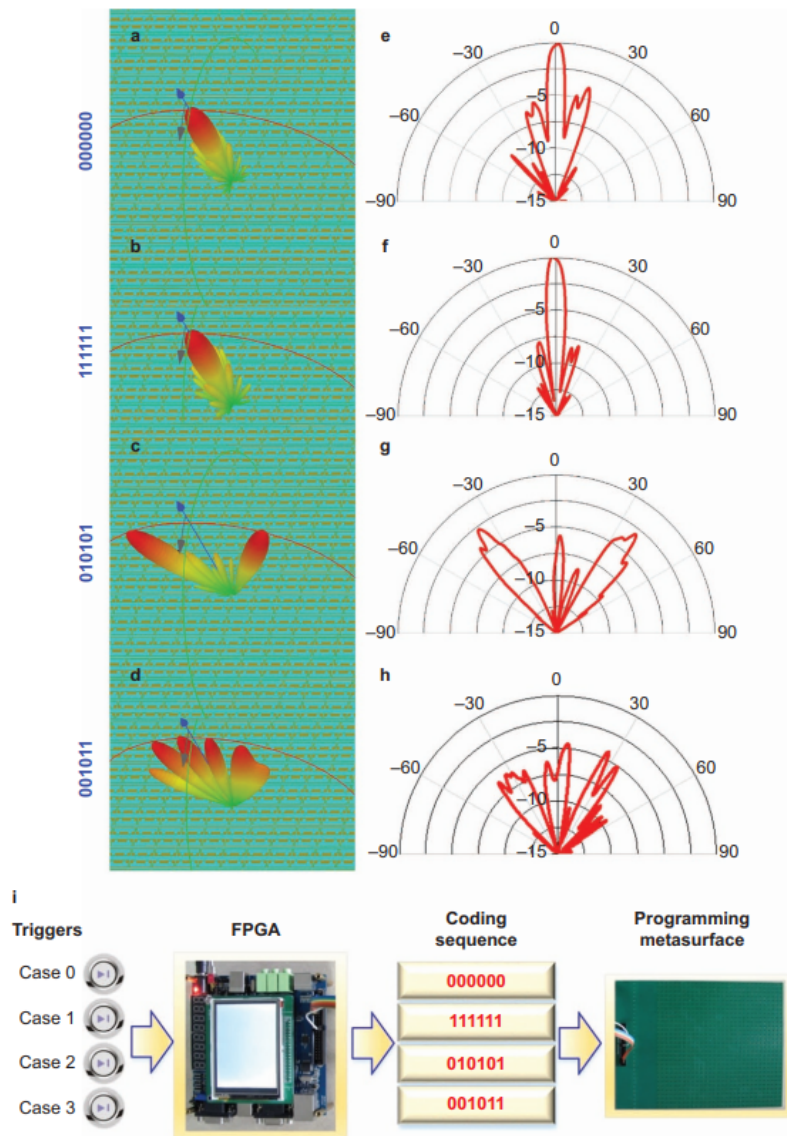


Figure 2.6: (a-d) Numerical simulation results of scattering patterns at 8.3 GHz for the 1D digital metasurface under different coding sequences: (a) 000000, (b) 111111, (c) 010101 and (d) 001011. (e-f) Experimental results of scattering patterns at 8.6 GHz for the 1D digital metasurface under different coding sequences: (e) 000000, (f) 111111, (g) 010101 and (h) 001011. (i) A flow diagram for realizing a programmable metasurface controlled by the FPGA hardware [3].

## 2.2 Dynamic Metasurface Antennas

In the article “Dynamic Metasurface Antennas for 6G Extreme Massive MIMO Communications” [13] an alternative application of metasurfaces for wireless communications as active reconfigurable antennas with advanced analog signal processing capabilities for next generation transceivers is presented. Recent research initiatives on novel transceiver hardware architectures and appropriate communication algorithms have been sparked by the increasingly demanding objectives for communications. Large numbers of Electro Magnetic (EM) radiating devices are used in such hardware architectures, paving the way for Multiple-Input Multiple-Output (mMIMO) communications. With relatively simple signal processing methods, a mMIMO system with an arbitrarily large number of antenna elements can deliver significant gains in spectral efficiency.

The number of nodes connected by wireless media is predicted to reach the tens of billions in the next several years, thanks to the widespread deployment of Internet of Things (IoT) devices. Future wireless networks are likely to transition into dense installations of coordinating extreme mMIMO transceivers to satisfy this huge connection, high peak vice rates, and enhanced throughput requirements.

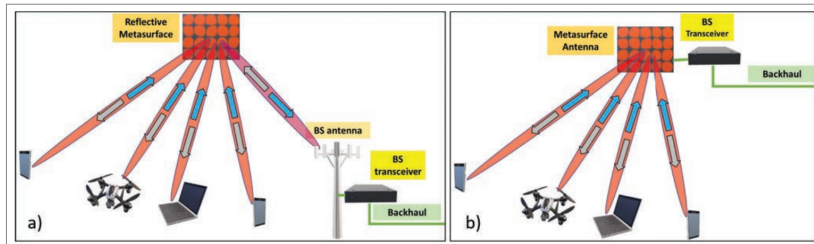


Figure 2.7: Two applications of reconfigurable metasurfaces in multi-user mMIMO wireless communications: downlink (gray arrows) and uplink (blue arrows): a) as near-passive reflective surfaces; b) as active transceiver antenna arrays [13].

Metamaterials enable flexible and dynamically customization processing of transmitted and received signals in the analog domain using minimal transceiver hardware, allowing for beam tailoring. Furthermore, when compared to traditional antenna arrays (i.e., those based on patch arrays and phase shifters), DMA-based architectures require far less power and expense, obviating the need for sophisticated corporate feed and/or active phase shifters. For a wide range of operating frequencies, DMAs can include a large number of tunable metamaterial antenna elements that can be packed into small physical regions. These qualities, namely

their capacity to construct flexible antenna topologies with a large number of elements of reduced size, cost, hardware complexity, and power consumption, are coupled.

In the context of wireless communications, two basic forms of dynamically tuned metasurfaces have recently been considered, as shown in Fig.2.7. Passive reflective surfaces and active antenna arrays are two examples. The first type builds on metasurfaces capacity to construct changeable reflection patterns. By successfully changing EM signal propagation, such passive metasurfaces are commonly used to facilitate and improve communication between the BS and many users in urban or indoor contexts.

The use of a metasurface allows the entire communication system to overcome difficult non-line-of-sight conditions and boost coverage. The metasurface can be placed within a minimal distance from the BS or the users to achieve this purpose without boosting transmission power. Traditional relaying techniques (i.e. neither power amplification nor baseband signal processing) are not used on such reflecting surfaces. Instead, they simply reflect the impinging signal in a controllable manner.

Passive reflective metasurfaces can also be used as part of a larger transceiver design (similar to a reflect array), allowing information to be embedded in the form of reflection modulation in the customizable reflection pattern. In light of the dynamic wireless environment, nearly passive reconfigurable intelligent surfaces require some level of control to adjust the impinging EM wave. This is accomplished by incorporating a digital control unit capable of fine tuning metamaterial elements to generate desired reflection patterns.

DMA's are made up of a slew of reconfigurable metamaterial radiating devices that can function as both broadcast and receive antennas. Those elements are mounted on a waveguide, which is coupled to the digital processor by dedicated inputs and outputs, and through which the signals to be conveyed are transmitted. Multiple distinct waveguide-fed element arrays, referred to as 1-Dimensional (1D) waveguides, are connected to a single input/output port in a shared DMA architecture as shown in Fig.2.8.

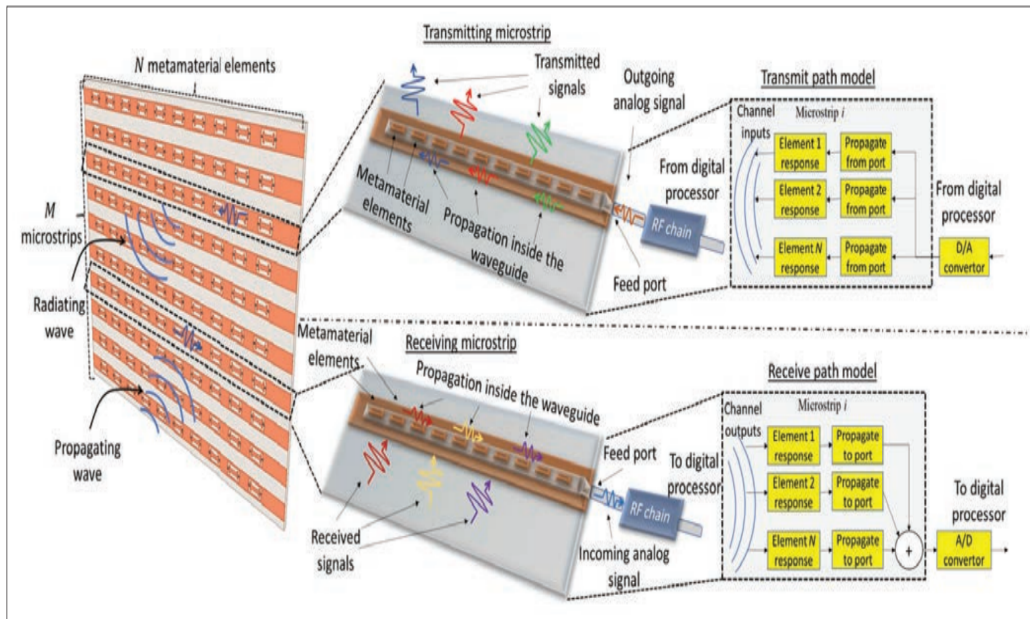


Figure 2.8: An N-element DMA made up of M microstrips, each of which is implemented as a one-dimensional waveguide. The upper right and bottom right halves of the diagram show how they work during transmission and reception, respectively, as well as their analogous signal route models [13].

The two qualities emerging from the DMA architectural metamaterial element acts as a resonator whose frequency response is specified by a Lorentzian equation determine relationships between radiating signals and those captured/fed at the input/output port of each waveguide.

- oscillator strength, damping factor
- The elements can be set to produce a variety of responses, from bandpass to frequency flat filters, and the resonance frequency can be adjusted.

Because part of the processing of transmitted and received signals is done in the analog domain as an inevitable result of the waveguide fed metamaterial array architecture, DMA based transceivers employ a hybrid A/D beamforming. The BS may use a significantly larger number of metamaterial elements than the number of digitally processed data streams because to hybrid processing, which in traditional mMIMO designs requires additional dedicated gear. In mMIMO BS's, this intrinsic expansion during transmission and compression while reception is often desired as a way to reduce the number of expensive RF chains, while achieving enhanced beamforming gain, and to facilitate efficient operation under low quantization requirements.

DMA's are capable of beamforming in a similar way to traditional phased array antennas, but with far lower power consumption and cost. To better demonstrate this notion, consider that a DMA's radiation pattern is the superposition of the radiated fields from several metamaterial radiators, the complex amplitude of which is determined by two factors: the element's tunable resonance response and the phase accumulated by the guided wave. The tuning states of metamaterial element's can be designed to create beams in any direction of interest using simple holographic techniques.

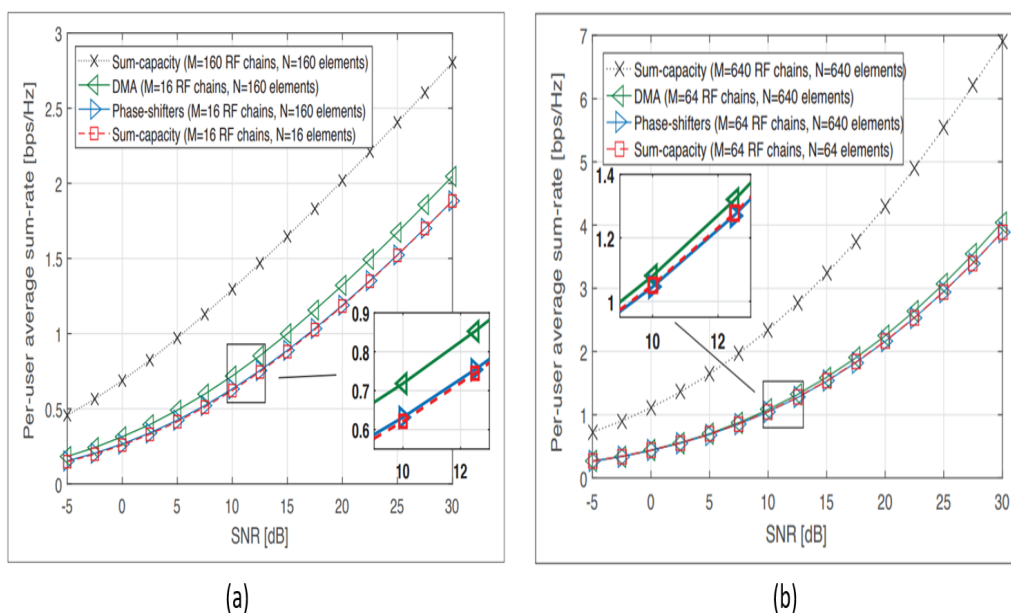


Figure 2.9: (a)Uplink sum-rate performance in bps/Hz versus SNR in dB for a 160-antenna mMIMO BS with 16 RF chains serving 64 users simultaneously within a 400m radius(b)Uplink sum-rate performance in bps/Hz versus SNR in dB for a 640-antenna mMIMO BS with 64 RF chains serving 64 users simultaneously within a cell with a 400m radius [13].

As a result, a highly sampled waveguide has enough degrees of freedom to construct any required beamforming pattern. The DMA architecture, as shown in Fig.2.9 a,b achieves sum-rate performance that is closer to the sum-capacity with  $M = N$  than conventional hybrid A/D architectures based on fully-connected networks of phase shifters.

## 2.2.1 DMA for Near Field Communication

When large arrays and higher transmitted frequencies are coupled, communicating devices commonly operate in the near-field (Fresnel) region, as opposed to conventional networks, which typically operate in the far-field. When communication systems operate in the mmWave/THz bands, for example, the nearfield distance for relatively small antennas/surfaces can be several dozens of meters, implying that the far-field model, which assumes plane wave-fronts of the EM field rather than spherical ones, no longer holds at practical distances. In contrast to merely a single direction as in far-field conditions, managing the spherical wavefront of the signals allows the beam to be focused (beam focusing ) towards a specified spot.

In this article [14], the authors look at multi-user downlink MIMO systems that operate in the near-field and have a DMA on the base station as interested in using DMA's for near-field transmissions, as well as assessing their ability to produce focused beams and the impact of such an operation on downlink multi-user systems.

The authors first develop a mathematical model for DMA-based near-field multi-user MIMO systems, which takes into account both DMA processing and the propagation of transmitted EM waves in near-field wireless communications. Then, while accounting for the distinctive Lorentzian-form response of metamaterial elements, optimize the DMA weights, which dictate its transmission pattern, and the digital precoding vector together to maximize the sum-rate when working in near-field.

The authors start with a single-user instance to develop the near-field transmission pattern based on the sum-rate target and specifically characterize the DMA configuration and the pre-coding vector for such systems. Then, in the case of multiple users, where the resulting optimization issue is non-convex, author suggest an alternating design algorithm [14] based on the single-user analyses principles. which demonstrate the suggested design's ability to focus beams and also show that by utilizing DMA's beam focusing capabilities, it is possible to reliably communicate with many users in the same angular direction with varied ranges, which is not possible with traditional beam steering techniques.

The baseband signal that the DMA output transmits is given by

$$s = HQz \quad (2.3)$$

where  $s \in \mathbb{C}^N$  denotes the DMA output signal vector and  $\mathbf{Q} \in \mathbb{C}^{N \times N_d}$  denotes the DMA's customizable weights

$$Q_{(i-1)N_e+l,n} = \begin{cases} q_{i,l} & i = n \\ 0 & i \neq n \end{cases} \quad (2.4)$$

As shown in Fig.2.10, author examine a downlink multi-user MIMO system in which a DMA-based BS communicates with  $M$  single-antenna receivers. Author concentrate on near-field operation, which is defined as a distance between the BS and the users that is less than the Fraunhofer distance  $d_F \triangleq 2D^2/\lambda$ , where  $D$  and  $\lambda$  are the antenna diameter and wavelength, respectively.

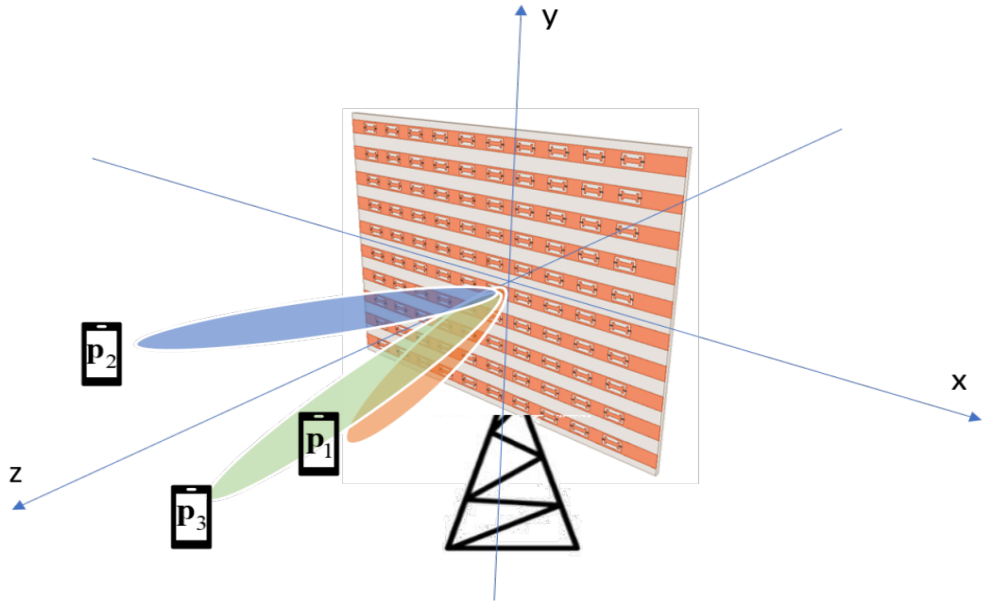


Figure 2.10: DMA focusing for multi-user communications in close proximity [13].

Let  $x_m$  be the data symbol meant for the  $m$ th user,  $m \in 1, 2, \dots, M \triangleq \mathcal{M}$ ,  $z = \sum_{m=1}^M w_m x_m$  is the DMA input signal, where  $w_m \in \mathbb{C}_d^N$  is the digital precoding vector for  $x_m$ . Substituting this for  $s$  results in

$$s = \sum_{m=1}^M H Q w_m x_m \quad (2.5)$$

The received signal of the  $m$ th user is represented as using the expression for the channel input  $s$  is

$$r(\mathbf{p}_m) = a_m^H \sum_{j=1}^M H Q w_j x_j + n_m, \forall m \in \mathcal{M} \quad (2.6)$$

where  $n_m$  is Gaussian noise,  $a_m = [A_{1,1}(\mathbf{p}_m) e^{-jk|\mathbf{p}_m - \mathbf{p}_{1,1}|}, \dots, A_{N_d, N_l}(\mathbf{p}_m) e^{-jk|\mathbf{p}_m - \mathbf{p}_{N_d, N_l}|}]^H$

The vector  $a_m$  encapsulates the near-field operation. When the far-field approximation holds, all of the component's outputs undergo the same path loss and phase shift, resulting in identical entries in  $a_m$  in (2.6). The diversity in near-field  $a_m$  entries allows the beam to be focused at a specific location in space rather than simply steered at a particular angle, as in the far-field. To achieve this focusing, the weights  $Q$  of the DMA and the precoding vectors  $w_j$  in (2.6) must be designed together so that the signals delivered by all the elements are summed up coherently in  $\mathbf{p}_m$ .

Authors examine multi-user communications in the near-field based on the aforesaid concept and are particularly interested in the prospect of achieving reliable connections when multiple users are facing the same direction but are at different distances from the BS. The goal is to collaboratively design the transmitter operation, encompassing both digital precoding and DMA configuration, in order to maximize the sum-rate attainable.

While the study focuses on beam focusing, the DMA is designed to establish dependable high-rate connections rather than generate focused beams. The notion that author working in the near-field, which is where the beam focusing ability comes from, is implicitly encoded in the objective via  $a_m$ .

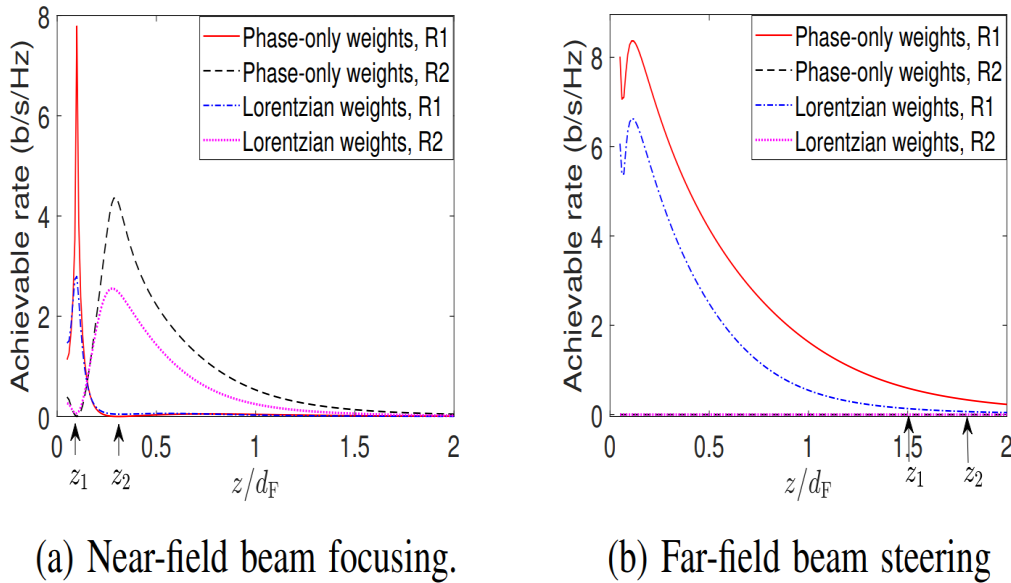


Figure 2.11: The achievable rates of each of the users, i.e., R1, R2 [13].

Authors conclude from Figs.2.11(a) and 2.11(b) that the suggested DMA-based near-field beam focusing design allows to communicate with numerous

users in the same angular direction at the same time, which is not possible with conventional beam steering.

## 2.3 Time-controlled metasurfaces for Frequency conversion

In this article a time-varying metasurface capable of manipulating the frequency of the incident field is proposed [16]. This feature is used to perform an artificial Doppler effect considering a planar metasurface whose electromagnetic response varies over time and which can be modeled through surface admittance  $Y_s(t, f)$ . Assuming that the electromagnetic response of the metasurface is around the frequency of the incident wave  $f_i$ , there is a minor reliance on the same and that the frequency  $f_m$  with which it varies over time is much smaller than  $f_i$ , then it can be assumed that the metasurface has the same surface properties for both the incident and the reflected field. This allows to neglect the dependence of the superficial admittance on the frequency, simplifying the mathematical treatment. [16] The considered situation is shown in Fig.2.12 (a), where the incident field  $e_i(z, t)$  and that transmitted  $e_r(z, t)$ , for  $z = 0$ , have the following form

$$e_i(z = 0, t) = E_i e^{j2\pi f_i t} \quad (2.7)$$

$$e_r(z = 0, t) = E_r e^{j2\pi f_r t} \quad (2.8)$$

The whole system can be simply modeled using the equivalent transmission line shown in Fig.2.12 (b). In this model, the incident and reflected fields are linked together by the reflection coefficient  $\gamma(t)$

$$\gamma(t) = \frac{Y_0 - Y_s(t)}{Y_0 + Y_s(t)} \quad (2.9)$$

where is it  $Y_0 = \frac{1}{Z_0}$  and the admittance of the vacuum. Since in general the reflection coefficient is a complex function of time, it can be expressed as:

$$\gamma(t) = |\gamma(t)| e^{j\phi(t)} \quad (2.10)$$

On the metasurface interface, for  $z = 0$ , the relationship between the incident electric field and the transmitted one will be

$$e_r(t) = \gamma(t) e_i(t) \quad (2.11)$$

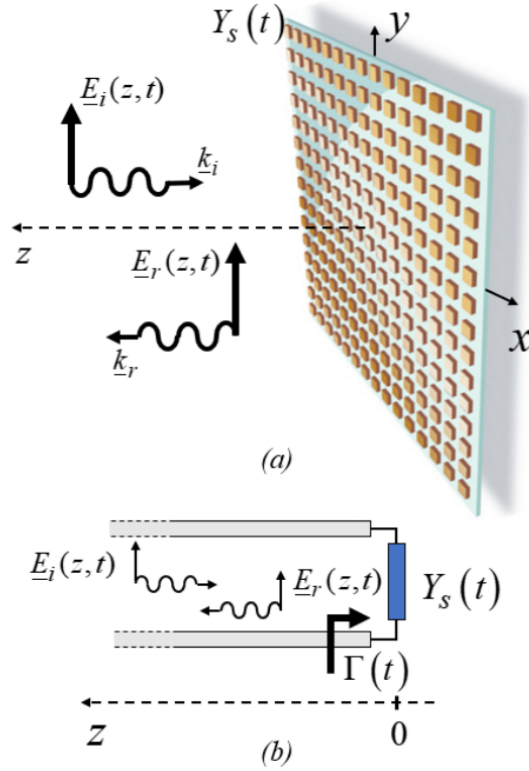


Figure 2.12: (a) A typically impinging electromagnetic field with frequency  $\omega_i = c_0 k_i$  and propagating in the negative  $z$ -direction illuminates a metasurface with a time-varying surface admittance  $Y_s(t)$ . A field reflected back with a different frequency  $r = c_0 k_r$ . (b) A model of the system's equivalent transmission line is shown in Fig.2.12 (a) [16].

The time-variant profile of the reflection coefficient  $\gamma(t)$ , being periodic, can be expanded into Fourier series such as

$$\gamma(t) = \sum_{n=-\infty}^{+\infty} c_n e^{j2\pi f_m n t} \quad (2.12)$$

where  $f_m$  is the fundamental frequency of the reflection coefficient and  $c_n$  are the coefficients of the Fourier series expansion. From the expressions of the reflected and incident field (2.7), (2.8) and from the relationship (2.11) it is possible to obtain the following expression of the reflection coefficient

$$\gamma(t) = \frac{e_r(t)}{e_i(t)} = \frac{E_r}{E_i} e^{j2\pi(f_r - f_i)t} \quad (2.13)$$

Assuming that there are no losses and that the difference between the frequency of the incident and reflected field is small, then the amplitude of the reflection coefficient is approximately unitary at all instance  $t$ . It follows that the coefficient  $\gamma(t)$  in (2.13) is a phasor that rotates in the complex plane with frequency  $f_r - f_i$ . Comparing (2.13) with (2.12) for  $n = 1$  it can be deduced that the absolute value of the frequency difference between the incident and the reflected field is equal to the fundamental frequency of the reflection coefficient.

$$f_m = |f_r - f_i| \quad (2.14)$$

It therefore appears that

$$\gamma(t) = e^{j2\pi f_m t} \quad (2.15)$$

Being the modulus of the reflection coefficient in (2.15) unitary, the metasurface is passive. Equating the equations (2.15) and (2.9) and by making the superficial admittance explicit we obtain that

$$Y_s(t) = -jY_0 \tan(\pi f_m t) \quad (2.16)$$

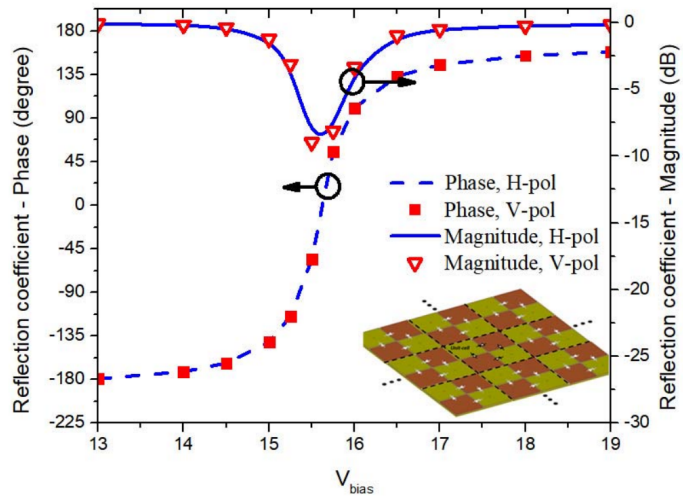


Figure 2.13: For both polarizations of the impinging electromagnetic field, the amplitude and phase of the reflection coefficient as a function of polarization voltage  $V_{\text{bias}}$ .  $F_i = 1.5$  GHz is the lighting frequency [16].

As expected, since the system is lossless, the surface admittance is purely imaginary and exhibits a capacitive or inductive behavior based on the sign of the tangent. In a period  $T_m = 1/f_m$ ,  $Y_s(t)$  assumes all possible values, varying from 0 to  $\pm\infty$ . In particular, these two extreme values correspond respectively to a perfect

magnetic and electrical conductor. A high impedance surface (high-impedance surface (HIS)), an electrically thin metal structure that prevents alternating currents from flowing within a certain frequency band, behaving like a perfect magnetic conductor. Outside this band, the surface behaves like a perfect electrical conductor. The metasurface response can be varied by reverse biased, voltage controlled varactor diodes.

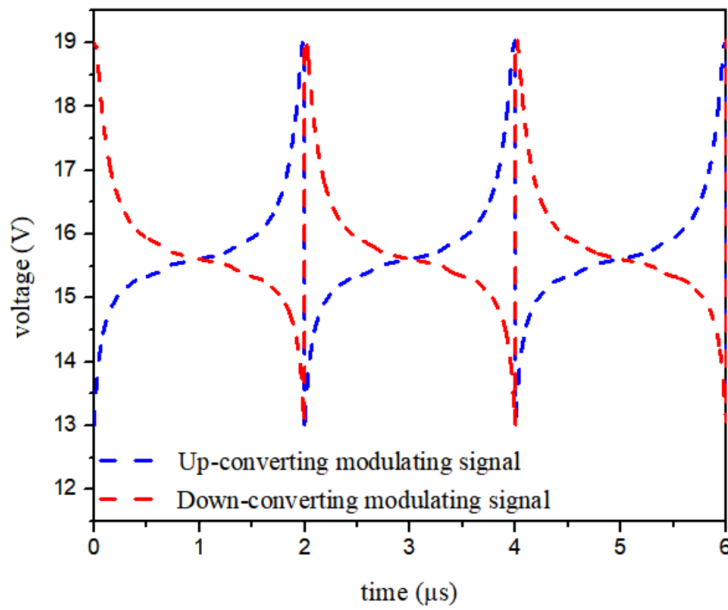


Figure 2.14: Up and down-conversion are achieved by driving voltage modulating signals at a frequency of  $f_m = 500$  kHz (blue and red dashed lines, respectively) [16].

Fig.2.13 shows the reflection coefficient of the metasurface as a function of the polarization voltage for an illumination frequency  $f_i = 1.5$  GHz, from which it can be deduced that the phase varies between  $-180^\circ$  and  $+160^\circ$  (due to the saturation of the capacitance of the varactor diodes at high voltages, this phenomenon occurs) and that the module is non-unitary at zero phase. In Fig 2.14 the trend over time of the bias voltage is reported to obtain the time profile of the surface impedance reported in (2.16).

## 2.4 Time-modulated metasurfaces for Frequency Translation

In “Serrodyne frequency translation using time-modulated metasurfaces” [17] the authors present a time-varying metasurface capable of carrying out a frequency translation of the incident electromagnetic wave without generating unwanted images. The translation in frequency is carried out using the method “serrodyne” which exploits a medium characterized by a saw-tooth phase variation. The metasurface is treated as a time-varying medium adapted to the impedance of the vacuum  $Z_0$ , which presents a permittivity  $\epsilon_r(t)$  and a permeability  $\mu_r(t)$  variable over time, by means of a control signal applied from the outside on the varactor diodes integrated on both sides of the surface. In order for you to have adaptation with  $Z_0$ , it must result that the ratio between the magnetic permeability and the electrical permittivity is unitary in every instant of time

$$\frac{\mu_r(t)}{\epsilon_r(t)} = 1 \quad (2.17)$$

This observation excludes only the refractive index  $n(t)$  of the medium can be varied periodically over time, modifying the values of  $\epsilon_r(t)$  And  $\mu_r(t)$ . Indicating with  $f_m$  the fundamental frequency of  $n(t)$ , it is possible to develop the latter in a Fourier series.

$$n(t) = \sqrt{\epsilon_r(t)\mu_r(t)} = \sum_{k=-\infty}^{+\infty} c_k e^{j2\pi k f_m t} \quad (2.18)$$

where  $c_k$  are the coefficients of the Fourier series expansion of  $n(t)$ . From the definition given in (2.18) we deduce that the refractive index is non-negative. The article examines the situation shown in Fig.2.15, in which the metasurface is illuminated by a monochromatic plane wave that propagates in the direction normal to the surface. At the interface with the vehicle, for  $z = 0^-$ , the incident wave  $e_i(z, t)$  has the following form.

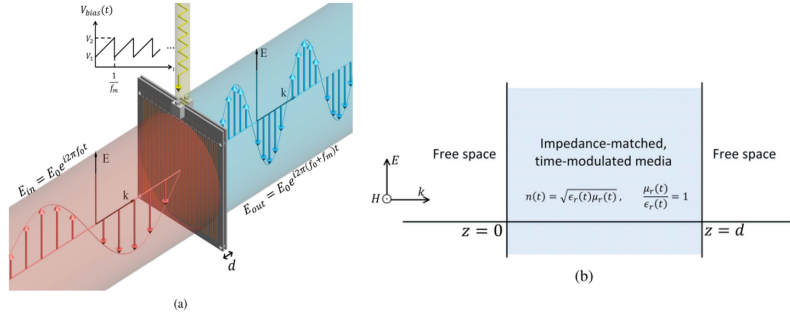


Figure 2.15: (a) Serrrodyne frequency translator based on a transparent metasurface. (b) A time-modulated analogous impedance-matched medium [17].

$$e_i(z = 0^-, t) = E_i e^{j2\pi k f_i t} \quad (2.19)$$

Assuming that

$$f_i \gg N_{max} f_m \quad (2.20)$$

where  $N_{max}$  is the number of harmonics used to accurately represent  $n(t)$ , it is observed that the frequency of the field present in the medium increases linearly with the propagation distance, varying by an amount equal to  $f_m$  every  $\lambda_i/2$ , where  $\lambda_i = \frac{c}{f_i}$  and the wavelength of the incident wave in vacuum. The behavior of the metasurface just discussed can be observed in Fig.2.16.

Assuming valid the hypotheses made previously, it can be deduced that the electric field inside the metasurface expressed as a function of time and space is

$$e(z, t) = E_i A(z, t) e^{j \left( 2\pi f_i t - \frac{2\pi f_i}{c} \sqrt{\epsilon_r(t)\mu_r(t)} z \right)} \quad (2.21)$$

where  $A(z, t)$  And a slowly variable function both in time and in space.

The field transmitted to the interface with the surface, for  $z = \frac{\lambda_i}{2}$ , takes the following form:

$$e \left( z = \frac{\lambda_i}{2}, t \right) = E_i A \left( z = \frac{\lambda_i}{2}, t \right) e^{j(2\pi f_i t - \pi n(t))} \quad (2.22)$$

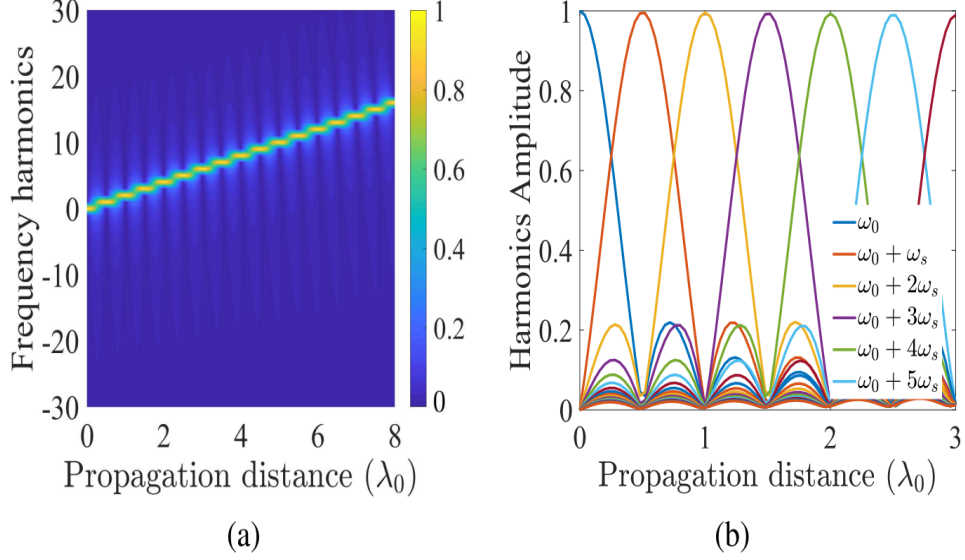


Figure 2.16: (a) Harmonic distribution as a function of propagation distance in a time-modulated medium. (b) Field amplitudes as a function of propagation distance for the first five harmonics [17].

From the equations (2.22) and (2.19), It is possible to obtain the transmission coefficient  $\tau(t)$  of the medium

$$\tau(t) = \frac{e(z = \frac{\lambda_i}{2}, t)}{E_i e^{j2\pi f_i t}} = A\left(z = \frac{\lambda_i}{2}, t\right) e^{-j\pi n(t)} \quad (2.23)$$

From the expression of  $\tau(t)$  it is possible to deduce that, for the metasurface to perform a translation in ideal frequency, resulting in an increase in frequency equal to  $f_m > 0$ , it should turn out that

$$\begin{cases} n(t) = \sum_{k=-\infty}^{+\infty} 2 - 2f_m(t - kT) \text{rect}\left(\frac{t - kT - \frac{T}{2}}{T}\right) \\ A(z = \frac{\lambda_1}{2}, t) = 1 \end{cases} \quad (2.24)$$

where  $T = \frac{1}{f_m}$ , rect is the rectangular pulse.

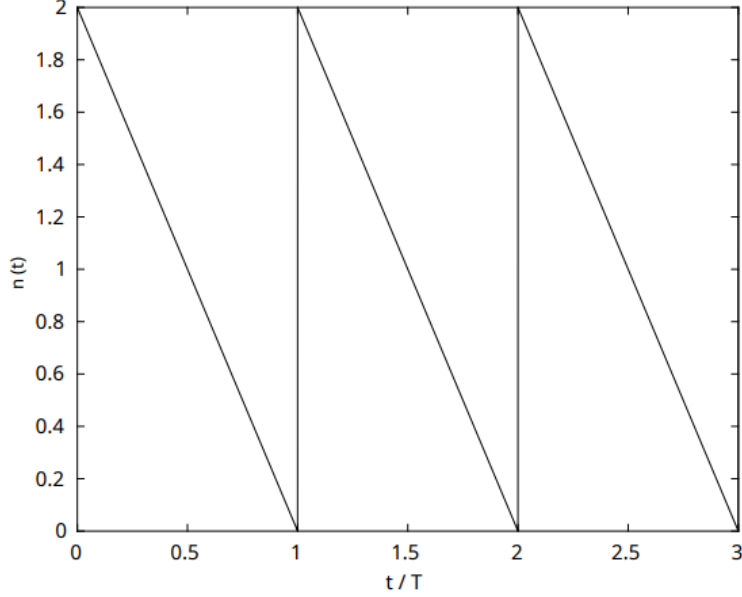


Figure 2.17: Time course of the refractive index  $n(t)$ .

Fig.2.17 shows the trend over time of the refractive index reported in (2.24). Substituting relations (2.24) in the equation (2.22) you get

$$e(z = \frac{\lambda_i}{2}, t) = E_i e^{j \left( 2\pi f_i t - \pi \sum_{k=-\infty}^{+\infty} 2 - 2f_m(t - kT) \text{rect} \left( \frac{t - kT - \frac{T}{2}}{T} \right) \right)} \quad (2.25)$$

By focusing on the exponent of the complex exponential in equation (2.25)

$$\begin{aligned} & j \left( 2\pi f_i t - \pi \sum_{k=-\infty}^{+\infty} 2 - 2f_m(t - kT) \text{rect} \left( \frac{t - kT - \frac{T}{2}}{T} \right) \right) = \\ & j \left( 2\pi f_i t - \sum_{k=-\infty}^{+\infty} 2\pi + (2k\pi - 2\pi f_m t) \text{rect} \left( \frac{t - kT - \frac{T}{2}}{T} \right) \right) = \\ & j \left( 2\pi f_i t - 2\pi + 2\pi f_m t - \sum_{k=-\infty}^{+\infty} 2k\pi \text{rect} \left( \frac{t - kT - \frac{T}{2}}{T} \right) \right) \end{aligned} \quad (2.26)$$

By deleting from the (2.26) the integer multiple terms of  $2\pi$  and substituting when obtained in (2.25) you get

$$e(z = \frac{\lambda_i}{2}, t) = E_i e^{j2\pi(f_i + f_m)t} \quad (2.27)$$

The equation (2.27) clearly shows how the transmitted field is a frequency shifted version of  $f_m$  of the incident field. The developed metasurface was tested for an incident wave at the frequency  $f_i= 10$  GHz and controlled with a fundamental frequency signal  $f_m = 1$  MHz. Fig.2.18 shows the spectrum of the transmitted electric field, in which it can be seen that there is a peak in  $f = f_i + f_m= 10.001$  GHz and that the conversion losses are equal to 5.3dB.

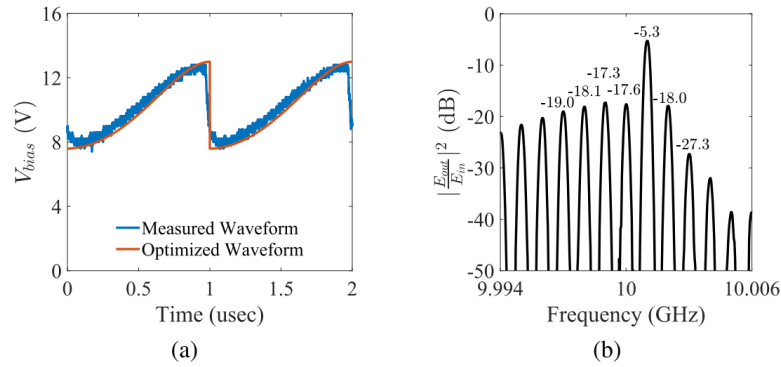


Figure 2.18: (a) A bias waveform is a waveform that is used to measure anything. (b) Transmission spectrum of a 10 GHz CW signal incident on the transmissive frequency translator as measured [17].

## 2.5 Space-time-coding digital metasurfaces

Based on the time modulation of the reflection coefficient, the author discuss space-time-coding digital metasurfaces in this study. In the frequency domain, a set of coding sequences is switched cyclically in a predetermined time period, resulting in the required harmonic scattered-power distributions. The method in [18] incorporates digital coding metasurfaces with “phase-switched screens” and “time-modulated arrays” to some extent. The underlying theory of time-varying coding metasurfaces based on the Fourier transform approach is first presented. Following that, the author give numerous illustrated instances to show how our approach can be used to manipulate spectral powers. The first example in Fig.2.19 involves designing space-time-coding sequences using a binary particle swarm optimization (BPSO) technique to achieve harmonic beam steering. The examples in the article focus on beam steering and shaping at the core frequency, whereas the remaining examples try to reduce scattering by spreading power over the frequency spectrum in a suitable manner. Finally, an  $8 \times 8$  space-time coding and programmable metasurface loaded with PIN diodes is built and tested experimen-

tally. The proposed method is projected to considerably expand the uses of digital coding metasurfaces, with significant benefits in scenarios such as wireless communication and radar systems.

As illustrated in Fig.2.19, a space-time-coding digital metasurface with a 2D array of  $M \times N$  components loaded with PIN diodes is considered. The reflection coefficient of an element can be dynamically adjusted with discrete phase or amplitude states by supplying a control voltage to a PIN diode. The reflection phase or amplitude of each coding element in the 1-bit scenario can be swapped periodically according to the digital “0/1” space-time-coding matrix in the bottom-right corner of Fig.2.19, where the red and green dots represent the “1” and “0” digits, respectively. The space-time-coding technique allows control of EM waves in both spatial propagation and harmonic power distribution at the same time [18].

We can adiabatically extend the approximate modeling that was originally introduced for space-coding metasurfaces by assuming a time-modulation speed substantially smaller than the EM-wave frequency and based on physical optics type approximations. As a result, the time domain far-field pattern scattered by the space-time-coding digital metasurface can be approximated as under normal incidence of plane waves with suppressed time-harmonic dependency  $\exp(j2\pi f_c t_c)$

$$f(\theta, \varphi, t) = \sum_{q=1}^N \sum_{p=1}^M E_{pq}(\theta, \varphi) \Gamma_{pq}(t) \exp\left\{j \frac{2\pi}{\lambda_c} [(p-1)d_x \sin \theta \cos \varphi + (q-1)d_y \sin \theta \sin \varphi]\right\} \quad (2.28)$$

where  $E_{pq}(\theta, \varphi)$  is the far-field pattern for the  $(p, q)$ th coding element computed at the central frequency  $f_c$ ,  $\theta$  and  $\varphi$  are the elevation and azimuth angles, respectively  $d_x$  and  $d_y$  are the element periods in the x and y directions, and  $\lambda_c$  is the central operating wavelength.  $\Gamma_{pq}(t)$  is the time-modulated reflection coefficient of the  $(p, q)$ th element, which is supposed to be a periodic function of time and defined over one period as a linear combination of shifted pulse functions, according to the timeswitched array theory [23] [24].

$$\Gamma_{pq}(t) = \sum_{n=1}^L \Gamma_{pq}^n U_{pq}^n(t) (0 < t < T_0) \quad (2.29)$$

where  $U_{pq}^n(t)$  is a periodic pulse function with modulation period  $T_0$ .

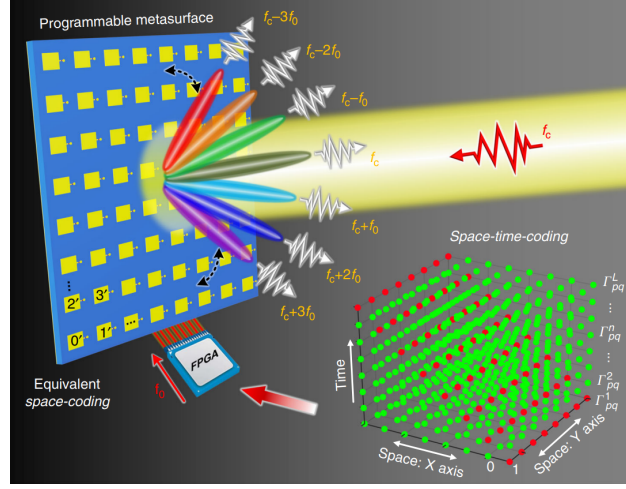


Figure 2.19: Illustration of a digital metasurface with space-time coding. By applying control voltages to PIN diodes, the metasurface element’s reflection coefficient can be dynamically modified with discrete phase or amplitude states. The reflection phase of each coding element in the shown example is periodically swapped according to the digital “0/1” space-time-coding matrix, which can result in similar multi-bit space-coding, such as “0”, “1”, “2” and “3” (equivalent 2-bit case). This coding approach allows for exact control of electromagnetic waves in both the spatial and frequency domains [18].

In each period, we have

$$U_{pq}^n(t) = f(z) = \begin{cases} 1, & (n-1)\tau \leq t \leq \tau \\ 0, & \text{otherwise} \end{cases} \quad (2.30)$$

where  $\tau = T_0/L$  denotes the pulse width of  $U_{pq}^n(t)$ ,  $L$  denotes the length of the time-coding sequence, and  $\Gamma_{pq}^n = A_{pq}^n \exp(j\phi_{pq}^n)$  denotes the reflection coefficient of the  $(p, q)$ th coding element during the interval  $(n-1)\tau \leq t \leq n\tau$  at the central frequency, with  $A_{pq}^n$  and  $\phi_{pq}^n$  denoting the amplitude and phase, respectively.

Finally at the  $m$ th harmonic frequency  $f_c + mf_0$ , the far-field scattering pattern of the space-time-coding digital metasurface is expressed as

$$a_{pq}^m = \sum_{n=1}^L \frac{\Gamma_{pq}^n}{L} \text{sinc}\left(\frac{\pi m}{L}\right) \exp\left[\frac{-j\pi m(2n-1)}{L}\right] \quad (2.31)$$

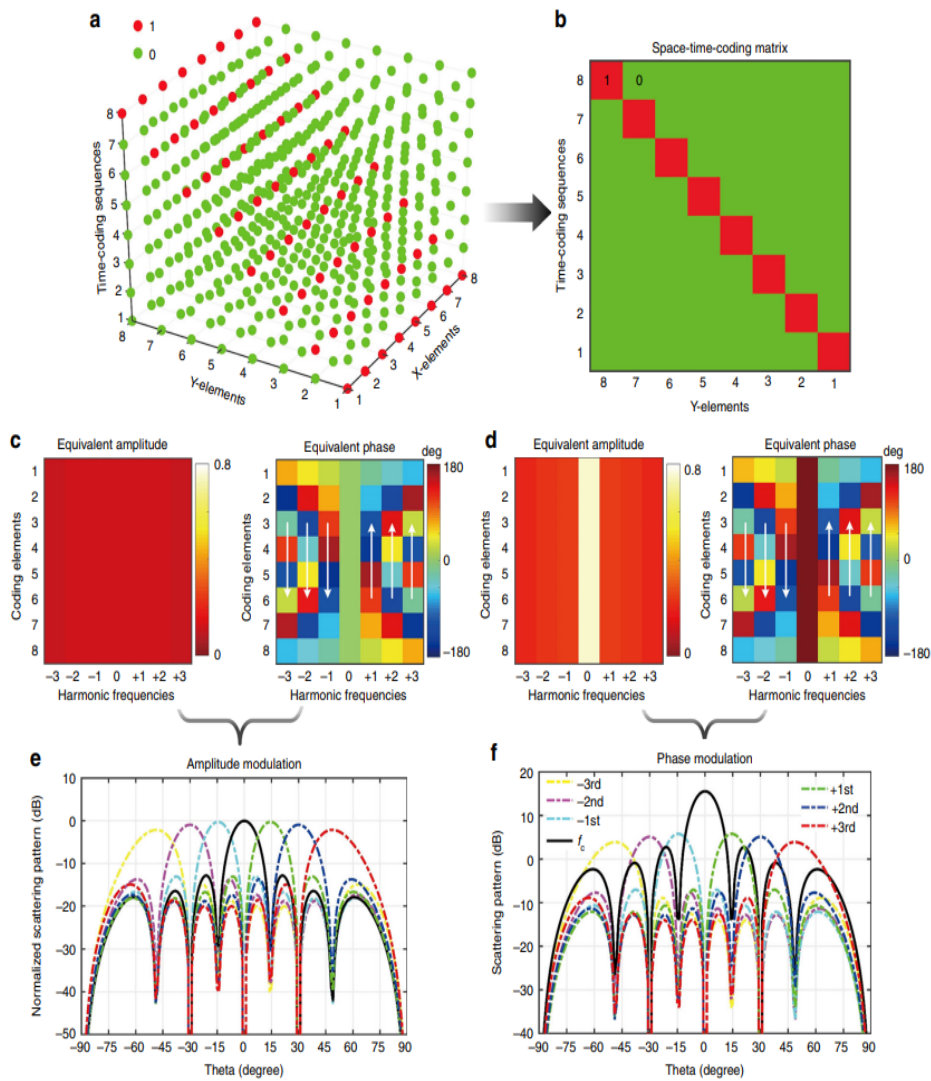


Figure 2.20: Harmonic beam steering. a, b The related 2D coding matrix and the 3D space-time-coding matrix. The red and green dots, respectively, represent the “1” and “0” digits. c, d AM and PM methods have equivalent amplitude and phase distributions, respectively. The phase gradients that emerge at the various harmonic frequencies are indicated by the white arrows. e, f Corresponding 1D scattering pattern cuts (at  $\phi = 90^\circ$ ) at different harmonic frequencies pertaining to AM and PM schemes, respectively [18].

$$F_m(\theta, \varphi) = \sum_{q=1}^N \sum_{p=1}^M E_{pq}(\theta, \varphi) \cdot \exp\left\{j \frac{2\pi}{\lambda_c} [(p-1)d_x \sin \theta \cos \varphi + (q-1)d_y \sin \theta \sin \varphi]\right\} a_{pq}^m \quad (2.32)$$

We may use (2.32) to compute the coding metasurface's scattering pattern at any harmonic frequency. We can synthesis the equivalent amplitude and phase excitations of all elements at a single harmonic frequency using Equation (2.31). Although the physical coding elements only have binary reflection phases ( $0^\circ$  or  $180^\circ$ ), the corresponding excitation [by Eq.(2.31)] can achieve nearly  $360^\circ$  phase coverage by properly structuring the time-coding sequences, which is a major aspect of the proposed technique. In this approach, a single 1-bit (or 2-bit) programmable metasurface that is regularly timeswitched can be used to synthesis multi-bit programmable metasurfaces, which can open up a slew of new possibilities. Traditional time-switched arrays have been studied in the past. As shown in Fig.2.20 a, b, time-gradient sequences can be used to achieve harmonic beam steering. By using AM only one element of the array scatters at a given time, thereby resulting in significant gain reductions. Conversely, if we use the same time sequences, but considering the proposed PM scheme instead, the scattered powers can be significantly enhanced. Fig.2.20 c, d illustrate the equivalent amplitudes and phases of the coding elements under AM and PM, respectively.

At positive and negative harmonic frequencies (see white arrows), some analogous phase gradients may also be seen, which are used to direct the harmonic beams. The harmonic beam steering can be better understood by introducing a time shift in the Fourier transform, Fig.2.20 shows the normalized scattering patterns pertaining to AM at different harmonic frequencies, while Fig.2.20 f shows the PM ones.

The author in [18] use a BPSO algorithm to optimize the time-coding sequence of each coding element for better power level equalization. As a result, as shown in Fig.2.21a, we obtain an optimal 2D space-time coding matrix. Fig.2.21b shows the equivalent harmonic scattering patterns, which indicate that the power levels at different harmonic frequencies are now uniform and around 7.6 dB greater than those for AM. Fig.2.21c and d show the 2D and 3D scattering patterns, respectively. The primary beams at different harmonic frequencies can be seen pointing in different directions, achieving the desired harmonic beam steering.

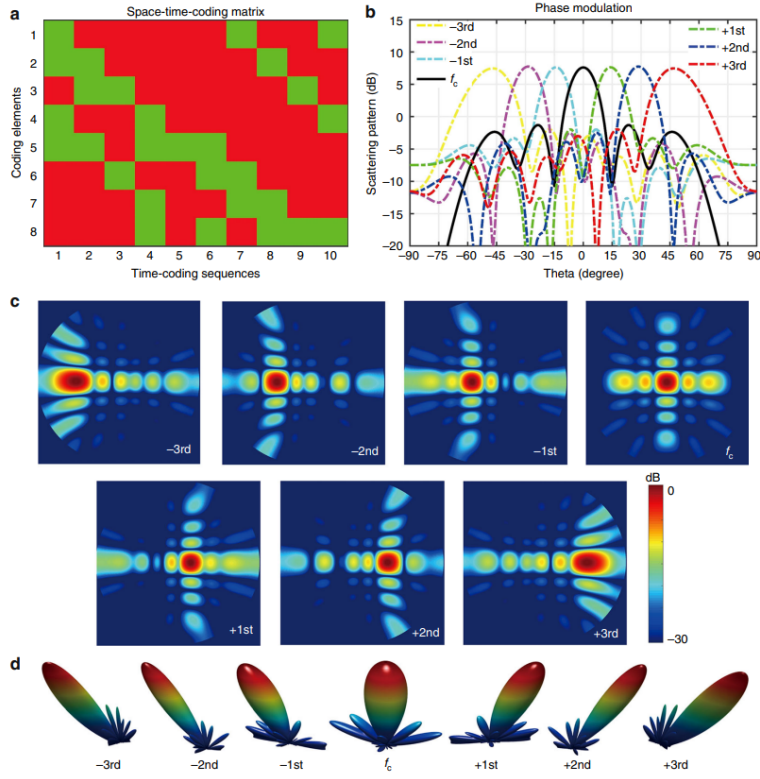


Figure 2.21: BPSO-optimized harmonic beam steering. a Optimized 2D space-time-coding matrix. b, c, d Corresponding 1D scattering-pattern cuts at  $\varphi = 90^\circ$ , 2D, and 3D scattering patterns, respectively, at different harmonic frequencies [18].

It is worth noting that the harmonic scattering patterns can also be estimated using the inverse fast Fourier transform (IFFT) technique, which can significantly lower the optimization's computing complexity, especially for electrically large metasurfaces. The space-time-coding strategy introduces a new method for designing multi-bit programmable metasurfaces (even with arbitrary phases) that does not necessitate a complex layout and control system and allows for more precise control of EM waves in the space and frequency domains using an 8x8 coding metasurface and time-coding sequences as shown in Fig.2.22.

Digital metasurfaces with space-time coding, in which each coding element contains a set of time-coding sequences that are switched cyclically during the modulation period. The suggested time modulation on digital coding, when combined with spatial modulation, can influence both the spatial (propagation direction) and spectral (frequency distribution) aspects of scattered EM power. The author developed beam-scanning patterns at multiple harmonic frequencies using

a BPSO-based time-coding sequence.

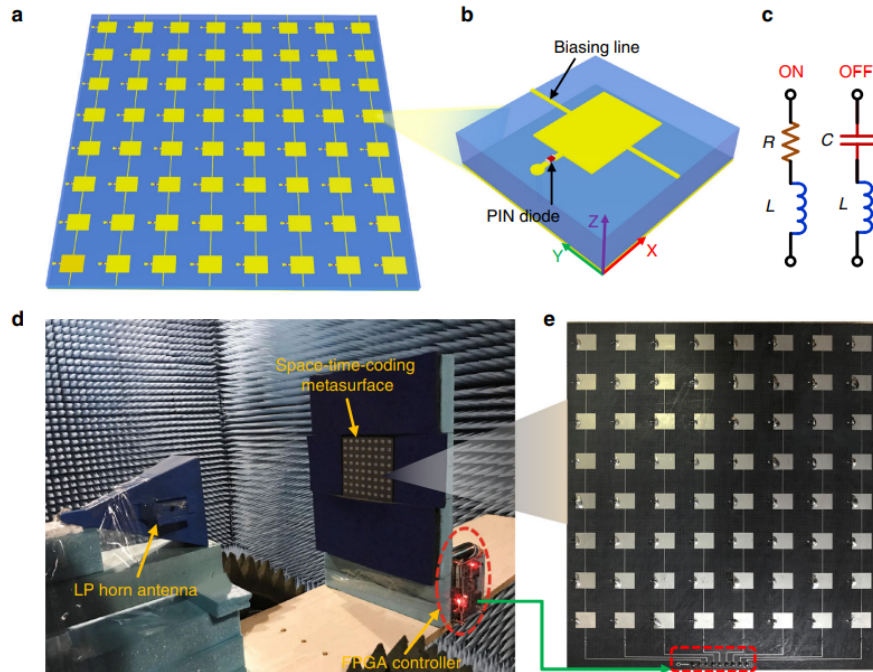


Figure 2.22: Prototype design, modeling, and characterization. a Schematic of the realized space-time-coding metasurface prototype. b Geometry of the coding element with the biasing line. c Equivalent circuit models of the PIN diode biased at the ‘ON’ and ‘OFF’ states. d Measurement setup in an anechoic chamber. e Photo of the fabricated prototype. f, g Numerically computed reflection phase and amplitude of the coding element, respectively, for both diode states as a function of frequency. The grey-shaded areas indicate a neighborhood of the operational frequency (10 GHz) [18].

## 2.6 Metaprism for Passive and non-reconfigurable metasurface

Channel estimation in RIS-assisted systems is still a work in progress, with three major challenges: (i) long training times, especially in multi-user MIMO systems, which may not be tolerable in dynamic scenarios; (ii) real-time reconfiguration of the RIS’s reflection functionality via a dedicated control channel with the BS; and (iii) the need for ad hoc channel estimation and signaling protocols, which make the introduction of RISs non-transparent. All of these concerns may make some

of the key predicted benefits of RISs, including as low cost, low complexity, and low energy usage, less desirable.

In this article “Using metaprisms for performance improvement in wireless communications.” [21] the author introduces the concept of metaprism, which is a fully passive, non-reconfigurable metasurface that works as a metamirror and has frequency-dependent reflecting qualities within the signal spectrum.

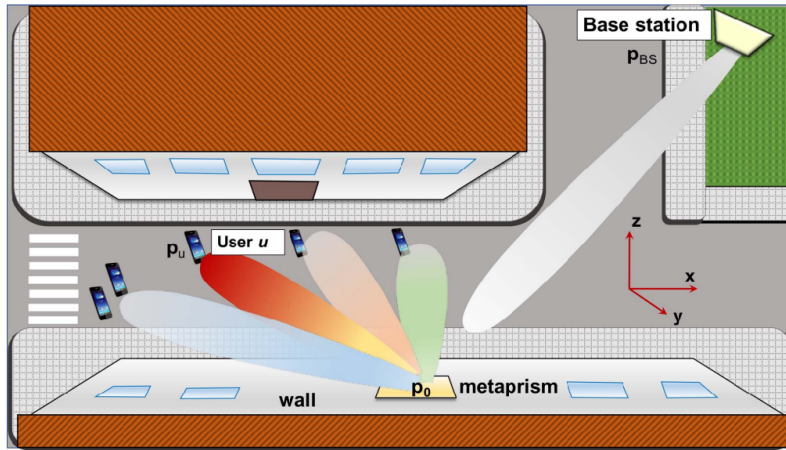


Figure 2.23: A metaprism empowers the analyzed NLOS scenario [21].

This is the first article proposing and analyzing how to exploit OFDM signals and frequency-selective reflecting metasurfaces with the purpose to improve the coverage of short-range wireless networks both in far-field and near-field channel conditions. A typical example of use-case scenario is shown in Fig. 2.23, where mobile users are in NLOS condition with respect to the BS and the metaprism is introduced to extend the covered area at a low-cost. Without interacting with the metaprism and without the need for dedicated CSI estimation schemes, which are the main current challenges and drawbacks of RISs as previously outlined, the proposed metaprism allows one to control the reflection of the signal through proper selection of the subcarrier assigned to each user using conventional OFDM signaling.

Figure 2.24 (top) shows a metasurface in the  $x - y$  plane with a center at coordinates  $p_0 = (0, 0, 0)$  and  $N \times M$  cells of size  $d_x \times d_y$  dispersed in a grid of points with coordinates  $p_{nm} = (0, 0, 0)$ . Figure 2.24 (bottom) shows a very general analogous model of the metasurface’s  $nm$ th cell at position  $p_{nm}$ , which consists of a radiation element (antenna) above a ground screen loaded with a cell-dependent and frequency-dependent impedance  $Z_{nm}(f)$ .

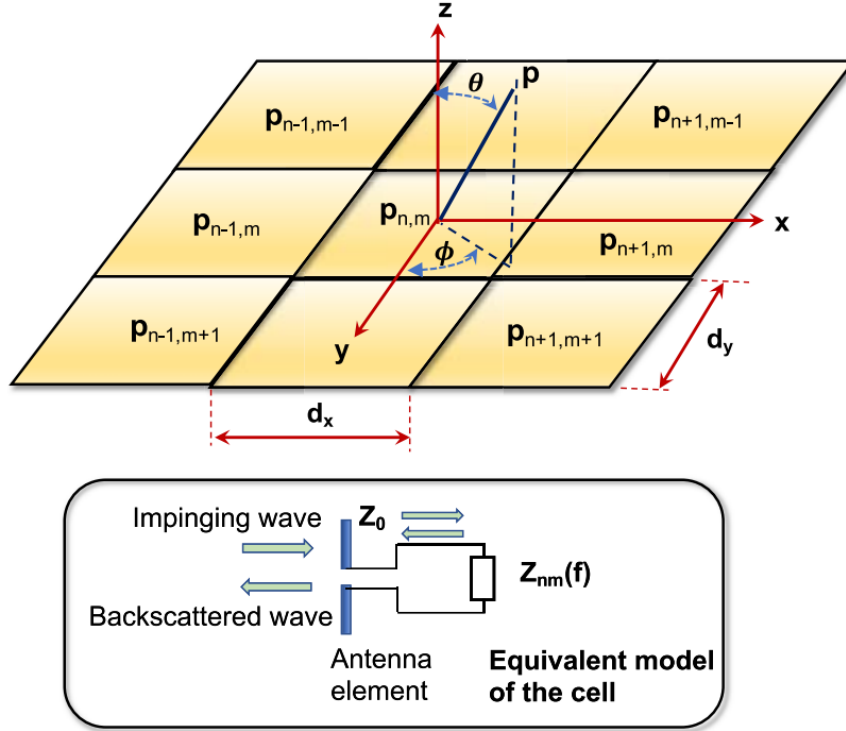


Figure 2.24: Metasurface composed of elementary cells (top). Equivalent model of the cell (bottom) [21].

## 2.7 Non-reciprocal and programmable meta-prism

In “Programmable nonreciprocal meta-prism” [19] a configurable metasurface is proposed that allows to obtain a controllable and non-reciprocal spatial decomposition, where each frequency component of the incident polychromatic wave is transmitted with a programmable transmission angle and gain through a DC voltage in the order of 3V. The metasurface consists of super cells which impose a certain phase variation on the incident wave  $\phi(f, x, y)$  and a certain gain  $T(f, x, y)$  which depend on their position on the surface and on the frequency of the incident wave. In general, the phase variation and the gain that the metasurface presents in one direction of propagation differ from those presented in the other. In order for his behavior to be non-reciprocal, it turns out that  $\phi^B(f, x, y) \neq \phi^F(f, x, y)eT^F(f, x, y) > 1 \gg T^B(f, x, y)$ , where  $B$  stands for “Backward” And  $F$  for “Forward”.

The metasurface is assumed to be illuminated by a electromagnetic polychro-

matic wave consisting of  $N$  frequency components, characterized by frequencies  $f_1, \dots, f_N$ , which propagates in the positive direction of the axis  $z$ , as shown in Fig.2.25 . The frequency components of the incident wave, interacting with the metasurface, take on different phase variations at different points  $(x, y)$ . The phase variation of the  $n^{th}$  frequency component is indicated with  $\phi_n(x, y)$ . Usually the phase and gain profile of the metasurface are designed in such a way that each frequency component is transmitted with a certain transmission angle and a certain gain.

In the event that the phase gradient is constant over the entire surface, the transmitted wave acquires an anomalous refraction, while, in the event that the phase gradient varies in space, greater functions are obtained such as beamforming and advanced applications of beam steering. Assuming that the metasurface has a constant phase gradient on its surface, it is possible to describe its behavior using generalized Snell's law.

$$\frac{\partial \phi_{x,n}}{\partial x} = k_n [\sin(\theta_x^{trns}) - \sin(\theta_x^{inc})] \quad (2.33)$$

$$\frac{\partial \phi_{y,n}}{\partial y} = k_n [\sin(\theta_y^{trns}) - \sin(\theta_y^{inc})] \quad (2.34)$$

where  $k_n$  is the wave number of the  $n$ th frequency component and  $\theta_a^{trns}$  and  $\theta_a^{inc}$  with  $a = x, y$  are respectively the angles of transmission and incidence in the direction  $a$ .

In general, for each frequency component, the acquired phase variation and gain are given by

$$\phi_n(r) = \sum_{m=1}^5 \phi_m(f_n, r) \quad (2.35)$$

$$T_n(r) = \sum_{m=1}^5 G_m(f_n, r) \quad (2.36)$$

Fig.2.26 shows the operating principle of the meta-prism, consisting of five distinct operations carried out by means of five different electronic and electromagnetic components. This scheme allows a high flexibility in the programmability of the meta-prism. The  $m - th$  stage of the scheme reported in Fig.2.26 is characterized  $\phi_m(f, r)$  and  $G_m(f, r)$ , where  $r$  is a vector that identifies a point on the surface.

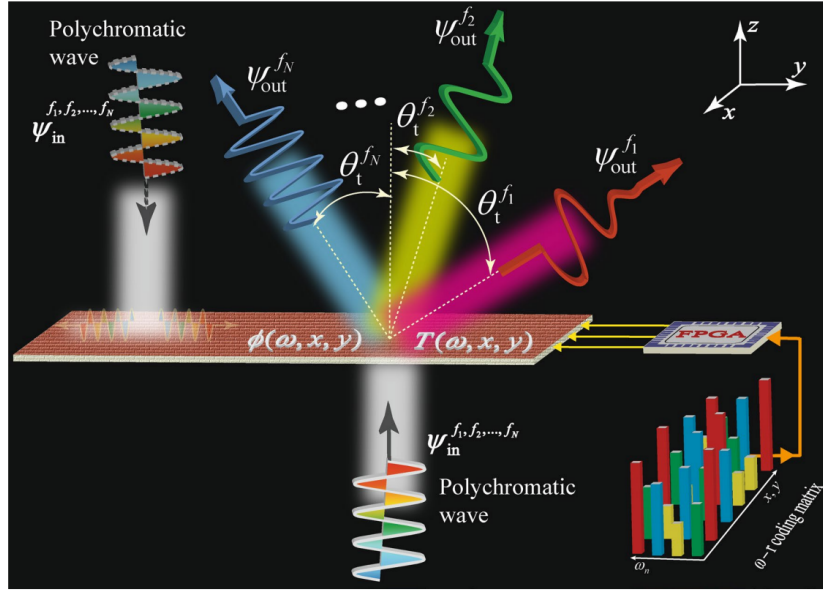


Figure 2.25: A digitally programmable nonreciprocal metasurface prism in concept [19].

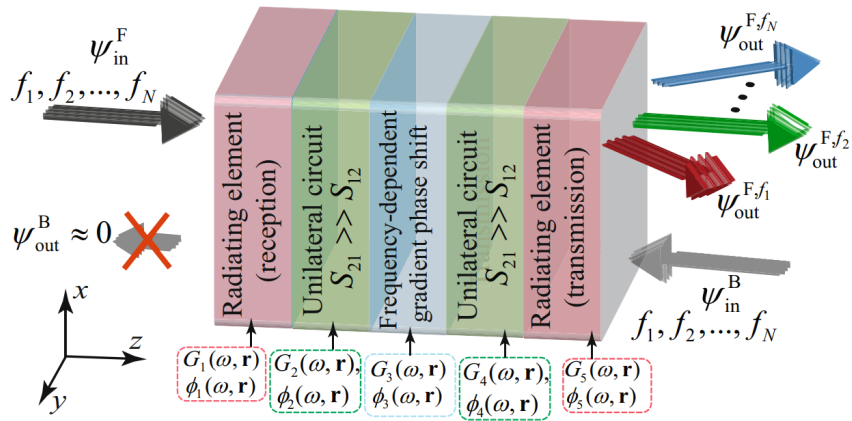


Figure 2.26: The nonreciprocal metasurface prism's programmable composition. The operation of the metasurface is guided by a four-step architecture, with each level demonstrating the necessary transmission phase and magnitude for controllable and programmable nonreciprocal prism functionality [19].

In the article, a meta-prism is created that operates for frequencies between 5.75 and 6 GHz. Experimentally it has been verified that signals at a frequency of

5.762 GHz are transmitted at an angle of  $-65.4^\circ$  and with a gain of 12 dB; 5.836 GHz signals are transmitted at an angle of  $-24.2^\circ$  and with a gain of 11.54 dB and that signals at 5.954 GHz are transmitted at an angle of  $25.1^\circ$  and with a gain of 10.4 dB.

## 2.8 Selective camouflage using time-controlled metasurfaces

In “Spread-spectrum selective camouflaging based on time-modulated metasurface” [20] a radar camouflage system is proposed which, by exploiting the electromagnetic properties of time-varying metasurfaces, makes it possible to make an object invisible to enemy radars and visible to friendly ones. The idea behind the camouflage system is that the metasurface, when illuminated by a signal  $e_i(t)$  produced by a radar, reflect a signal  $e_r(t)$  as close as possible to the background noise. This system is carried out by spreading the spectrum of the incident signal (spread spectrum) so that the reflected signal has an extremely low power spectral density [20].

The metasurface with which the object is covered is checked in a sequence  $m(t)$  and has a reflection coefficient  $\gamma(t, f)$ . Considering an incident electric field having the following form,

$$e_i(t) = a(t)e^{j2\pi f_i t} \quad (2.37)$$

where  $a(t)$  is a narrow-band function of time, and assuming that the metasurface has a constant reflection coefficient in the  $e_i(t)$ , then the reflected signal will have the following form

$$e_r(t) = e_i(t)\gamma(t) = a(t)e^{j2\pi f_i t}\gamma(t) \quad (2.38)$$

By Fourier transforming the equation (2.38) one gets

$$E_r(f) = A(f) \otimes \Gamma(f - f_i) \quad (2.39)$$

where  $A(f)$  and  $\Gamma(f)$  are respectively the Fourier transforms of  $a(t)$  and  $\gamma(t)$  and  $\otimes$  represents the product of convolution.

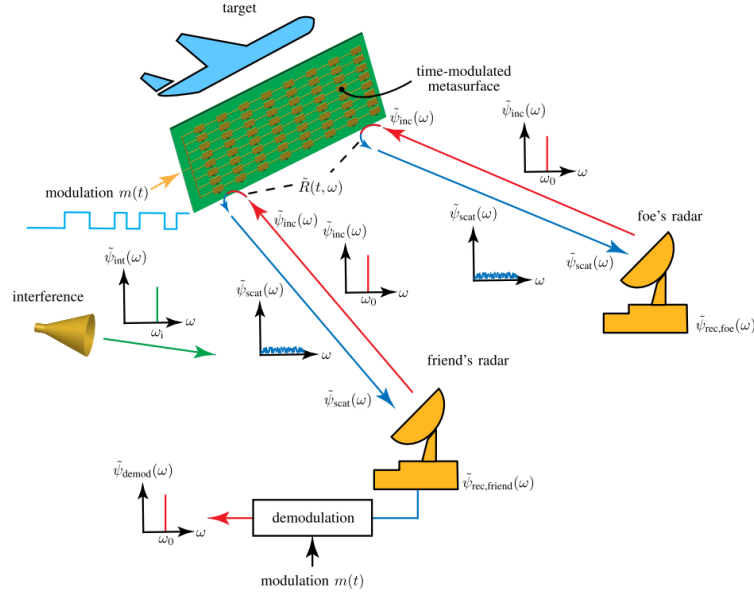


Figure 2.27: Spread-spectrum time-modulated metasurface camouflaging is proposed [20].

Designing  $\gamma(t)$  so that the band  $B_\gamma$  of its spectrum  $\Gamma(f)$  is much larger than the band  $B$  of the useful signal spectrum  $A(f)$ , the convolution operation in (2.39) produces a signal whose spectrum has a band approximately equal to  $B_\gamma$  (spread spectrum). This makes it  $e_r(t)$  difficult to intercept compared to  $e_i(t)$ . This camouflage technique also makes it possible to make the object identifiable by a friendly radar that knows the trend over time of the reflection coefficient. Assuming there is synchronization between  $\gamma(t)$  and the reflected signal  $e_r(t)$  it proves that

$$e_{demod}(t) = e_r(t) \frac{1}{\gamma(t)} = e_i(t) \quad (2.40)$$

The metasurface is controlled so as to quickly pass between the state of perfect magnetic conductor and that of perfect electrical conductor, presenting a reflection coefficient  $\gamma(t)$  which varies between  $+1$  and  $-1$ . Each state of the metasurface lasts for a time  $T_m$ . In order for the metasurface to be studied as an LTI system, the following relationship must hold

$$T_m \gg T_d > T_i \quad (2.41)$$

where  $T_d$  and  $T_i$  are the time constant of the metasurface and the period of the incident electromagnetic wave, respectively.

An ideal control sequence would be an infinite band white noise, since, assuming both finite energy, it would allow to obtain a zero power spectral density for each frequency, achieving perfect camouflage.

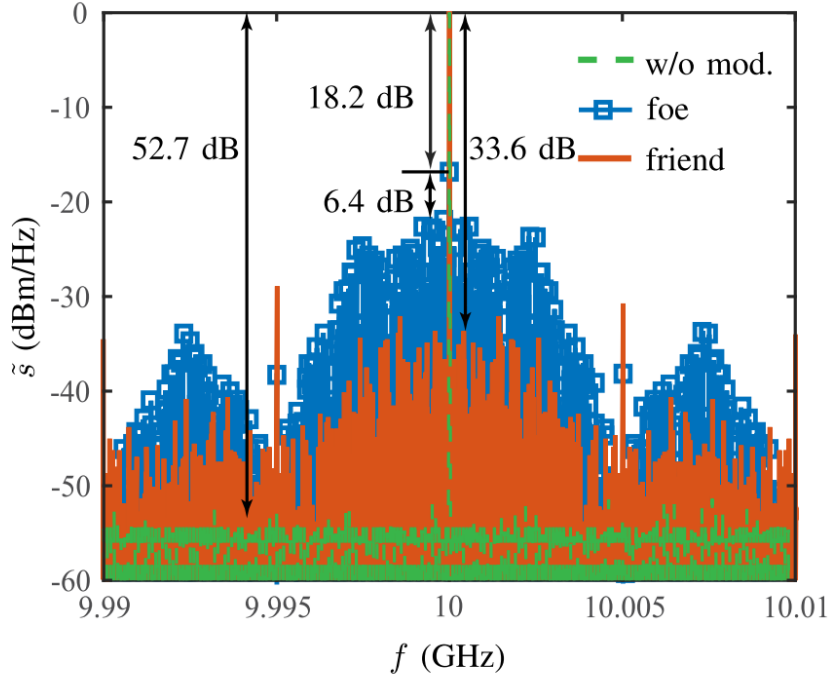


Figure 2.28: Camouflaging selectivity [20].

In practice, the control sequence band is limited by the speed of the PIN diodes used to make the metasurface: a control sequence is therefore used  $m(t)$  periodic and pseudo-random, which varies between  $+1$  and  $-1$  with a frequency  $f_m = 1/T_m$

Fig.2.28 shows the experimental results obtained by illuminating the previously discussed metasurface with an incident wave at frequency 10 GHz and using a pseudo-random control sequence characterized by  $f_m = 5$  MHz and period equal to  $127T_m$ . From the Fig.2.28 it is possible to deduce how the reflected signal picked up by the enemy radar, indicated in blue, is “scattered” on a 10 MHz. The spectral power density of the signal obtained from the friendly radar that knows the control sequence is represented in orange  $m(t)$ . Comparing the two results it can be seen that at the frequency of 10 GHz there is a difference of 18.2 dB between the power spectral density of the friend radar demodulated signal and that of the signal picked up by the enemy radar, confirming the ability of the

metasurface to selectively camouflage the object it covers.

## 2.9 Secure Electromagnetic Buildings using Slow Phase-Switching FSS

In “Secure electromagnetic buildings using slow phase-switching frequency selective surfaces” [22] the use of Frequency Selective Surface (FSS) is proposed to prevent communications to the outside or inside of a building, making it a Secure Electromagnetic Building (SEB). Fig.2.29 shows a cross section of a secure electromagnetic building (SEB). FSS are a class of metasurfaces that, formed by dielectric and metallic elements that are repeated periodically on the surface, exhibit frequency-dependent transmission and reflection properties.

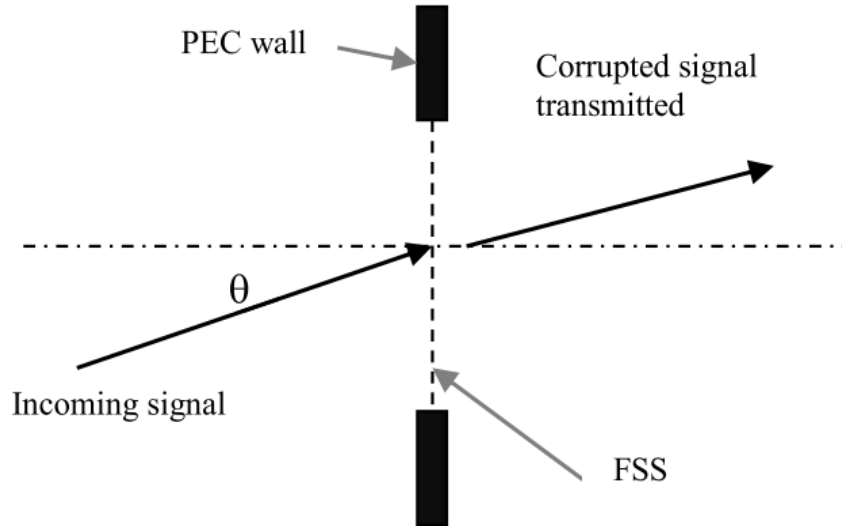


Figure 2.29: Camouflaging selectivity [22].

The transmission coefficient  $\tau(t)$  will only be a function of time if the surface is significantly bigger than the wavelength of the plane wave that ordinarily affects it. It is feasible to develop the latter in a Fourier series by managing the metasurface in such a way that it obtains a periodic trend of  $\tau(t)$ .

$$\tau(t) = \sum_{n=-\infty}^{+\infty} c_n e^{j2\pi n f_m t} \quad (2.42)$$

where  $c_n$  is the  $n^{\text{th}}$  coefficient of the Fourier series expansion and  $f_m$  and the fundamental frequency of the signal  $\tau(t)$ .

The Fourier transform  $T(f)$  of the equation (2.42) will be

$$T(f) = \sum_{n=-\infty}^{+\infty} c_n \delta(f - nf_m) \quad (2.43)$$

Recalling that the transmission coefficient coincides with the ratio between the transmitted field and the incident field, it is immediate to deduce that, in the frequency domain, the spectrum of the transmitted field will be given by the convolution between that of the transmission coefficient and that of the incident field, so as reported in the equation (2.44)

$$E_t(f) = T(f) \otimes E_i(f) = \sum_{n=-\infty}^{+\infty} c_n E_i(f - nf_m) \quad (2.44)$$

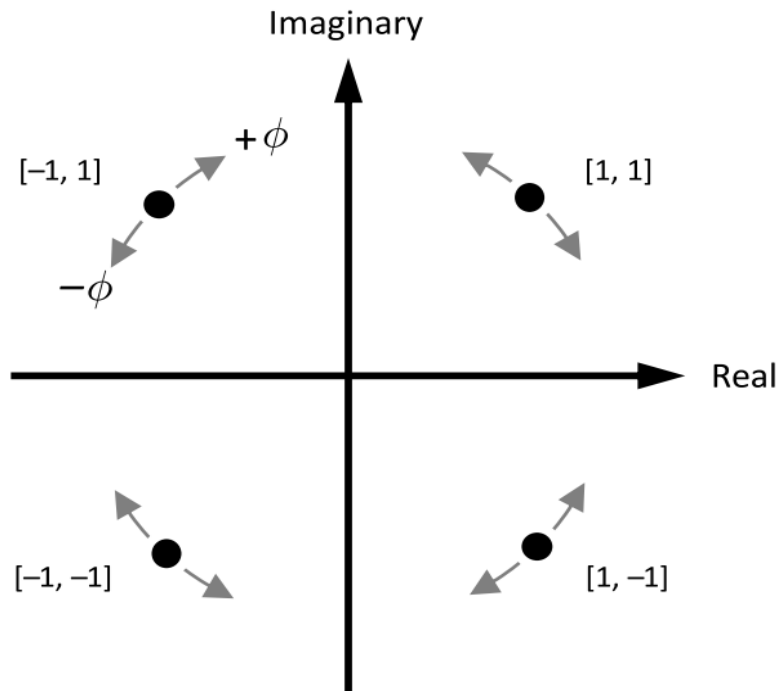


Figure 2.30: A QPSK system's constellation diagram exhibiting phase shifting [22].

An incident signal is considered modulated according to a modulation scheme QPSK. The metasurface is controlled in such a way that it has a phase transmission coefficient that varies between  $\pm\varphi$  in a period equal to the symbol time of the QPSK signal. The larger the phase is in absolute value, the higher the probability that, in the constellation diagram, a symbol passes into the adjacent quadrant, increasing the probability of error (bit error rate (BER)). Fig.2.30 shows, by way of example, the constellation diagram of a QPSK system and the effect caused by the phase variation of the transmission coefficient of the metasurface.

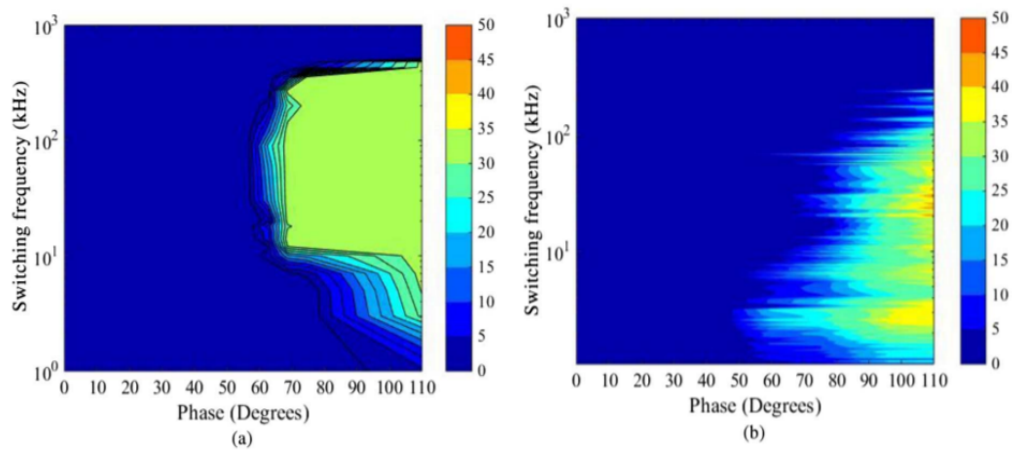


Figure 2.31: BER (%) of GSM signal transmitted through the reconfigurable FSS using (a) measured and (b) simulated data [22].

In order to verify what was theoretically obtained, an FSS was created which has varactor diodes in its structure that can be controlled in voltage with a signal that varies between 20 and 23 Volts, allowing to obtain an almost linear phase variation equal to  $110^\circ$ . Considering a GSM signal characterized by a 2 GHz frequency carrier and a bit rate of 270.833 Kbits/s and using a square wave with frequency as control signal  $f_m$  (switching frequency), it is possible to obtain BER's between 0% And 36%. Fig.2.31a shows a plot of the measured BER in percentage versus switching frequency and FSS phase difference. For comparison, system simulations were carried out using the measured FSS characteristics as illustrated in Fig. 2.31b.

# Chapter 3

## Metasurfaces working beyond millimeter waves

Although time-varying metasurfaces provide novel techniques to govern light-matter interactions, realizing time-varying metasurfaces, particularly at optical frequencies, is difficult. The phase must be changed exceedingly quickly in order to provide a discernible wavelength/frequency shift at optical frequencies. This section explains how to process signal at tera hertz frequencies using several approaches.

### 3.1 Time-Varying Metasurfaces Based on Graphene Microribbon Arrays

The author in this article [25] proposes a time-varying metasurface based on graphene microribbons that may be used to adjust the wavelength of reflected waves at terahertz frequencies.

The optical conductivity of graphene, and hence its complicated refractive coefficients, can be dynamically adjusted by changing its Fermi level by an applied electrostatic potential. A graphene microribbon metasurface has been proven to reflect terahertz electromagnetic waves with either increased or decreased frequency as compared to the incident waves by altering the Fermi level of graphene with a certain temporal modulation frequency.

Graphene is a two-dimensional conductive film with optical conductivity

$$\sigma(\omega) = \frac{e^2 E_F}{\pi \hbar^2} \frac{i}{\omega + i\tau^{-1}} \quad (3.1)$$

where  $\omega = -\frac{\partial\phi}{\partial t}$ ,  $\tau$  is relaxation time,  $\hbar$  is the reduced Planck's constant.

Graphene's optical conductivity, and hence its complicated refractive indices, are greatly influenced by the Fermi level,  $E_F$ . However, due to weak wavematter interactions caused by the monolayer thickness of a continuous graphene membrane, achieving a big enough phase transition is difficult. The author proposes using graphene microribbon arrays instead of a continuous graphene screen to improve wavematter interactions, which result in bigger phase changes due to resonant behavior at particular frequencies.

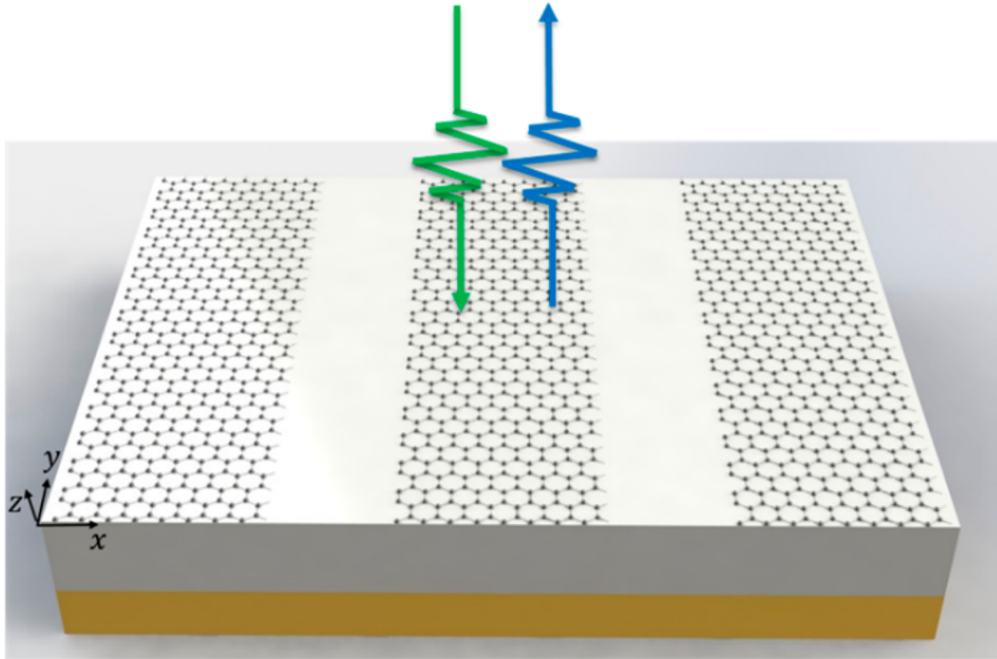


Figure 3.1: The graphene microribbon array is depicted schematically on top of a  $10 \mu\text{m}$  thick dielectric spacer and a metallic mirror in this diagram. The frequency shift of the wave upon reflection is represented by arrows of various colors [25].

Figure 3.1 shows the time-varying metasurface design, which includes graphene microribbon arrays on top of a transparent spacer layer and a thick metal substrate. The ribbon width and periodicity of graphene microribbon arrays are set to  $25$  and  $50 \mu\text{m}$  meters, respectively. These structural parameters are the result of several electromagnetic simulations optimizing the graphene microribbon arrays so that a large-enough phase change may be accomplished for different Fermi levels of graphene around the wavelength of  $300 \mu\text{m}$  (about  $f = 1 \text{ THz}$ ). The dielectric spacer's (polyimide) refractive index is fixed to a constant value of  $n = 1.7$ . To improve overall performance, the dielectric layer thickness is chosen to be  $10 \mu\text{m}$ . The metal on the back side is thought to be a perfect electric conductor (PEC),

reflecting waves back into the dielectric spacer. Because of the metasurface's time-varying phase change, the reflected waves will change frequency.

Figure 3.2a shows the calculated reflection spectra of graphene microribbon arrays for three distinct  $E_F$  values. There is a resonant behavior due to a localized electromagnetic response from microstructured graphene for  $E_F = 0.3$  eV, with a drop in the reflection spectra approximately  $300 \mu\text{m}$ .

When  $E_F$  is increased from 0.3 eV to 0.9 eV, the resonance wavelength shifts toward shorter wavelengths. Figure 3.2b depicts the  $E_z$  electric field distribution from the side for one ribbon with a wavelength of  $300 \mu\text{m}$  and an  $E_F$  of 0.6 eV. Figure 3.2b clearly shows localized resonant dipoles along the borders of the ribbon.

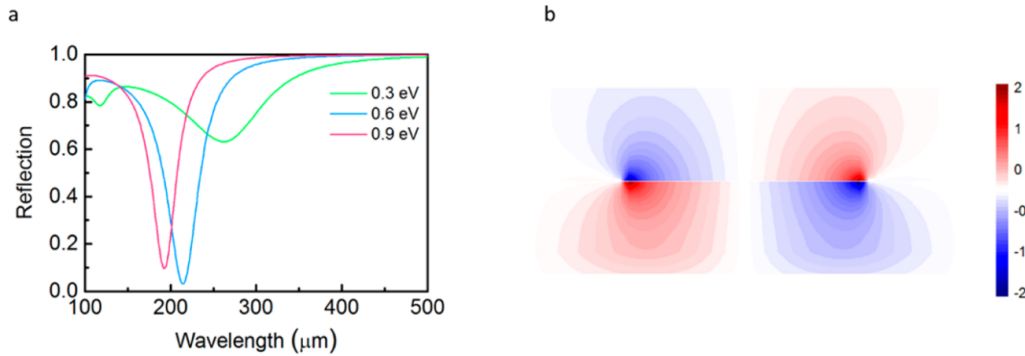


Figure 3.2: (a) Calculated graphene microribbon array metasurface reflection spectra for three distinct graphene Fermi energies. (b) A single graphene microribbon unit cell's simulated electric field distribution ( $E_z$ ) [25].

The metasurface should be operated at frequencies where the largest phase change occurs in order to generate the greatest rise in the frequency of terahertz waves. A preferable technique is to divert the operation frequency from the resonance frequency by a little amount so that there is still a moderate phase change with adequate reflection from the graphene metasurface. Changing the Fermi level, and thus the complex refractive indices, of graphene as a function of time can provide a time-varying metasurface that allows for a frequency change in reflected terahertz waves.

The author shows a temporal modulation pattern for modifying the Fermi level of graphene in Figure 3.3a, which use a simple analytical formula to comprehend the operating principle and crucial factors such as frequency change. The overall phase change for Fermi levels changing from 0.1 eV to 1 eV is determined to be  $\phi \approx 5$  when terahertz waves with a wavelength of  $200 \mu\text{m}$  ( $f = 1.5$  THz) are impinge on the graphene metasurface.

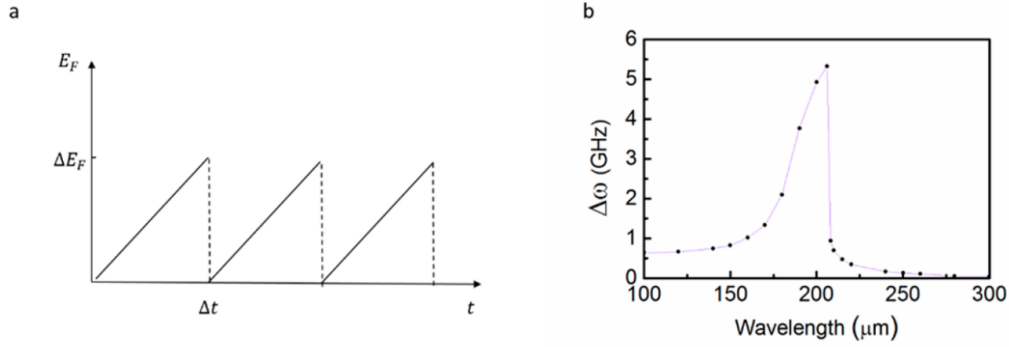


Figure 3.3: (a) A temporal modulation strategy for modifying graphene Fermi levels has been proposed. (b) For varied operation wavelengths of a time-varying metasurface, calculated frequency change of reflected terahertz waves [25].

Suppose Fermi levels are modulated by  $\Delta t \approx 10^{-9} s$ , which necessitates the use of a 1 GHz alternate current (ac) on graphene (Figure 3.3a). The frequency change in this case is  $\omega \approx -\frac{\Delta\phi}{\Delta t} = 5 GHz$ , with a quality factor of  $\frac{\Delta\omega}{\omega} = 0.021$ . For actual applications, author chooses a moderate temporal modulation frequency. Nevertheless, faster modulation speeds that may be attained in the future will result in larger frequency shifts, because frequency change is proportional to modulation frequency.

Low metasurface reflection is one of the major disadvantages of operating at resonance frequencies. For a Fermi level of 0.6 eV (Figure 3.2a), where the highest phase jump occurs, reflection is nearly zero for this wavelength of 200  $\mu m$ . As a result, a different scenario exists in which the operation frequency is chosen to be different from the resonance frequency, resulting in a lower phase change but greater reflection performance.

The frequency change is projected to be smaller as a result of the smaller phase change. It is worth noting, however, that even such a frequency change is fascinating, and is difficult to do with ordinary optical equipment. The frequency change of the reflected wave is an important parameter, and the author chooses it to be a figure of merit to compare the performance of graphene-based time-varying metasurfaces for different operation wavelengths.

The graphene microribbon arrays can operate in a variety of frequency ranges and achieve a variety of optical performance goals. When compared to space-varying metasurfaces, time-varying metasurfaces provide a more active means of controlling light. More sophisticated devices, such as multifunctional anomalous deflectors and optical isolators, can be built by combining both space-gradient patterns and temporal modulation at the same time.

## 3.2 Linear Frequency Conversion via Sudden Merging of Resonances

Frequency conversion of light is normally accomplished by nonlinear optical phenomena, but it can also occur when light propagates across a linear medium with time-varying optical properties. The frequency of electromagnetic waves traveling through timevariant media changes due to the momentum conservation, according to Morgenthaler [26]. Extreme optical properties can be achieved in metamaterials, and these qualities can be dynamically controlled. As a result, time-varying metamaterials can be a great platform for custom frequency converters that use the linear frequency conversion method [27]. The frequency conversion of THz waves on a suddenly shifting metasurface, or 2-dimensional metamaterial, is demonstrated experimentally. The metasurface has two different resonances, which are combined into one when an optical pulse illuminates it. THz frequency conversion from the original resonance frequencies to the combined resonance frequency occurs when the THz wave travels over the metasurface during this merging phase.

The momentum conservation phenomenon gave rise to the conversion phenomenon. The response function of the original metasurface,  $\theta_1(t)$  is changed to the response function of the combined metasurface,  $\theta_2(t)$  after the pumping. The charge momentum, which is the surface current on the metasurface, must, nevertheless, be continuous. The author calculates the surface current density function  $J(t)$  on the metasurface as a function of these conditions.

$$J(t) = \int_{-\infty}^{+\infty} [\theta_2(t - \tau)E_v(\tau) + \theta_2(t - \tau)u(\tau - t_d)[E_i(\tau) - E_v(\tau)]]d\tau \quad (3.2)$$

where  $E_{i,v}(\tau)$  signifies the input field and virtual field which is defined to satisfy  $\int_{-\infty}^{+\infty} \theta_2(t - \tau)E_v(\tau)d\tau = \int_{-\infty}^{+\infty} \theta_2(t - \tau)E_i(\tau)d\tau$  in equation 3.2 and calculate the converted field from the input field.

The experiments and findings are depicted in Figure 3.4. As illustrated in Fig.3.4a, the suggested metasurface is made up of an array of two metal split ring resonators (SRRs) on a semi-insulating GaAs substrate. The unit cell's outer and inner SRRs are planned to exhibit resonances at  $\omega_1 = 2\pi \times 0.62$  THz and  $\omega_2 = 2\pi \times 1.24$  THz. Fig.3.4(b-d) shows transmission spectra in the range of  $-4.4ps \leq t_d \leq 15.6ps$  at few selected time delays (-4ps, 2ps, and 15ps) and amplitude transmission at the combined resonance frequency as a function of  $t_d$ , respectively.

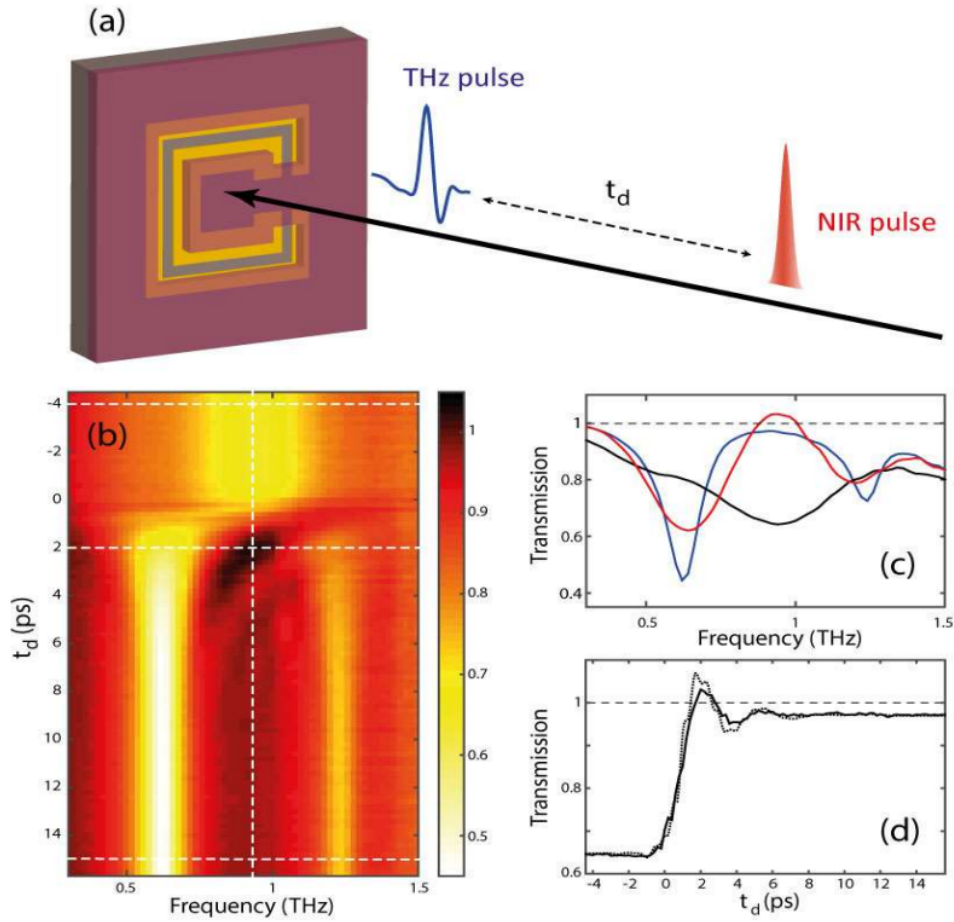


Figure 3.4: (a) The experiment is depicted schematically. (b) Metasurface amplitude transmission as a function of time delay (y axis) and frequency (x axis). (c) Amplitude transmission with different time delays: -4 ps (black), 2 ps (red), and 15 ps (blue). (d) Amplitude transmission as a function of time delay at 0.92 THz. The theoretical computation is indicated by the dot line [27].

To spatially limit optical carrier injection for undesirable areas, a dielectric multilayer is formed and patterned over the SRR. When the metasurface is illuminated, the ultrafast optical pump pulse at 800 nm produces photo-carriers in the gap between the two SRRs. At optical pumping of  $10\mu J/cm^2$ , the area with increased photoconductivity develops a new current route, and the two SRRs are effectively merged into one single SRR oscillating at the 'merged' resonance frequency,  $\omega_{mer} = 2\pi \times 0.92$  THz. With a broadband sub-cycle THz input field and a  $10\mu J/cm^2$  optical pump beam, the author examined the transmission spectra of the metasurface as a function of time delay  $t_d$ .

The theoretical computation is indicated by the dot line in Fig.3.4(d). The measured transmission spectra consistently show the original two modes in the range of  $t_d > 10ps$  range and the combined mode in the range  $t_d < 0ps$ . On the other hand, transmission at 0.92 THz about  $t_d = 2 ps$  is observed as more than unity as a result of the frequency conversion.

The frequency conversion observed is completely independent of nonlinear optical processes. The postulated phenomena are not based on nonlinear susceptibilities of composing materials, and even for very weak intensity input waves, conversion efficiency is not affected. Frequency conversion in nonlinear materials or nonlinear metamaterials is clearly distinguishable from this point. Because powerful sources for nonlinear processes need high implementation cost in this frequency range, frequency conversion via time variable metasurface may be extremely valuable in THz science or application.

### **3.3 Electrical control of terahertz frequency conversion**

Nonlinear frequency conversion, particularly in the THz frequency range, is still in its infancy due to the scarcity of powerful THz sources and nonlinear media. Instead of exploiting material nonlinearities, linear frequency conversion using time-varying media has been offered as an alternative. In the THz spectral range, this type of frequency conversion provides a constant conversion efficiency regardless of input power, and thus has the potential to achieve comparable or even higher conversion efficiencies than nonlinearity-based frequency conversion methods. The key to this frequency conversion process is a rapid change in surface conductivity, and managing the pace of such change can be utilized to regulate the frequency conversion process.

Optical pumping (OPTP) rapidly modifies the effective surface conductivities in the absence of external voltage. The conductivity change in the region under the direct-current (DC) electric field is delayed by later processes of inter-valley scattering and Coulomb screening when an external voltage is supplied to the samples. The frequency conversion process can be regulated by electrically controlling the rate of change in the surface conductivities.

In this article [34] the metasurface structure was made in the same way as the IPCA, but the electrodes were designed to produce split-ring resonators (SRR), as shown in Fig.3.5(a) (schematic illustration) and Fig.3.5(b) (photo illustration) (microscopic image).

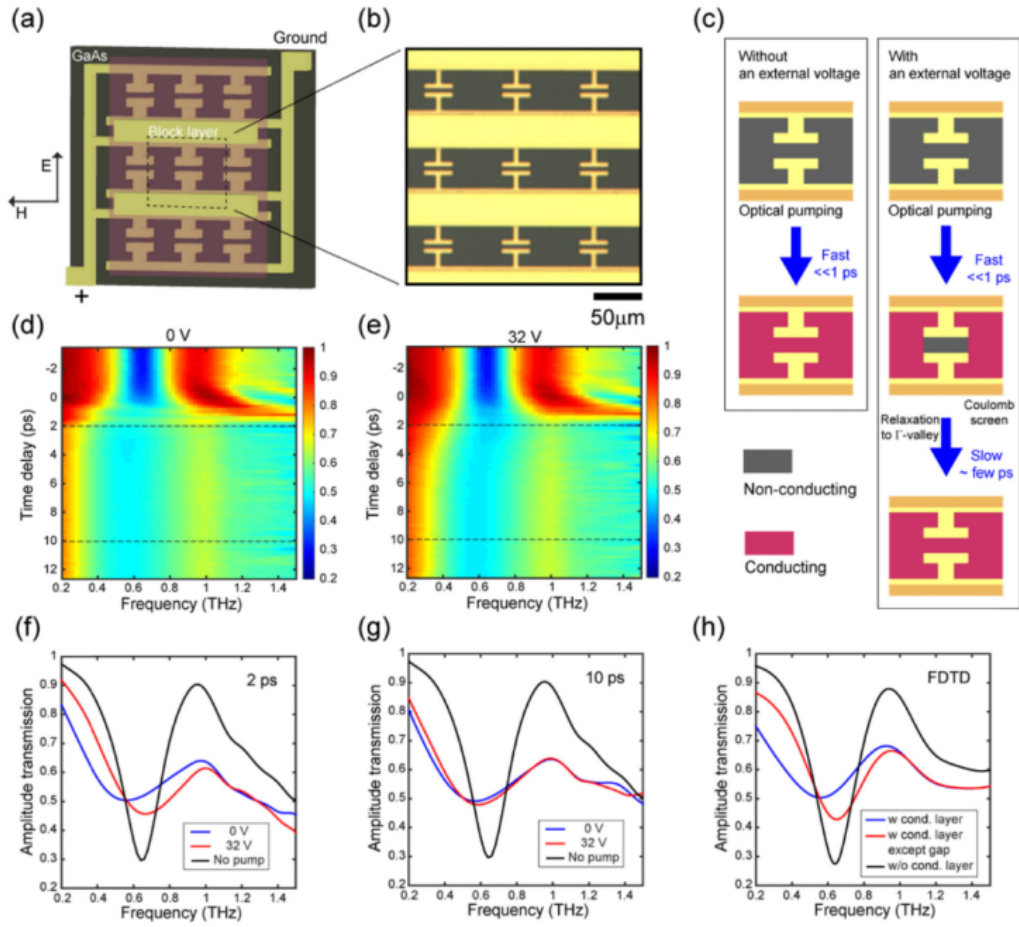


Figure 3.5: (a) Illustration of a schematic and (b) a microscopic photograph of a metasurface. The polarization of the input THz wave is indicated by the arrows in (a). (c) Schematic illustration of metasurface temporal conductivity change with and without external voltage. (d) Transmission spectra measured through metasurface without external voltage as a function of time delay,  $t_d$ , and (e) transmission spectra obtained with 32 V external voltage (f) Selected transmission spectra with (red) and without voltage at  $t_d = 2$  ps (blue). The transmission spectrum through the metasurface without optical pumping is shown in black. (g) Transmission spectra with and without voltage at  $t_d = 10$  ps. (h) Numerical simulation of transmission spectra via a metasurface with a conducting layer for the full exposed region (blue), a conducting layer except for the gap (red), and no conducting layer (black) [34].

The time-varying behavior of the metasurface is dispersed as a result of the electrical modulation of the spatiotemporal conductivity distribution. OPTP mea-

measurements were used to explore the metasurface's time-varying behavior and electrical modulation, as illustrated in Figs.3.5(d)-3.5(f)(g). The metasurface initially exhibits profound resonance at 0.6 THz due to the SRR structures. The resonance is suddenly slowed and red-shifted by optical pumping in the absence of external voltage, and the dulled resonance is maintained for more than ten picoseconds, as illustrated in Fig.3.5(d).

The transmission spectra of the metasurface with an external voltage of 32 V, on the other hand, show blue-shifted resonance shortly after optical pumping, as seen in Figs.3.5(e) and 3.5(f). The low conductivity of the gap region due to inter-valley scattering causes this form of resonance blue-shift. However, when the time delay increases, the blue-shifted resonance gradually lowers to a lower frequency, eventually resembling the resonance recorded without external voltage as illustrated in Fig.3.5(g). This resonance change is attributed to the gap region's conductivity recovering as a result of Coulomb screening.

In general, external voltage suppresses both up- and down-conversion processes. However, down-conversion components are suppressed more strongly than up-conversion components. Although the frequency conversion presented has a similar characteristic to the nonlinear spectrum broadening generated by self-phase modulation, the physical genesis of the frequency conversion process from time-varying surfaces is fundamentally different. The degree of frequency manipulation and the accompanying conversion efficiency are invariant to the input power since the media's temporal change is independent of the input wave. Furthermore, despite the thin film geometry's extremely short contact length, noticeable frequency manipulation is achievable because external control via optical pumping can dramatically alter the media's properties. Finally, because an abrupt change is the primary contributor to the frequency conversion process, the conversion can be controlled electrically by altering the speed of the conductivity change, as shown in this article [34].

### **3.4 Thermally switchable terahertz wavefront metasurface**

The material vanadium dioxide( $VO_2$ ) recently has attracted the attention of the THz community. In this article [28] two thermally switchable THz metasurface wavefront modulators, a THz multi-focus lens (TML), and a THz Airy beam generator (TAG) are presented. The metasurface devices are entirely made of microstructured  $VO_2$  thin films with no extraneous metal features. When the temperature rises above  $T_C$ , the  $VO_2$  material takes on metallic properties, and the device function is activated, in which the metasurfaces convert the input x-polarized THz

wave into a y-polarized wave with desired phase and amplitude modulations, and the y-polarized THz plane wave is focused into four focus points or a y-polarized THz Airy beam is generated. The devices are transparent to a good approximation in the off-state at temperatures below  $T_C$  and have no effect on the THz wavefront. As a result of the controlled tuning of the ambient temperature, the THz device function is dynamically regulated. Using a THz holographic imaging system, the characteristics of the two THz metasurface wavefront modulators were examined in the frequency range of 0.3 to 1.2 THz.

The overall concept for evaluating the operational properties of the developed metasurface devices on the THz wavefront is roughly represented in Fig.3.6. The metasurface device is in its off-state at  $20^\circ\text{C}$ , which is lower than the  $T_C$  of  $\text{VO}_2$ , and will not affect the THz wave, as shown in Fig.3.6(a). The device function will be turned on and the THz wavefront will be modified at  $70^\circ\text{C}$ , which is higher than the  $T_C$  of  $\text{VO}_2$ . The design and fabrication of two active THz wavefront modulator devices has been completed. In their on-state, one device can focus the THz wave into four foci as shown in Fig.3.6(b), while the other can generate a THz ring-Airy beam as shown in Fig.3.6(c).

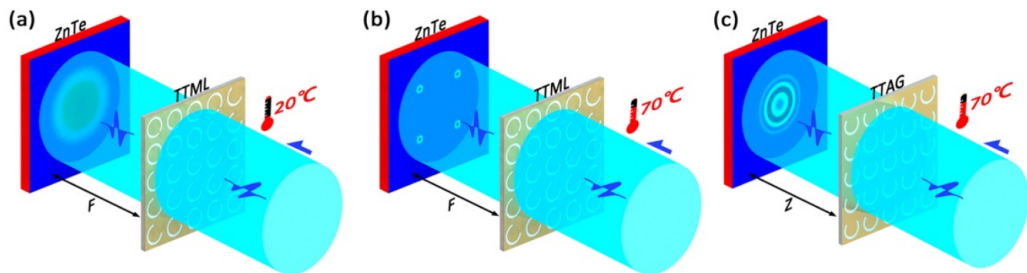


Figure 3.6: The configuration for studying operational properties of THz wavefront modulators as a function of temperature is shown in schematic [28].

Microstructuring arrays of C-shaped [29] slot antenna with varying opening angles into  $\text{VO}_2$  thin films (thickness roughly  $1\ \mu\text{m}$ ) produced on c-sapphire substrates (thickness  $330\ \text{m}$ ) with a thin  $\text{TiO}_2$  buffer layer manufactured both devices (thickness  $20\ \text{nm}$ ). When the  $\text{VO}_2$  is metallic, the C-shaped slot antennas effect THz radiation only at temperatures over  $T_C$ . The geometric parameters of each C-shaped slot antenna allow one to adjust the scattered cross-polarized THz field's amplitude and phase locally. An array of specifically constructed C-shaped slot antennas can thus be used to modulate the amplitude and phase of a THz plane wave's wavefront.

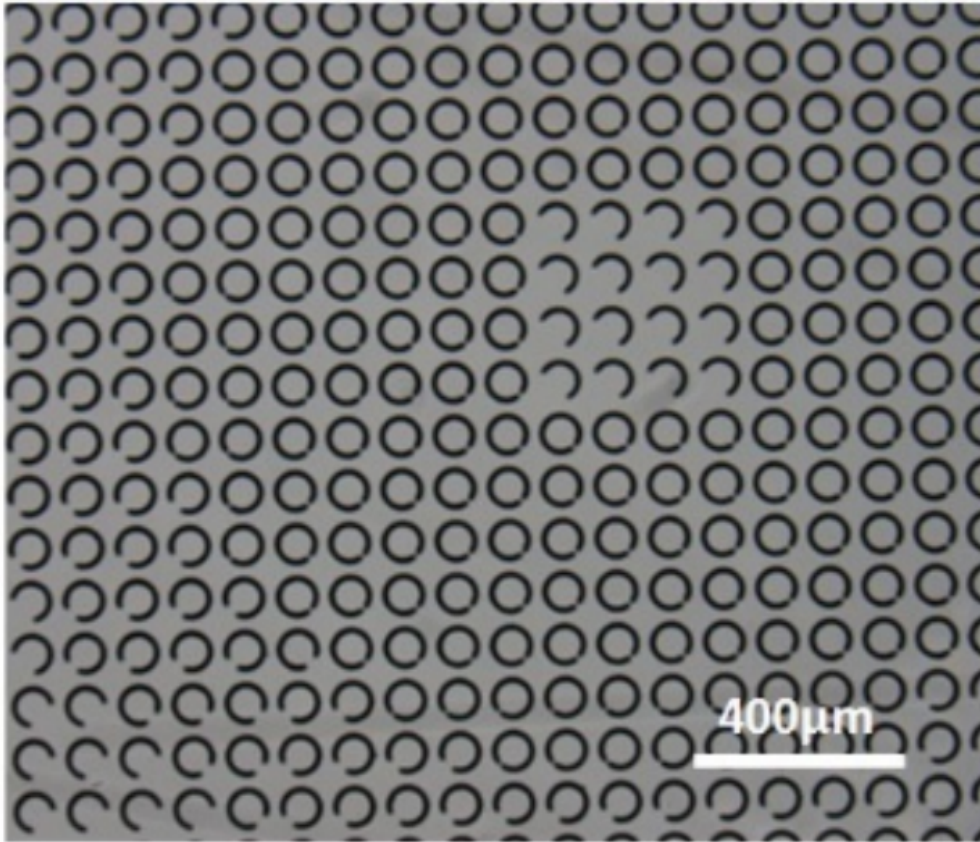


Figure 3.7: Photograph of a part of TML [28].

The metasurface, which is made up of eight various types of C-shaped slot antenna units with variable split opening angles ( $\theta = 10^\circ, 35^\circ, 100^\circ$ , and  $132^\circ$ ) and azimuth angles ( $\beta = \pm 45^\circ$ ), acts as a THz multi-focus lens. At the design operating frequency of 0.8 THz, each type of antenna unit produces a different constant phase change of the cross-polarized wave in the range of 0 to  $2\pi$ . In this approach, the eight individual antenna units allow for eight distinct phase shifts with an equal spacing of  $\pi/4$  in the range of 0 to  $2\pi$ . The TML's desired spatial phase distribution is calculated using the Yang-Gu amplitude-phase retrieval technique [30]. This spatial phase distribution has been digitized using multiples of  $\pi/4$ .

Figure 3.7 shows a micrograph of a portion of the TML's metasurface. It depicts antenna units that are microstructured into the  $VO_2$  thin film and are placed in a regular pattern with a  $100 \mu\text{m}$  pitch.

In a similar way, the tunable TAG was created. To digitalize the spatial dis-

tributions of phase and amplitude in the associated metasurface plane, 32 distinct types of antenna units were used. For phase shifts of  $\pi$  and  $2\pi$ , the different antenna types produce an amplitude quantization into 16 values spanning from 0 to the intensity maximum at the operating frequency of 0.8 THz. The 32 antenna unit's azimuth angles are chosen as follows:  $\beta = \pm 1^\circ, \pm 3^\circ, \pm 4^\circ, \pm 6^\circ, \pm 7^\circ, \pm 8^\circ, \pm 9^\circ, \pm 10^\circ, \pm 12^\circ, \pm 13^\circ, \pm 17^\circ, \pm 19^\circ, \pm 21^\circ, \pm 25^\circ, \pm 30^\circ, \pm 45^\circ$ . The positive sign and negative sign indicate the phases of the cross-polarized wave are  $\pi$  and  $2\pi$ , respectively.

The performance of the thermally controllable THz wavefront modulators was characterized using a THz imaging system. Figure 3.8 shows a diagram of the experimental setup. For generating and detecting THz waves, a laser beam with an average strength of 900 mW was split into two parts: a pump beam (880 mW) and a probe beam (20 mW). The TML and TAG device's, z-scan measurements were made by simply moving the sample along the z-axis.

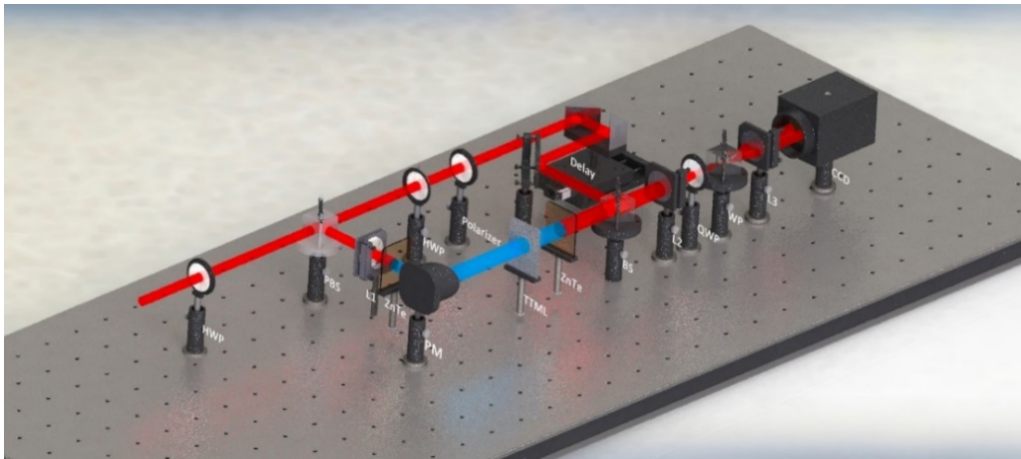


Figure 3.8: Imaging system based on THz. TTML: Temperature controlled THz multi-focus lens, HWP: half wavelength plate, PBS: polarization beam splitter, L: lens, PM: parabolic mirror, BS: beam splitter, QWP: quarter-wavelength plate, WP: Wollaston polarizer [28].

Figures 3.9(a) and 3.9(b) show the intensity distributions on the focal plane of the TML measured with THz radiation at 0.8 THz (design operating frequency) at temperatures of 20°C and 70°C, respectively. At 20°C, a uniform THz spot with a diameter of 4.0 mm may be seen in the focal plane. It relates to a parallel beam of THz radiation flowing through the TML with little modification. The  $VO_2$  is in its insulating phase at this temperature, and the antenna structures do not modulate the wavefront, i.e. the TML's lens action is turned off. When the  $VO_2$  is in its metallic phase, i.e., when the device is in its on-state, the image on

the focus plane changes. In the related image, four foci can be seen, suggesting that the  $VO_2$  microstructures do indeed operate as C-shaped slot antennas and alter the THz wavefront. In accordance with the TML's design, the distances between pairs of two neighboring focal points in the x and y directions are both 2 mm. The experimental results clearly reveal that the microstructuring of the thin film had no effect on the IMT of the  $VO_2$ , and that antenna structures microstructured into  $VO_2$  might definitely serve as actively switchable building blocks for THz devices based on metastructures or metasurfaces.

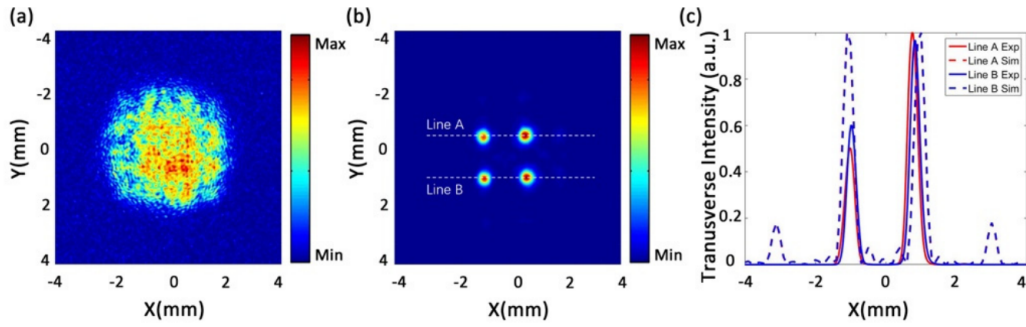


Figure 3.9: The TML's switching characteristics [28].

The lateral intensity distributions along the dashed lines in Fig. 3.9(b) are extracted and shown in Fig.3.9(c) to further investigate the properties of the TML in its on-state. The intensity distributions along lines A and B are represented by the red and blue curves, respectively. For easier comparison, the numerical simulation results are also given as dashed lines. The same phase distribution generated by the Yang-Gu technique is used in the simulation, and homogeneous light is assumed.

Similarly, the thermally switchable TAG's performance was evaluated in the off-state at  $20^\circ\text{C}$  and the on-state at  $70^\circ\text{C}$ . The results at  $20^\circ\text{C}$  confirm that when the material is insulating, the  $VO_2$  C-shaped slot antenna structures do not operate at temperatures below  $T_C$ . At these temperatures, the TAG's metasurface has no effect on the wavefront of THz radiation. The experimental results matched the simulation results well.

Temperature-driven  $VO_2$  IMT is reversible, and there is no aging effects. The IMT is accompanied by a structural phase shift from a monoclinic ( $T < T_C$ ) to a tetragonal ( $T > T_C$ ) lattice structure. The structural phase transition, on the other hand, is characterized by small microscopic changes in the link lengths between nearby atoms. Not only is this microscopic process reversible, but it also happens very quickly. On a time period of a few hundred femtoseconds, it occurs. As a result, instead of thermal switching, electrical or optical switching can be employed to increase switching speed.

The materials issue is generating  $VO_2$  thin films that are also homogeneous on the mesoscopic scale (e.g., have a crisp grain size distribution or suffer a homogeneous strain owing to the substrate), as such mesoscopic characteristics affect the transition temperature and hysteresis behavior. However, author have showed that the  $VO_2$  C-shaped slot antenna units can alter the amplitude and phase of dispersed THz light when the  $VO_2$  is in its metallic phase. At temperatures  $T > T_C$ ,  $VO_2$  antennas reveal not only metal properties, but also localized surface plasmon resonances. As a result, metasurface devices based on such  $VO_2$  micro-structures may modulate light fields in the same way that gold metasurface devices can. Furthermore, the  $VO_2$  based devices allow for thermal switching of this feature on ( $T > T_C$ ) and off ( $T < T_C$ ). Such metasurface devices have a high transmittance in the off-state and have little effect on the THz beam profile. As a result, thermochromic  $VO_2$  metasurface devices have a lot of potential for creating temperature-controlled light field devices in the future.

### **3.5 Graphene-Based Plasmonic Nano-Antenna Array**

Dynamic beamforming antenna arrays are necessary in a mobile network to dynamically steer the beam direction. Smart antenna arrays with programmable parts have been proved to work at up to 140 GHz [32], however existing antenna arrays at genuine THz frequencies do not support dynamic beamforming [33].

The difficulties in achieving real THz frequencies and utilizing the available bandwidth encourage the development of new, alternative technologies. One such intriguing alternative is the use of graphene-based plasmonic devices that operate in the THz region.

Graphene is a two-dimensional carbon substance with exceptional electrical conductivity, making it ideal for the transmission of extremely high-frequency electrical signals. Furthermore, graphene allows highly adjustable Surface Plasmon Polariton (SPP) waves to propagate directly at THz frequencies. SPP waves are highly restricted electromagnetic (EM) waves created at the conductor-dielectric interface, with wavelengths many orders of magnitude less than freespace EM waves of the same frequency. The intrinsic tunability of graphene and the highly confined wavelength of SPP waves enable the development of novel graphene-based plasmonic devices for signal generation and detection, modulation and demodulation, and radiation, all of which operate at true THz frequencies. Nonetheless, there is a limit to how much power a single gadget can output, and thus how far it can communicate.

The author suggest a new beamforming antenna array architecture for THz

communications in this article [31], which takes advantage of graphene's unique features. The proposed architecture comprises of an on-chip plasmonic THz signal generator, an on-chip plasmonic phase modulator and controller, and an on-chip plasmonic nano-antenna, and each element represents a complete THz front-end.

The capacity of graphene to vary its amplitude and phase dynamically is used to apply beamforming weights to each piece. The author present a new customized weight selection approach in light of the shown beamforming capabilities and, in particular, the dependency of amplitude and phase selection. The proposed architecture can be utilized to create highly dense antenna arrays that can provide comprehensive (i.e., simultaneous phase and amplitude) beamforming control and potentially outperform current array topologies.

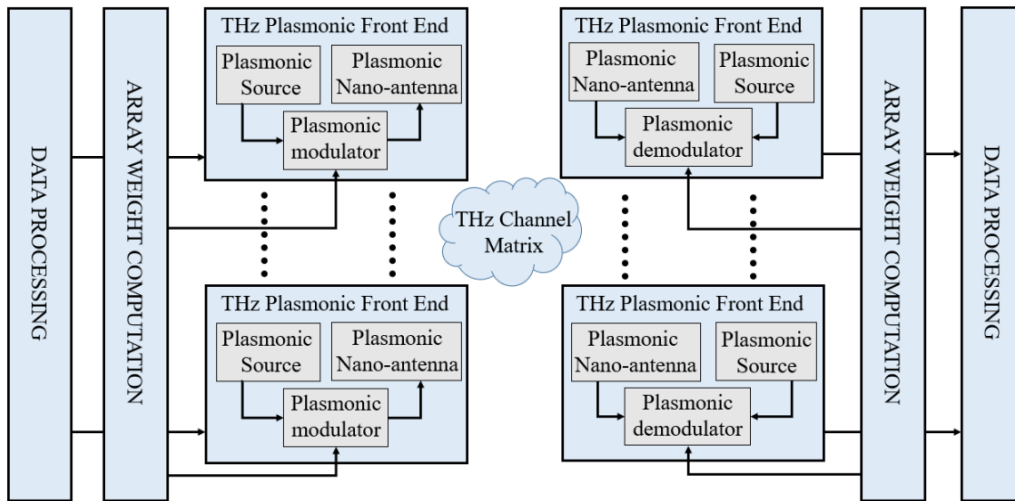


Figure 3.10: Graphene-based plasmonic nano-antenna array architecture [31].

This architecture shown in Fig.3.10 takes advantage of graphene plasmonic's unique features to considerably simplify array creation. Each component of the proposed architecture is a fully functional THz frontend. An on-chip plasmonic source, an on-chip plasmonic phase modulator, and an on-chip plasmonic nano-antenna make up the plasmonic front-end at the transmitter. The receiver's front-end is identical, except instead of a modulator, it has a demodulator.

The source is designed to create SPP waves at THz frequency efficiently. THz emission can be generated in a sub-micrometric resonant cavity with asymmetric boundary conditions and propagate on-chip to the plasmonic modulator. By adjusting the Fermi energy of the graphene layer, the modulator comprises of a graphene-based plasmonic waveguide. The SPP wave propagation speed is

changed, resulting in a phase shift at the output. SPP waves travel along the graphene layer rather than through it, resulting in substantially stronger SPP wave modulation.

In various ways, the suggested plasmonic array architecture varies from traditional systems. An independent source powers each plasmonic front-end. The addition of more front-ends to an array not only improves the radiation direction efficiency, but also increases the total output power. Without any additional gear, the plasmonic modulator shown in Fig.3.11 can directly modify the phase of SPP waves at THz frequency.

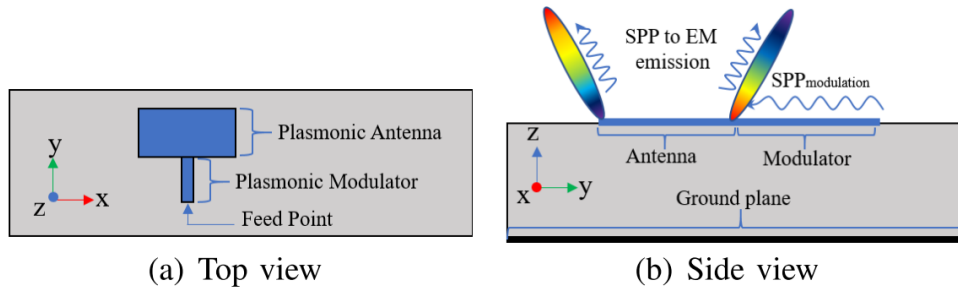


Figure 3.11: The THz front end's functioning principle and design. A plasmonic source (shown here with the feed point), a plasmonic modulator, and a plasmonic nano-antenna comprise the front end: a) top view; and b) side view [31].

As needed, the nano-antenna can be tuned to offer amplitude control. The mutual coupling between the radiating elements in this plasmonic array is determined by the SPP wavelength  $\lambda_{spp}$ , rather than the free-space wavelength,  $\lambda_0$ . As a result, these front-ends can be confined to a small space. The plasmonic array meets the requirements of a comprehensive dynamic beamforming system with no additional hardware, an independent power source per element, complete beamforming functionality, and an exceptionally tiny size.

Figure 3.12 depicts the planar plasmonic array. The resultant beam's orientation is indicated by the elevation angle  $\theta_0$  and azimuth angle  $\phi_0$ . To achieve the appropriate phase difference and amplitude attenuation, a codebook  $C$  consists of complex weights  $W_{i,j}$  corresponding to the  $i, j^{th}$  element must be defined.  $W_{i,j}$  is of the form  $Ae^{j\beta}$ , where  $A$  is the signal strength magnitude and  $\beta$  is the signal strength eigen value. The codebook is used in the plasmonic array by altering the modulator's Fermi energy,  $EF_{mod_{i,j}}$ , and the antenna's Fermi energy,  $EF_{ant_{i,j}}$ . As a result, the effective complex weight for a given element,  $W_{i,j}$ , is mapped to that element's modulator and antenna Fermi energy:

$$W_{i,j} \mapsto EF_{mod_{i,j}}, EF_{ant_{i,j}} \quad (3.3)$$

Consideration of phase and amplitude control separately is one technique to determine the codebook. After that, the effective complex valued weight  $W_{i,j}$  is created as follows:

$$\Im\{W_{i,j}\} \mapsto f(EF_{mod_{i,j}}), \Re\{W_{i,j}\} \mapsto f(EF_{ant_{i,j}}) \quad (3.4)$$

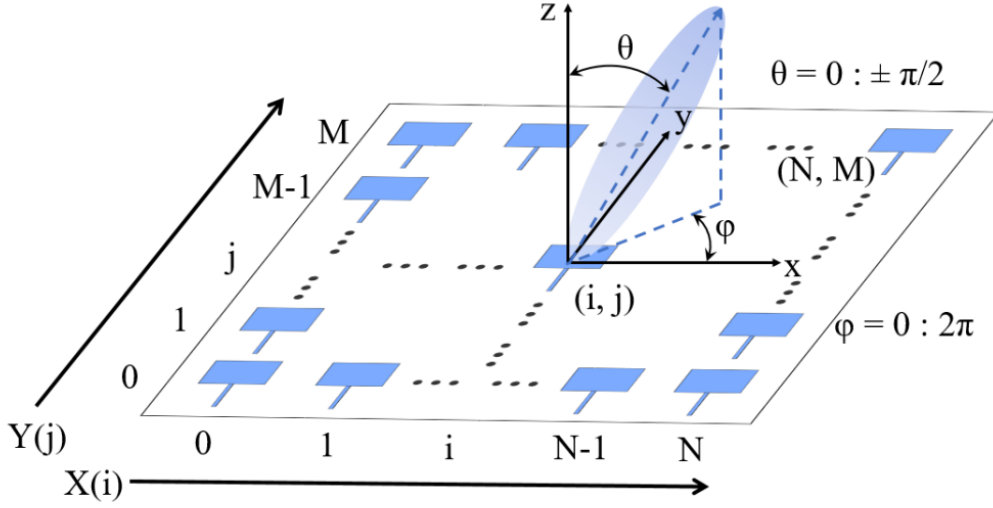


Figure 3.12: The plasmonic array's spatial geometry. The azimuth angle  $\phi_0$  specifies the angle of the beam with the x-axis, while the elevation angle  $\theta_0$  describes the divergence from the broadside direction [31].

While independent phase and amplitude control has its drawbacks, it is still worth considering the inclusion of the joint relationship in determining effective weights is a problem that adds to the complexity of the beamforming algorithm. More specifically, the weight computation cannot be split into two functions, but must be viewed as a single function with two control variables:

$$W_{i,j} \mapsto f(EF_{mod_{i,j}}, EF_{ant_{i,j}}) \quad (3.5)$$

The values of the modulator's Fermi energy and the antenna's Fermi energy corresponding to the effective weights needed for a given codebook can then be

retrieved using an algorithm [31], as required by array theory. The exact combination of  $EF_{mod}$  and  $EF_{ant}$  that produces the appropriate effective weight is only searched for once, and the values are then saved for future use.

The effective weights for each combination are determined analytically and shown in Fig.3.13. Every point in Fig.3.13 represents an effective weight in the complex plane (the signal strength is represented by the radius  $r$ , and the phase is represented by the angle). Using the data in Fig.3.13, all conceivable codebooks,  $C$ , that can be achieved when phase and amplitude control are considered together can have effective weights  $W_{Jointcodebook}$ , which are given by

$$W_{jointcodebook} \in [0.18e^{j0}, 1e^{j2\pi}]. \quad (3.6)$$

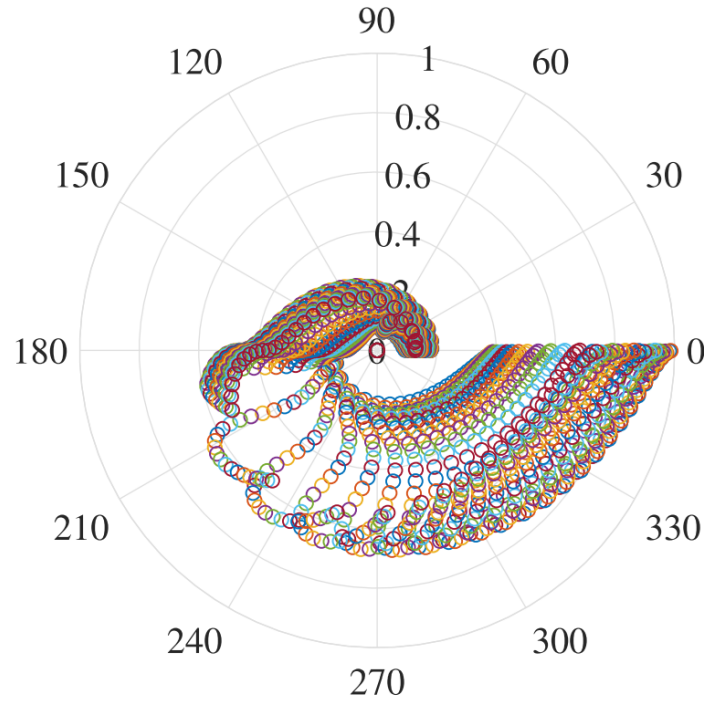


Figure 3.13: Polar representation of all effective weights that can be used in the joint consideration of codebook design  $W_{Jointcodebook}$  [31].

The application of codebook C3, which is developed from the algorithm, provides for better side-lobe strength minimization while preserving directional accuracy.

The Effective Isotropic Radiated Power (EIRP) of a linear array at various sizes is shown in Fig.3.15. The EIRP of a single front-end is also displayed, with the signal source having the cumulative power of the total number of array

members. The EIRP is calculated numerically up to a  $6 \times 1$  array size, after which a polynomial extrapolation is used to calculate the estimated EIRP of a bigger array. For each front-end that is being considered, the same technique is used. When the total input power is the same, the EIRP of the array outperforms the front-end, as expected.

The EIRP and footprint size for a  $6 \times 1$  array constructed according to the principles described in this article [31] are  $4.5 \text{ mW}$  and  $0.056 \text{ mm}^2$ , respectively. A  $6 \times 1$  plasmonic array's transmitted power density is thus  $80.16 \text{ mW/mm}^2$ . A  $32 \times 1$  array is expected to have an EIRP more than  $300 \text{ mW}$  using a polynomial approximation. The array's footprint would be  $0.3 \text{ mm}^2$ , with a radiation efficiency of  $1000 \text{ mW/mm}^2$ .

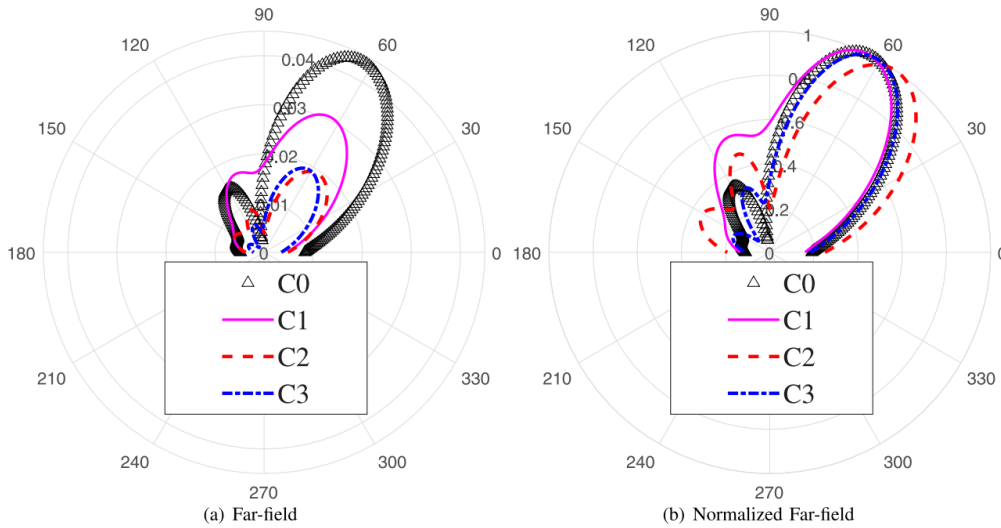


Figure 3.14: (a) Far-field radiation patterns created by putting the four separate codebooks to work, with the goal of steering the beam towards  $(\theta_0, \phi_0) = (30^\circ, 0^\circ)$ : C0 - Ideal weight, C1 - Phase control, C2 - Phase and amplitude control examined independently, C3 - Jointly considered phase and amplitude control b) Far-field radiation patterns derived with normalized far-field radiation patterns [31].

The use of electrostatic bias places a limit on the maximum feasible Fermi energy in order to perform accurate control of the graphene-based modulator and antenna as required to create the codebook. As indicated in [34], the constraint occurs when the electric field required reaches values that can cause dielectric breakdown of the substrate under consideration. In graphene, however, the maximum value of Fermi energy can be raised for the same electric bias by increasing Fermi velocity.

Furthermore, the effect of power attenuation and the propagation of plasmons

along the graphene layer necessitate a longer relaxation period than the most popular production methods can provide. When the quality of graphene production is compromised, the relaxation time is lowered, and the power attenuation is increased. Worse, the plasmons may fade out completely before crossing the entire length of the front-end, leaving the front-end in a ‘off’ condition.

Because the array design is based on the plasmonic wavelength, the array that can be created using this architecture is small, has a high EIRP, and can be used for a variety of beamforming applications. Fabrication and experimental testing of the array’s performance will be the focus of future efforts.

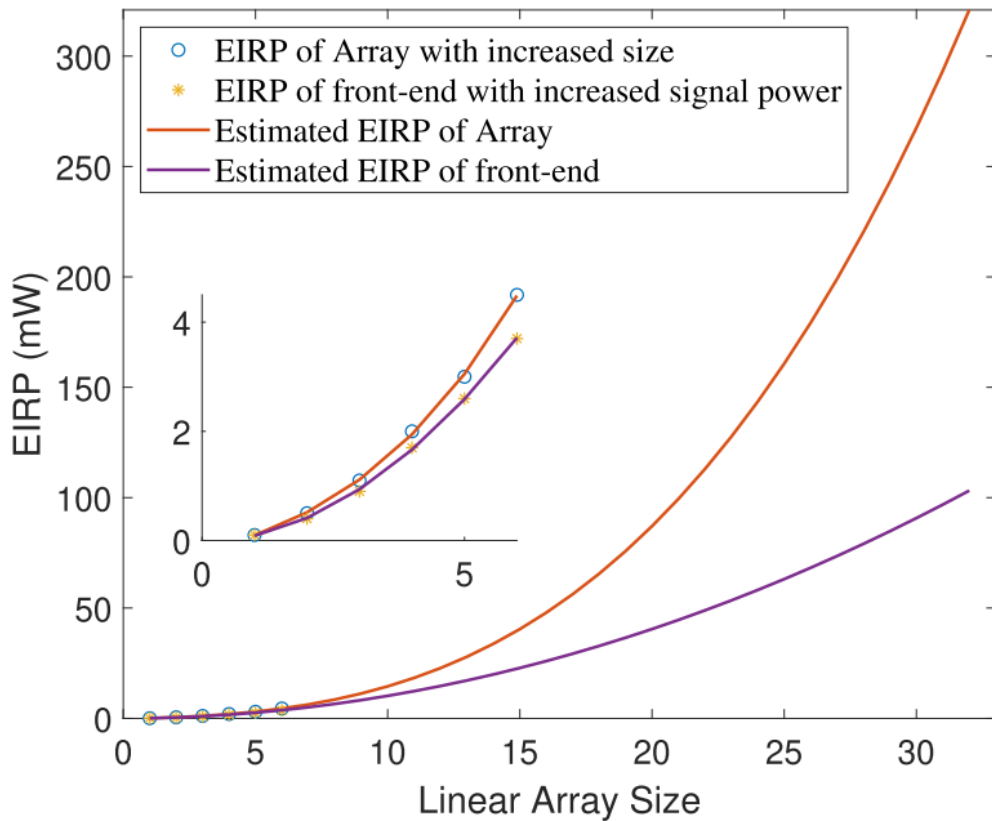


Figure 3.15: The EIRP as a function of element count [31].

# Chapter 4

## Conclusion

The technology of metasurfaces has been exposed in this thesis, with a focus on their structure and the models that are used to investigate them. The first chapter introduces the metasurface and its several generations, with a focus on Reconfigurable Intelligent Surfaces and their solutions. The second chapter demonstrates metasurface programming methods developed in recent years at the academic level, with a focus on space-time and time-varying metasurfaces for controlling and beamforming.

The third chapter depicts time-varying metasurfaces in the terahertz region in particular those that may be controlled electrically, thermally, and optically has received special attention.

According to my research, Graphene based Plasmonic nano antenna is the most promising technology especially in the terahertz band, since it has successfully demonstrated dynamic beamforming with accuracy. The power density of the array improves non-linearly with its size as each element gains an independent signal source and the ability to define narrow directional beams. Because the array design is dependent on the plasmonic wavelength, the array that can be created using this architecture is small, has a high EIRP, and may be used for a variety of beamforming applications.

Future study are expected to focus on developing a way to assess and fix a front-deviation from broadside emission while managing phase and amplitude, as even minor deviations have been shown to have a significant influence on beamforming ability. Fabrication and experimental testing are necessary in order to confirm expected results and material specifications. Other options for improving device performance can be explored once the developed models and algorithms have been experimentally validated. Another promising direction of research is represented by the possibility to perform more complex operations directly at EM level thanks to next generation metasurfaces with the purpose to shift part of the processing of the signal from the digital domain to the EM domain. The main

advantages of this perspective is expected to be in terms of reduced latency, complexity, power consumption and cost.

# List of Figures

1.1	Visual illustration of the Poincaré Sphere for representing polarisation states of light [2]. . . . .	2
1.2	The evolution of the metasurface notion across time. Homogeneous periodic structures characterize the first generation of metasurfaces. In-homogeneous metasurfaces with varied qualities in space make up the second generation of metasurfaces. Metasurfaces of the third generation are either homogeneous or in-homogeneous structures with properties that change over time [7].	4
1.3	A vision of a structured intelligent environment made up of metasurfaces whose attributes may be adjusted in real-time [7]. . . . .	5
1.4	Radio environments and smart radio environments have communication-theoretic models (with and without joint encoding) [8]. . . . .	7
1.5	IRS applications that are commonly used in wireless networks [11]. . . . .	9
1.6	IRS Architecture [11]. . . . .	10
1.7	The RFocus prototype from MIT (photo: Jason Dorfman, CSAIL) [8]. . . . .	11
1.8	The prototype of NTT DOCOMO (photo: NTT DOCOMO) [8]. .	12
1.9	BS transmit power vs Horizontal distance between User and BS [11]. . . . .	13
1.10	Multiple communication modes in LoS conditions, corresponding to parallel channels at the EM level, are used by a LIS to communicate with a mobile terminal equipped with a small intelligent surface [9]. . . . .	14
2.1	The coding metasurface and the 1-bit digital metasurface. (a) 1-bit digital metasurface: ‘0’ and ‘1’. (b) A square metallic patch unit structure for realizing the ‘0’ and ‘1’ elements. (c, d) Two 1-bit periodic coding metasurfaces for controlling beam scattering by designing ‘0’ and ‘1’ element coding sequences: (c) 010101.../010101... and (d) 010101.../ 101010... codes [3]. . . . .	16

2.2	Top view of the one-of-a-kind metamaterial particle used to create a digital metasurface, with specific geometrical characteristics [3].	18
2.3	The biased diode's effective circuit models in the "on" and "off" states. (a) The 'on' condition. (b) The 'off' condition [3]. . . . .	18
2.4	The metamaterial particle for realizing the digital metasurface and the corresponding phase responses. (a) The structure of the metamaterial particle, which behaves as '0' and '1' elements when the biased diode is 'OFF' and 'ON', respectively. (b) The corresponding phase responses of the metamaterial particle as the biased diode is 'OFF' and 'ON' over a range of frequencies [3]. . .	19
2.5	FPGA-controlled fabrication of a 1D digital metasurface. (a) The 1D digital metasurface from above. (b) FPGA (Field Programmable Gate Array). (c) The 1D digital metasurface from the bottom. (d) A zoomed image of the one-dimensional digital metasurface [3]. .	20
2.6	(a-d) Numerical simulation results of scattering patterns at 8.3 GHz for the 1D digital metasurface under different coding sequences: (a) 000000, (b) 111111, (c) 010101 and (d) 001011. (e-f) Experimental results of scattering patterns at 8.6 GHz for the 1D digital metasurface under different coding sequences: (e) 000000, (f) 111111, (g) 010101 and (h) 001011. (i) A flow diagram for realizing a programmable metasurface controlled by the FPGA hardware [3]. . . . .	21
2.7	Two applications of reconfigurable metasurfaces in multi-user mMIMO wireless communications: downlink (gray arrows) and uplink (blue arrows): a) as near-passive reflective surfaces; b) as active transceiver antenna arrays [13]. . . . .	22
2.8	An N-element DMA made up of M microstrips, each of which is implemented as a one-dimensional waveguide. The upper right and bottom right halves of the diagram show how they work during transmission and reception, respectively, as well as their analogous signal route models [13]. . . . .	24
2.9	(a)Uplink sum-rate performance in bps/Hz versus SNR in dB for a 160-antenna mMIMO BS with 16 RF chains serving 64 users simultaneously within a 400m radius(b)Uplink sum-rate performance in bps/Hz versus SNR in dB for a 640-antenna mMIMO BS with 64 RF chains serving 64 users simultaneously within a cell with a 400m radius [13]. . . . .	25
2.10	DMA focusing for multi-user communications in close proximity [13]. . . . .	27
2.11	The achievable rates of each of the users, i.e., $R_1, R_2$ [13]. . . . .	28

2.12	(a) A typically impinging electromagnetic field with frequency $\omega_i = c_0 k_i$ and propagating in the negative z-direction illuminates a metasurface with a time-varying surface admittance $Y_s(t)$ . A field reflected back with a different frequency $r = c_0 k_r$ . (b) A model of the system's equivalent transmission line is shown in Fig.2.12 (a) [16]. . . . .	30
2.13	For both polarizations of the impinging electromagnetic field, the amplitude and phase of the reflection coefficient as a function of polarization voltage $V_{\text{bias}}$ . $F_i = 1.5$ GHz is the lighting frequency [16]. . . . .	31
2.14	Up and down-conversion are achieved by driving voltage modulating signals at a frequency of $f_m = 500$ kHz (blue and red dashed lines, respectively) [16]. . . . .	32
2.15	(a) Serrodyne frequency translator based on a transparent metasurface. (b) A time-modulated analogous impedance-matched medium [17]. . . . .	34
2.16	(a) Harmonic distribution as a function of propagation distance in a time-modulated medium. (b) Field amplitudes as a function of propagation distance for the first five harmonics [17]. . . . .	35
2.17	Time course of the refractive index $n(t)$ . . . . .	36
2.18	(a) A bias waveform is a waveform that is used to measure anything. (b) Transmission spectrum of a 10 GHz CW signal incident on the transmissive frequency translator as measured [17]. . . . .	37
2.19	Illustration of a digital metasurface with space-time coding. By applying control voltages to PIN diodes, the metasurface element's reflection coefficient can be dynamically modified with discrete phase or amplitude states. The reflection phase of each coding element in the shown example is periodically swapped according to the digital "0/1" space-time-coding matrix, which can result in similar multi-bit space-coding, such as "0", "1", "2" and "3" (equivalent 2-bit case). This coding approach allows for exact control of electromagnetic waves in both the spatial and frequency domains [18]. . . . .	39
2.20	Harmonic beam steering. a, b The related 2D coding matrix and the 3D space-time-coding matrix. The red and green dots, respectively, represent the "1" and "0" digits. c, d AM and PM methods have equivalent amplitude and phase distributions, respectively. The phase gradients that emerge at the various harmonic frequencies are indicated by the white arrows. e, f Corresponding 1D scattering pattern cuts (at $\phi = 90^\circ$ ) at different harmonic frequencies pertaining to AM and PM schemes, respectively [18]. . . . .	40

2.21	BPSO-optimized harmonic beam steering. a Optimized 2D space-time-coding matrix. b, c, d Corresponding 1D scattering-pattern cuts at $\varphi = 90^\circ$ , 2D, and 3D scattering patterns, respectively, at different harmonic frequencies [18]. . . . .	42
2.22	Prototype design, modeling, and characterization. a Schematic of the realized space-time-coding metasurface prototype. b Geometry of the coding element with the biasing line. c Equivalent circuit models of the PIN diode biased at the ‘ON’ and ‘OFF’ states. d Measurement setup in an anechoic chamber. e Photo of the fabricated prototype. f, g Numerically computed reflection phase and amplitude of the coding element, respectively, for both diode states as a function of frequency. The grey-shaded areas indicate a neighborhood of the operational frequency (10 GHz) [18]. . . . .	43
2.23	A metaprism empowers the analyzed NLOS scenario [21]. . . . .	44
2.24	Metasurface composed of elementary cells (top). Equivalent model of the cell (bottom) [21]. . . . .	45
2.25	A digitally programmable nonreciprocal metasurface prism in concept [19]. . . . .	47
2.26	The nonreciprocal metasurface prism’s programmable composition. The operation of the metasurface is guided by a four-step architecture, with each level demonstrating the necessary transmission phase and magnitude for controllable and programmable nonreciprocal prism functionality [19]. . . . .	47
2.27	Spread-spectrum time-modulated metasurface camouflaging is proposed [20]. . . . .	49
2.28	Camouflaging selectivity [20]. . . . .	50
2.29	Camouflaging selectivity [22]. . . . .	51
2.30	A QPSK system’s constellation diagram exhibiting phase shifting [22]. . . . .	52
2.31	BER (%) of GSM signal transmitted through the reconfigurable FSS using (a) measured and (b) simulated data [22]. . . . .	53
3.1	The graphene microribbon array is depicted schematically on top of a $10 \mu\text{m}$ thick dielectric spacer and a metallic mirror in this diagram. The frequency shift of the wave upon reflection is represented by arrows of various colors [25]. . . . .	55
3.2	(a) Calculated graphene microribbon array metasurface reflection spectra for three distinct graphene Fermi energies. (b) A single graphene microribbon unit cell’s simulated electric field distribution ( $E_z$ ) [25]. . . . .	56

3.3	(a) A temporal modulation strategy for modifying graphene Fermi levels has been proposed. (b) For varied operation wavelengths of a time-varying metasurface, calculated frequency change of reflected terahertz waves [25]. . . . .	57
3.4	(a) The experiment is depicted schematically. (b) Metasurface amplitude transmission as a function of time delay (y axis) and frequency (x axis). (c) Amplitude transmission with different time delays: -4 ps (black), 2 ps (red), and 15 ps (blue). (d) Amplitude transmission as a function of time delay at 0.92 THz. The theoretical computation is indicated by the dot line [27]. . . . .	59
3.5	(a) Illustration of a schematic and (b) a microscopic photograph of a metasurface. The polarization of the input THz wave is indicated by the arrows in (a). (c) Schematic illustration of metasurface temporal conductivity change with and without external voltage. (d) Transmission spectra measured through metasurface without external voltage as a function of time delay, $t_d$ , and (e) transmission spectra obtained with 32 V external voltage (f) Selected transmission spectra with (red) and without voltage at $t_d= 2$ ps (blue). The transmission spectrum through the metasurface without optical pumping is shown in black. (g) Transmission spectra with and without voltage at $t_d = 10$ ps. (h) Numerical simulation of transmission spectra via a metasurface with a conducting layer for the full exposed region (blue), a conducting layer except for the gap (red), and no conducting layer (black) [34]. . . . .	61
3.6	The configuration for studying operational properties of THz wavefront modulators as a function of temperature is shown in schematic [28]. . . . .	63
3.7	Photograph of a part of TML [28]. . . . .	64
3.8	Imaging system based on THz. TTML: Temperature controlled THz multi-focus lens, HWP: half wavelength plate, PBS: polarization beam splitter, L: lens, PM: parabolic mirror, BS: beam splitter, QWP: quarter-wavelength plate, WP: Wollaston polarizer [28]. . . . .	65
3.9	The TML's switching characteristics [28]. . . . .	66
3.10	Graphene-based plasmonic nano-antenna array architecture [31].	68
3.11	The THz front end's functioning principle and design. A plasmonic source (shown here with the feed point), a plasmonic modulator, and a plasmonic nano-antenna comprise the front end: a) top view; and b) side view [31]. . . . .	69

3.12	The plasmonic array's spatial geometry. The azimuth angle $\phi_0$ specifies the angle of the beam with the x-axis, while the elevation angle $\theta_0$ describes the divergence from the broadside direction [31]. . . . .	70
3.13	Polar representation of all effective weights that can be used in the joint consideration of codebook design $W_{Joint\_codebook}$ [31]. . . . .	71
3.14	(a) Far-field radiation patterns created by putting the four separate codebooks to work, with the goal of steering the beam towards $(\theta_0, \phi_0) = (30^\circ, 0^\circ)$ : C0 - Ideal weight, C1 - Phase control, C2 - Phase and amplitude control examined independently, C3 - Jointly considered phase and amplitude control b) Far-field radiation patterns derived with normalized far-field radiation patterns [31]. . . . .	72
3.15	The EIRP as a function of element count [31]. . . . .	73

# Bibliography

- [1] Alsharif, Mohammed H., et al. "Toward 6G communication networks: Terahertz frequency challenges and open research issues." *Computers, Materials and Continua* 66.3 (2021): 2831-2842.
- [2] Kenney, Mitchell Guy. "The development of metasurfaces for manipulating electromagnetic waves." Diss. University of Birmingham, 2016.
- [3] Cui, Tie Jun, et al. "Coding metamaterials, digital metamaterials and programmable metamaterials." *Light: Science and Applications* 3.10 (2014): e218-e218.
- [4] Yu, Nanfang et al. "Light Propagation with Phase Discontinuities: Generalized Laws of Reflection and Refraction." *Science* 334 (2011): 333 - 337.
- [5] Chen, X., Huang, L., Mühlenbernd, H., Li, G., Bai, B., Tan, Q., Jin, G., Qiu, C., Zhang, S., and Zentgraf, T. (2012). Dual-polarity plasmonic metalens for visible light. *Nature Communications*, 3, [1198]. <https://doi.org/10.1038/ncomms2207>
- [6] Khorasaninejad, Mohammadreza, and Kenneth B Crozier. "Silicon nanofin grating as a miniature chirality-distinguishing beam-splitter." *Nature communications* vol. 5 5386. 12 Nov. 2014, doi:10.1038/ncomms6386
- [7] M. Barbuto et al., "Metasurfaces 3.0: a Key Enabling Technology for the Development of beyond-5G Communication Systems," 2020 Fourteenth International Congress on Artificial Materials for Novel Wave Phenomena (Metamaterials), 2020, pp. 502-504, doi: 10.1109/Metamaterials49557.2020.9285131.
- [8] M. Di Renzo et al., "Smart Radio Environments Empowered by Reconfigurable Intelligent Surfaces: How It Works, State of Research, and The Road Ahead," in *IEEE Journal on Selected Areas in Communications*, vol. 38, no. 11, pp. 2450-2525, Nov. 2020, doi: 10.1109/JSAC.2020.3007211.

- [9] D. Dardari and N. Decarli, "Holographic Communication Using Intelligent Surfaces," in *IEEE Communications Magazine*, vol. 59, no. 6, pp. 35-41, June 2021, doi: 10.1109/MCOM.001.2001156.
- [10] D. Dardari, "Communicating With Large Intelligent Surfaces: Fundamental Limits and Models," in *IEEE Journal on Selected Areas in Communications*, vol. 38, no. 11, pp. 2526-2537, Nov. 2020, doi: 10.1109/JSAC.2020.3007036.
- [11] Wu, Qingqing, and Rui Zhang. "Towards smart and reconfigurable environment: Intelligent reflecting surface aided wireless network." *IEEE Communications Magazine* 58.1 (2019): 106-112.
- [12] A. Abrardo, D. Dardari and M. Di Renzo, "Intelligent Reflecting Surfaces: Sum-Rate Optimization Based on Statistical Position Information," in *IEEE Transactions on Communications*, vol. 69, no. 10, pp. 7121-7136, Oct. 2021, doi: 10.1109/TCOMM.2021.3096549.
- [13] N. Shlezinger, G. C. Alexandropoulos, M. F. Imani, Y. C. Eldar and D. R. Smith, "Dynamic Metasurface Antennas for 6G Extreme Massive MIMO Communications," in *IEEE Wireless Communications*, vol. 28, no. 2, pp. 106-113, April 2021, doi: 10.1109/MWC.001.2000267.
- [14] Zhang, Haiyang, et al. "Beam Focusing for Multi-User MIMO Communications with Dynamic Metasurface Antennas." *ICASSP 2021-2021 IEEE International Conference on Acoustics, Speech and Signal Processing (ICASSP)*. IEEE, 2021.
- [15] S. Henthorn, K. L. Ford and T. O'Farrell, "Bit-Error-Rate Performance of Quadrature Modulation Transmission Using Reconfigurable Frequency Selective Surfaces," in *IEEE Antennas and Wireless Propagation Letters*, vol. 16, pp. 2038-2041, 2017, doi: 10.1109/LAWP.2017.2695008.
- [16] Ramaccia, Davide, et al. "Phase-induced frequency conversion and doppler effect with time-modulated metasurfaces." *IEEE Transactions on Antennas and Propagation* 68.3 (2019): 1607-1617.
- [17] Wu, Zhanni, and Anthony Grbic. "Serrodyne frequency translation using time-modulated metasurfaces." *IEEE Transactions on Antennas and Propagation* 68.3 (2019): 1599-1606.
- [18] Zhang, Lei, et al. "Space-time-coding digital metasurfaces." *Nature communications* 9.1 (2018): 1-11.

- [19] Taravati, Sajjad, and George V. Eleftheriades. "Programmable nonreciprocal meta-prism." *Scientific Reports* 11.1 (2021): 1-12.
- [20] Wang, Xiaoyi, and Christophe Caloz. "Spread-spectrum selective camouflaging based on time-modulated metasurface." *IEEE Transactions on Antennas and Propagation* 69.1 (2020): 286-295.
- [21] Dardari, Davide, and Devis Massari. "Using metaprisms for performance improvement in wireless communications." *IEEE Transactions on Wireless Communications* 20.5 (2021): 3295-3307.
- [22] Roberts, Jiayin, Kenneth Lee Ford, and Jonathan M. Rignall. "Secure electromagnetic buildings using slow phase-switching frequency-selective surfaces." *IEEE Transactions on Antennas and Propagation* 64.1 (2015): 251-261.
- [23] Tennant, A. and Chambers, B. Time-switched array analysis of phase-switched screens. *IEEE Trans. Antennas Propag.* 57, 808-812 (2009).
- [24] Kummer, W., Villeneuve, A., Fong, T. and Terrio, F. Ultra-low sidelobes from time-modulated arrays. *IEEE Trans. Antennas Propag.* 11, 633-639 (1963).
- [25] Liu, Zizhuo, Zhongyang Li, and Koray Aydin. "Time-varying metasurfaces based on graphene microribbon arrays." *Acs Photonics* 3.11 (2016): 2035-2039.
- [26] F. R. Morgenthaler, "Velocity Modulation of Electromagnetic Waves," in *IRE Transactions on Microwave Theory and Techniques*, vol. 6, no. 2, pp. 167-172, April 1958, doi: 10.1109/TMTT.1958.1124533.
- [27] K. Lee, J. Son, B. Kang, J. Park, F. Rotermund and B. Min, "Linear frequency conversion via sudden merging of resonances in time-variant terahertz metasurfaces," 2017 42nd International Conference on Infrared, Millimeter, and Terahertz Waves (IRMMW-THz), 2017, pp. 1-2, doi: 10.1109/IRMMW-THz.2017.8067111.
- [28] Teng Wang, Jinwen He, Jinying Guo, Xinke Wang, Shengfei Feng, Florian Kuhl, Martin Becker, Angelika Polity, Peter J. Klar, and Yan Zhang, "Thermally switchable terahertz wavefront metasurface modulators based on the insulator-to-metal transition of vanadium dioxide," *Opt. Express* 27, 20347-20357 (2019)

- [29] X. Zhang, Z. Tian, W. Yue, J. Gu, S. Zhang, J. Han, and W. Zhang, "Broadband terahertz wave deflection based on C-shape complex metamaterials with phase discontinuities," *Adv. Mater.* 25(33), 4567-4572 (2013).
- [30] B. Gu, G. Yang, and B. Dong, "General theory for performing an optical transform," *Appl. Opt.* 25(18), 3197-3206 (1986).
- [31] A. Singh, M. Andrello, N. Thawdar and J. M. Jornet, "Design and Operation of a GrapheneBased Plasmonic Nano-Antenna Array for Communication in the Terahertz Band," in *IEEE Journal on Selected Areas in Communications*, vol. 38, no. 9, pp. 2104-2117, Sept. 2020, doi: 10.1109/JSAC.2020.3000881.
- [32] A. Simsek, S.-K. Kim, and M. J. W. Rodwell, "A 140 GHz MIMO transceiver in 45 nm SOI CMOS," in *Proc. IEEE BiCMOS Compound Semiconductor Integr. Circuits Technol. Symp. (BCICTS)*, Oct. 2018, pp. 231-234.
- [33] K. M. Luk et al., "A microfabricated low-profile wideband antenna array for terahertz communications," *Sci. Rep.*, vol. 7, no. 1, Dec. 2017, Art. no. 1268.
- [34] Fuscaldo, Walter et al. "Graphene-Based Fabry-Perot Cavity Leaky-Wave Antennas: Towards an Experimental Validation." 2018 48th European Microwave Conference (EuMC) (2018): 276-279.

